Electron Energy Loss Spectroscopy for Probing Nanophotonic Excitations at High Energy and Momentum

by

Prashant Shekhar

A thesis submitted in partial fulfillment of the requirements for the degree of

Doctor of Philosophy

in

Photonics and Plasmas

Department of Electrical and Computer Engineering

University of Alberta

Abstract

Strong nanoscale light-matter interaction is often accompanied by ultra-confined photonic modes and large momentum polaritons existing far beyond the light cone. A direct probe of such phenomena is difficult due to the momentum mismatch of these modes with free space light however, fast electron probes can reveal the fundamental classical, quantum and spatially dispersive behavior of these excitations. In chapter 2, we use momentum-resolved electron energy loss spectroscopy (k-EELS) in a transmission electron microscope to explore the optical response of plasmonic thin films including momentum transfer up to wavevectors (k) significantly exceeding the light line wave vector. We show close agreement between experimental k-EELS maps, theoretical simulations of fast electrons passing through thin films and the momentum-resolved photonic density of states (k-PDOS) dispersion. Although a direct link between k-EELS and the k-PDOS exists for an infinite medium, here we show fundamental differences between k-EELS measurements and the k-PDOS that must be taken into consideration for realistic finite structures with no translational invariance along the direction of electron motion.

Chapter 3 builds on the foundations of chapter 2 to probe silicon thin films and probe its properties in a completely new regime of the spectrum with k-EELS. Silicon is widely used as the material of choice for semiconductor and insulator applications in nano-electronics, MEMS, solar cells and on-chip photonics. In stark contrast, in this thesis, we explore silicon's metallic properties and show that it can support propagating surface plasmons, collective charge oscillations, in the extreme ultra-violet (EUV) energy regime not possible with other plasmonic materials such as aluminum, silver, or gold. This is fundamentally different from conventional ap-

proaches where doping semiconductors is considered necessary to observe plasmonic behavior. We experimentally map the photonic band structure of extreme ultraviolet (EUV) surface and bulk plasmons in silicon using k-EELS. The experimental observations are validated by macroscopic electrodynamic electron energy loss theory simulations as well as quantum density functional theory calculations. As an example of exploiting these EUV plasmons for applications, we propose a tunable and broadband thresholdless Cherenkov radiation source in the EUV using silicon plasmonic metamaterials.

In chapter 4 we expand the use of k-EELS to probe more exotic nanophotonic structures in the form of Bi_2Te_3, a naturally occurring hyperbolic material. Hyperbolic materials, uniaxial structures with a metallic response along one direction and dielectric response along the orthogonal direction, support unique electromagnetic modes with a wide variety of deep subwavelength applications in waveguiding, imaging, sensing, quantum and thermal engineering beyond conventional devices. They derive their name from their unique hyperbolic isofrequency typology that can support photonic excitations at large wave-vectors (high-k modes) that would normally decay in conventional media. With k-EELS we perform the first measurements of the high-k modes in Bi_2Te_3 and confirm its natural hyperbolic character from the visible to the UV. k-EELS proves to be the ideal tool for probing hyperbolic media as the relativistic electrons have a high momentum that are able to couple to Bi_2Te_3's large momentum (high-k) states that are difficult to probe optically. Additionally, we expand on the theoretical ideas proposed in chapter 3 to perform the first measurement of hyperbolic Cherenkov radiation in a natural hyperbolic material and discuss its unique thresholdless Cherenkov radiation properties.

The work in this thesis paves the way for using k-EELS as the preeminent tool for mapping the k-PDOS of exotic phenomena with large momenta (high-k) such as hyperbolic polaritons, Cherenkov radiation and spatially-dispersive plasmons. In addition k-EELS can also probe excitations at high energy that are difficult to probe optically. As a result, this work has laid the foundations for a focused application: a coherent, compact, tunable, and broadband EUV source.

Preface

Some of the research presented in this thesis consists of work published in peer reviewed journals. Specifically chapter 2 is a direct reproduction of:

- P. Shekhar, M. Malac, V. Gaind, N. Dalili, A. Meldrum, and Z. Jacob, "Momentum-Resolved Electron Energy Loss Spectroscopy for Mapping the Photonic Density of States," ACS Photonics 4, 10091014 (2017).

In chapter 2 the fabrication of the silver samples via electron beam deposition, the measurement of the samples via k-EELS in the TEM, the coding/calculations of the electron energy loss scattering probability in MATLAB and the writing of the full manuscript were performed by myself. Several discussions and guidance regarding the formulation of the energy loss scattering probability were had with Vaibhav Gaind. In particular, the analytic expressions of the behaviour of the energy loss scattering probability in the limit of large momentum can be attributed to him. Zubin Jacob and Marek Malac were the supervising authors and were involved with the concept formation and finalizing the manuscript for publication.

Chapter 3 is currently under review for publication in the journal *Optica*. Chapter 3 is a reproduction of the submitted manuscript and consists of the following author list:

- Prashant Shekhar, Sarang Pendharker, Harshad Sahasrabudhe, Douglas Vick, Marek Malac, Rajib Rahman, and Zubin Jacob

Sarang Pendharker is responsible for the full field simulations of Cherenkov radiation in the silicon plasmonic material seen in figure 3.4. The concepts of the origins of the thresholdless Cherenkov radiation phenomena in hyperbolic metamaterials discussed in the chapter are a result of many fruitful discussions between Sarang and myself. Harshad Sahasrabudhe and Rajib Rahman are responsible for the density functional theory calculations of the silicon dielectric permittivity seen in figure 3.1. Douglas Vick was heavily involved in the sample fabrication of the silicon films which he performed via focused ion beam. All other aspects, including writing of the full manuscript were performed by myself. Once again, Zubin Jacob and Marek Malac

were the supervising authors and were involved with the concept formation and finalizing the manuscript for publication.

Chapter 4 also consists of a collaborative research effort between the following authors:

- Prashant Shekhar, Sarang Pendharker, Douglas Vick, Marek Malac, and Zubin Jacob

Once again, concepts regarding the origins of thresholdless Cherenkov radiation phenomena in hyperbolic metamaterials discussed in the chapter are a result of many fruitful discussions between Sarang Pendharker and myself. Douglas Vick was once again an integral part of the sample fabrication process, helping to prepare the bismuth telluride sample via focused ion beam for observation in the transmission electron microscope. All other components of the chapter were completed by myself. Zubin Jacob and Marek Malac were involved with the concept formation and finalization of the chapter.

All of the work presented in this thesis is result of a collaboration from 3 institutions:

- University of Alberta, Department of Electrical and Computer Engineering, 9107 - 116 Street, T6G 2V4, Edmonton, Canada

- Nanotechnology Research Centre, Nat. Res. Council, 11421 Saskatchewan Dr NW, T6G 2M9, Edmonton, Alberta, Canada

- Birck Nanotechnology Center, School of Electrical and Computer Engineering, Purdue University, West Lafayette, IN 47906, USA

To my parents

For their unconditional love and unwavering support

.

Acknowledgements

First and foremost I would like to thank my supervisor Zubin Jacob. His vast knowledge, thoughtful insight, detailed guidance, and consistent encouragement have made completing this thesis possible. He has always put a strong focus on developing the scientific abilities of all his students, but it is his fearlessness and willingness to take risks that sets him apart. Early in my Master's degree I was struggling and considered quitting; Zubin's wise words convinced me to stay. Zubin, thank you for taking that chance on me, for that I am truly indebted to you.

I am similarly beholden to Marek Malac for taking under his a wing a student with no experimental experience and teaching him the complicated mechanisms of electron microscopy. Marek's breadth of experimental know-how, patience, light-heartedness, and hands-on approach to science proved to be a valuable learning experience. Meetings with Marek early in my PhD ended up shaping the entirety of the work in this thesis and I am grateful for his guidance.

I would also like to acknowledge Ward Newman, Sean Molesky, Cristian Cortes, Ryan Starko-Bowes, Farid Kahlor and Saman Jahani who have gone from colleagues in research to life-long friends. I did not know a single soul when I first moved to Edmonton but I can now trace all the friendships I have made back to this core group. Thank you for the discussions involving all things science and all things not!

I am also incredibly thankful for the support group surrounding me which made writing this thesis possible: Ying Tsui for your weekly guidance and collaborations, Sarang Pendharker for our scientific discussions and your contributions to this work, Kai Cui and Douglas Vick of NRC-NANO for your experimental expertise, and Pinder Bains for all your administrative assistance.

To my family, how incredibly lucky I am to have all of you in my life as a consistent source of inspiration and encouragement. To my mother, Alka, whose love of all things math and problem-solving rubbed off on me at a young age. I hope to one day emulate a fraction of her strong work ethic and ability to light up a room. To my father, Tushar, whose constant discussions about business pushed me directly into the sciences! All joking aside, my father's level-headedness, patience, and incredibly caring nature has been a constant source of stability in my life. To

my sister, Natasha, thank you for always sharing a laugh and making home feel close over long distances. I would also like to send a very warm thank you to my future mother-in-law, Ramila Patel, who welcomed me into her home with open arms and gave me a second family in Edmonton. Your nurturing has been the fuel to complete this work!

And last, but certainly not the least, to my partner Sheetal Patel whose presence made the entirety of my PhD a joy. Your sense of humour, caregiving nature, and acceptance of my ineptitudes have done more for me than I could ever express.

Contents

List of Figures

List of Abbreviations and Symbols

Abbreviation	Extended Form
BP	Bulk Plasmon
CR	Cherenkov Radiation
EELS	Electron Energy Loss Spectroscopy
EMT	Effective Medium Theory
ENZ	Epsilon-Near-Zero
EUV	Extreme Ultra-violet
HMM	Hyperbolic Metamaterial
HM	Hyperbolic Material
LDOS	Local Density of States
PDOS	Photonic Density of States
SPP	Surface Plasmon Polariton
TCR	Thresholdless Cherenkov Radiation
TEM	Transmission Electron Microscope
λ	Wavelength

Chapter 1

Introduction

1.1 Probing Optical Excitations at the Nanoscale

There is a strong drive for the continued development of nanotechnology in a variety of fields to discover new fundamental physical phenomena and develop new technological applications; the field of optics is no exception. Nano-optics, often referred to as nanophotonics, involves the understanding of photonic phenomena on the nanoscale beyond the diffraction limit of light. The roots of the now burgeoning field can be traced to the development of near-field optics in the mid 1980s. This, alongside ever improving nanofabrication techniques, allowed for increasingly complex nanoscale structures to control light at the nano-scale for a variety of applications. For example, nanophotonic structures such as optical microcavities, photonic crystals and more recently metamaterials and metasurfaces have lead to applications such as super-resolution lensing/microscopy [1, 2, 3], single molecule detection/analysis [4, 5], single-photon sources [6, 7], and the potential for optical networks via surface plasmon polariton excitations [8, 9, 10] .

The development of optical microscopy in particular has been a cornerstone in the field of nanophotonics. Initially, the understanding of the concepts of dispersion, diffraction and polarization in the 1700s and 1800s lead to the engineering of far-field optical microscopes. Improvements in instrumentation and technique eventually led to the ability to study physical processes on the nanometer scale, however resolutions were generally diffraction limited to the order of $\approx \lambda/2$. However, more recently, certain far-field optical microscopy techniques have been employed to beat the diffraction limit with a confocal microscopy setup including confocal fluorescence microscopy [11, 12], multiphoton spectroscopy [13], and stochastic optical reconstruction microscopy [14, 15] among many others [12]. Another avenue involves the direct excitation/detection of evanescently decaying near-fields in close

proximity to the sample known as near-field scanning optical microscopy (NSOM) [16, 17]. In NSOM a subwavelength tip is brought in close proximity to the sample where it brings, scatters and collects light before it evanescently decays to probe subwavelength excitations.

While optical microscopy techniques can probe and excite subwavelength optical phenomena and achieve subwavelength resolutions, they are hindered by the fact that they use sources with small incident wavevectors limiting their ability to probe deeply subwavelength features. As a result, there has been a sustained interest to use a different probe for optical excitations: the electron. The electron, with a de Broglie wavelength on the order of 0.01 nm, can not only be used to produce images with extremely high spatial resolutions but its inherent evanescent fields can couple to large wavevector (deeply subwavelength) optical excitations. In fact, some of the earliest work on the excitation of subwavelength optical surface waves on thin metal films were conducted by Ritchie with an electron probe [18], nearly 10 years before it was performed with visible light by Kretschmann and Raether in 1968 [19].

The most prominent technique for probing optical phenomena with electrons has been electron energy loss spectroscopy (EELS) in a transmission electron microscope (TEM). In EELS, a swift electron passes through a sample and experiences a measured energy loss (ΔE) that corresponds directly to the transfer of the energy to characteristic excitations within the photonic nanostructure [20]. The technique was originally developed by James Hillier and RF Baker in the 1940s [21] but did not see widespread use until the 1990s due to large advances in the instrumentation that continue to this day. For example, recently scanning TEM EELS (STEM-EELS), which uses a highly convergent beam with a point-like electron probe, has been used to spatially map plasmonic excitations on nanostructures with sub-nanometer spatial precision [22, 23, 24, 25, 26], probe higher order modes of nanodisks [27] and nanoparticles [28] as well as probe a series of phenomena interpreted to have quantum plasmonic behaviour [29, 30, 31, 32]. Additionally, EELS has been shown to provide insight into the nature of absorption versus scattering processes in nanostructures [33] as well as a direct relation to the photonic density of states (PDOS) [34, 35].

While STEM-EELS can spatially resolve nanoscale photonic excitations up to wavevectors several times past the light line, it provides no information about the band structure and dispersion of said excitations. Specifically, the large spatial resolution achieved with the narrow beam fundamentally limits the momentum (angular) resolution possible with such a technique due to the uncertainty principle. This problem was circumvented in the mid 70s where a wider parallel electron beam sacrificed some of the spatial resolution to measure both the transferred ΔE and momentum (Δk) from the electron to the sample to determine the characteristic energy-

momentum dispersion relation of plasmonic excitations [36, 37, 38]. This technique, known as momentum-resolved electron energy loss spectroscopy (k-EELS) has been somewhat forgotten since the early 1980s and has not seen much light of day in the field of nanophotonics, despite the success of STEM-EELS. This is especially interesting, as in its current state, STEM-EELS does not provide a smoking gun for quantum excitations as experimental measurements claiming so have also been described classically using the spatially dispersive properties of plasmonic excitations arising from the wavevector dependence of optical constants (non-local response) [39, 40, 41]. A momentum-resolved technique, such as k-EELS, can shed light and help resolve the debate on the nature of quantum versus nonlocal nanophotonic excitations not possible with STEM-EELS.

One of the primary goals of this thesis is to convince the reader that k-EELS is a fundamental tool for probing nanophotonic excitations that will lead to the continued development of the field of nanophotonics. It is shown that k-EELS has a fundamental link to nanophotonics and can be used to map momentum-resolved photonic density of states up to large wavevectors, it is demonstrated that k-eels is a versatile technique that can probe large regions of the spectrum from the visible to the EUV and also anisotropic structures, and that it can give key insights into the nature of classical, quantum and non-local optical phenomena from the measured band structure.

1.2 Thesis Overview

In this section we provide an overview of the thesis and highlight the primary material systems investigated with k-EELS in each chapter. Each system is an integral component to the current field of nanophotonics and, with the help of k-EELS, we gain new valuable insight into the nature of each of these systems and their potential for future applications.

In chapter 2 k-EELS is used to measure the momentum-resolved photonic density of states (k-PDOS) of plasmonic excitations in ultra-thin silver films. Although a direct connection between k-EELS and the k-PDOS has been theoretical proposed [34], experimental measurements confirming this fact have been lacking. Specifically, the established connection between k-EELS and the k-PDOS does not include the host of experimental systems with surface effects from finite structures integral to nanophotonics. It is for this reason that thin silver films, one of the most widely applied nanophotonic materials for its low loss plasmonic properties in the visible, is used to experimentally demonstrate the connection between k-EELS and the k-PDOS for the first time.

In chapter 3 we experimentally demonstrate via k-EELS that silicon can support
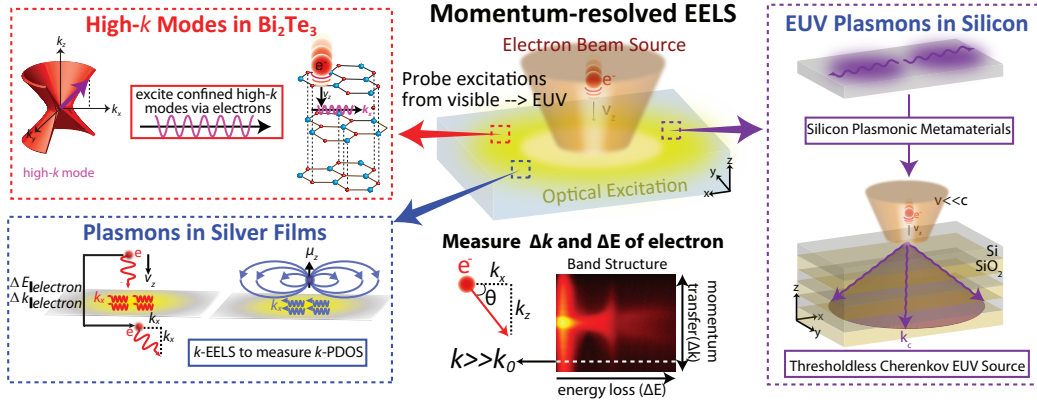
Figure 1.1: **Probing nanophotonic excitations with k-EELS.** In this thesis map the momentum-resolved photonic density of states (k-PDOS) of the surface plasmon polaritons of silver films (chapter 2), measure the high-k modes of Bi_2Te_3 (chapter 4) and the EUV plasmonic properties of silicon and silicon based metamaterials (chapter 3) with momentum-resolved electron energy loss spectroscopy (k-EELS).

plasmonic excitations at high energies in the EUV, beyond any other material popularly used in the field of nanophotonics. Interestingly, even though silicon is widely used as the material of choice for semiconductor and insulator applications in nanoelectronics [42], MEMS [43], solar cells [44] and on-chip photonics [45, 46, 47] its plasmonic properties in the EUV have remained largely ignored. Silicon's versatility as a material and its widespread use in industry made it a prime candidate for investigation, and in this chapter we highlight that silicon's capabilities can be extended further into the EUV regime for nanophotonic applications. k-EELS proved to be the tool of choice to probe such high energy excitations that are difficult to probe optically, and also allowed for the accurate mapping of the photonic bandstructure of the plasmonic excitations. In addition, in this chapter we also propose a tunable, broadband EUV radiation source in the form of thresholdless Cherenkov radiation in silicon plasmonic metamaterials.

Chapter 4 expands on the metamaterial ideas presented in chapter 3 by using k-EELS to probe the naturally occurring hyperbolic material (HM) Bi_2Te_3. Recently, interest in the avenue of naturally occurring HMs has gained traction as they have been seen to curtail the limitations of the finite size of the unit cell prevalent in artificial hyperbolic structures. Bi_2Te_3 is one of only 2 naturally occurring HMs that have recently been shown to possess hyperbolic behaviour in the visible, which is of course a prime regime of the spectrum for applications in nanophotonics. Hyperbolic materials are able to support photonic excitations up to large wavevectors (high-k modes) that are difficult to probe optically, and so, in this chapter, we perform the first measurement of the high-k modes and the hyperbolic cherenkov radiation mode

4

in Bi_2Te_3 with k-EELS.

The final chapter provides a brief summary and conclusion of the results presented in the thesis. Additionally, broad impacts of the work are discussed.

A series of appendices provide more detailed and expanded explanations of core concepts discussed throughout this thesis. This includes derivations of the electron energy loss function and scattering probability in uniaxial media (appendix A), the concept of the photonic density of states including a derivation of the electromagnetic Green's function (appendix B), surface plasmon excitations in drude metals (appendix C) as well as the behaviour of surface plasmons in nonlocal media (appendix D), an in depth discussion about hyperbolic metamaterials and their properties (appendix E), further details about the behaviour Cherenkov radiation in hyperbolic media (appendix F), additional details about the nature of the electron source and the electron energy loss spectrometer in a transmission electron microscope (appendix H) and finally a detailed methodology for preparing silicon samples for k-EELS analysis via focused ion beam milling (appendix I).

1.3   Scope

In order to achieve true nanoscale light confinement and control there are a series of challenges in the field of nanophotonics that must be addressed. In this thesis, we look at addressing 4 of these key challenges:

1. *Probing nanophotonic excitations at large momentum (high-k)*

2. *Probing nanophotonic excitations at high energy (from the deep ultra-violet to the extreme ultra-violet)*

3. *Characterization of new materials and metamaterial design to control nanophotonic excitations in the high energy/large momentum regime*

4. *Focused Application: Realizing a compact, tunable, broadband, and efficient EUV source*

Challenge 1 and 2 are a result of the limitations of optical nanophotonic spectroscopy techniques as outlined in section 1.1. In this thesis, we show that k-EELS is an essential tool in the field of nanophotonics to address both of these challenges simultaneously due to its ability to map photonic excitations to large energy and momentum. In chapter 3, we show how k-EELS can also be used to address the third challenge above, where we probe EUV plasmonic excitations in silicon that have not been explored previously. This can lead to the exploration of new materials and metamaterial designs for applications in EUV waveguides, lenses, sensors, detectors and sources that are sorely lacking.

Challenge 4 represents more a longterm challenge of this work to realize a truly efficient, broadband, tunable and compact EUV source. EUV sources are a keen area of interest in the field of nanophotonics for the next generation of nanolithography and metrology techniques to sustain Moore's law [48], applications in material science including electron spectroscopy techniques such as angle-resolved photoemission spectroscopy [49], as well for biomedical imaging [50].

Current forms of efficient EUV sources are large scale facility sources such as synchrotrons that are primarily used for high power applications. Additionally, laser produced plasma (LPP) EUV sources, which use a 20 KW CO_2 pulsed laser onto a tin target to create highly ionized plasmas [51, 52, 53], is the current state of the art for generating EUV radiation at 13.5 nm and is expected to be implemented for high volume use by 2020. LPP sources are promising as a high power EUV source, however they have some key challenges to overcome, including low efficiencies, incoherent EUV emission, and ablation debris compromising the cleanliness of the system.

While synchrotrons and LPP EUV sources are incredibly useful, they are not the most feasible forms of EUV sources for everyday lab use and tabletop applications due to their limited access, bulkiness and cost. KMLabs^{TM} currently manufactures commercial state of the art EUV tabletop sources that use a nonlinear effect known as high harmonic generation (HHG) to produce coherent EUV light [48]. A major drawback of the system however is its inefficiency of EUV light generation due to the higher power lasers required for its nonlinear process. In chapter 3 we propose a design for a compact EUV source as a potential stepping stone to address some of the major issues of tabletop EUV sources in the longterm. Such a source would be powered by low energy electrons instead of the energy intensive lasers required in nonlinear processes to potentially fill the void for a coherent, broadband, tunable, compact and efficient EUV source that is currently absent.

Chapter 2

Momentum-resolved Electron Energy Loss Spectroscopy for Mapping the Photonic Density of States

Strong nanoscale light-matter interaction is often accompanied by ultra-confined photonic modes and large momentum polaritons existing far beyond the light cone. A direct probe of such phenomena is difficult due to the momentum mismatch of these modes with free space light however, fast electron probes can reveal the fundamental quantum and spatially dispersive behavior of these excitations. In this chapter, we use momentum-resolved electron energy loss spectroscopy (k-EELS) in a transmission electron microscope to explore the optical response of plasmonic thin films including momentum transfer up to wavevectors (k) significantly exceeding the light line wave vector. We show close agreement between experimental k-EELS maps, theoretical simulations of fast electrons passing through thin films and the momentum-resolved photonic density of states (k-PDOS) dispersion. Although a direct link between k-EELS and the k-PDOS exists for an infinite medium, here we show fundamental differences between k-EELS measurements and the k-PDOS that must be taken into consideration for realistic finite structures with no translational invariance along the direction of electron motion. The results of this chapter paves the way for using k-EELS as the preeminent tool for mapping the k-PDOS of exotic phenomena with large momenta (high-k) such as hyperbolic polaritons and spatially-dispersive plasmons.

2.1 Introduction

Electron energy loss spectroscopy (EELS) in a transmission electron microscope (TEM) is an essential tool for nanophotonics due to its ability to probe charge density oscillations far past the light-line. In EELS, a swift electron passes through a sample and experiences a measured energy loss (ΔE) that corresponds directly to the transfer of the energy to characteristic excitations within the photonic nanostructure [20]. Recently, scanning TEM EELS (STEM-EELS) has been used to spatially map plasmonic excitations on nanostructures with sub-nanometer spatial precision [22, 23, 24, 25, 26], probe higher order modes of nanodisks [27] and nanoparticles [28] as well as probe a series of phenomena interpreted to have quantum plasmonic behaviour [29, 30, 31, 32]. However, in its current state, EELS does not provide a smoking gun for quantum excitations and similar experiments have also been described using the spatially dispersive properties of plasmonic excitations arising from the wavevector dependence of optical constants (non-local response). [39, 40, 41]. Additionally, EELS has been shown to provide insight into the nature of absorption versus scattering processes in nanostructures [33] as well as a direct relation to the photonic density of states (PDOS) [34, 35].

Optical techniques, which use sources with small incident wavevectors, are severely limited in their ability to measure the PDOS at large wavevectors in photonic nanostructures [22]. However, using electrons with techniques such as STEM-EELS and cathodoluminescence [54], this limitation can be surpassed as the inherently evanescent field of the electron can couple to large-wavevector excitations in the medium. Despite this, STEM-EELS provides no information about the band structure of the medium as the large spatial resolution achieved with the narrow beam fundamentally limits the momentum (angular) resolution possible with such a technique. This problem can be circumvented using momentum-resolved electron energy loss spectroscopy (k-EELS) where a wider parallel electron beam can measure both the transferred ΔE and momentum (Δk) from the electron to the sample to determine its characteristic energy-momentum dispersion relation [38, 36] (Figure 2.1(a)). Thus, k-EELS is a valuable tool for the k-space mapping of the PDOS for plasmonic systems up to large wavevectors (high-k) and can give key insights into classical, quantum [55] and non-local optical phenomena from the measured band structure.

In this chapter, we use k-EELS to measure the momentum-resolved photonic density of states (k-PDOS) of plasmonic excitations on ultra-thin silver films. We explore the role of electron energy and momentum loss as a function of thickness of the plasmonic film up to wavevectors 5 times past the light line. Although a direct connection between k-EELS and the k-PDOS has been theoretically proposed [34], experiments confirming this phenomenon have been lacking. Also note that the relation between the two quantities have been determined for an optical source

embedded in an infinite medium with translational invariance along the direction of electron motion. Thus, the established connection between k-EELS and the k-PDOS does not include the gamut of experimental systems with surface effects from finite structures integral to nanophotonics. Here, we highlight the fundamental differences between the k-PDOS and k-EELS in both energy and momentum space for such a finite system and experimentally demonstrate that k-EELS provides an accurate measure of the k-PDOS dispersion in energy-momentum space up to high-k not possible with other techniques. We also conclude that coupling to longitudinal modes is not observed in the local model of the k-PDOS for an optical source placed outside the medium but is apparent in the k-EELS spectrum. The use of k-EELS to map the k-PDOS to high-k can pave the way for exploring more exotic phenomena such as hyperbolic polaritons [56, 57, 58], slow light modes [59, 60] and strong coupling [61, 62]. It can also help shed light on questions related to non-local plasmonic excitations [63] and the nature of nonclassical vs. classical effects [64] effects in photonic nanostructures.

In the next section, we first outline a detailed methodology of the k-EELS system and setup as well as the sample fabrication before discussing our results in section 2.3 and section 2.4.

2.2 Performing k-EELS in the Transmission Electron Microscope: Experimental Setup and Sample Preparation

Performing k-EELS requires a notably different setup of the TEM compared to momentum-integrated EELS or STEM-EELS techniques (Figure 2.1 (a)).[1] For the work presented in this chapter, k-EELS was conducted with a Hitachi HF-3300 TEM/STEM with a cold field emission gun (CFEG) and a Gatan Image Filter (GIF) Tridiem^{TM} and the MAESTRO central computer control system [65]. The TEM operation in k-EELS uses a parallel electron beam (300 keV incident energy), unlike the point like probe of STEM-EELS with a highly convergent beam, in order to map k-space dispersion of the excitations. The use of a parallel beam versus a highly focused beam allows for the preservation of the angular scattering information essential for mapping the momentum loss characteristics of materials. The electrons with normal incidence pass through the sample and are scattered with a momentum transfer (Δk) and undergo an energy loss ($\Delta E = \hbar\omega$) corresponding directly to the momentum and energy of excitations in the sample. The electron energy loss is determined by the EEL spectrometer which applies a magnetic field perpendicular to the direction of electron motion, dispersing them in terms of their energy in

---

[1]An more detailed schematic of the general setup can be seen in figure 3.2 (a) of chapter 3

real space. Additionally, a rectangular EELS slit is placed in front of the EELS spectrometer in the diffraction plane so only electrons scattered along a certain direction in reciprocal space are collected and enter the EELS spectrometer. Note that this slit is placed perpendicular to the direction of the energy dispersion of the electrons performed by the EELS spectrometer. As a result, with proper calibration, the combination of the EELS slit and the EELS spectrometer disperses electrons on a 2D plane of a CCD camera with one axis corresponding to energy loss and one axis corresponding to the momentum loss experienced by the electron. This results in a a characteristic energy-momentum map of the probed sample. Note that if a certain crystal direction is desired to be probed, it is important to align the EELS slit with the desired crystal direction.

The k-EELS experiment performed in this chapter was completed on isotropic ultra-thin silver films. It was performed in diffraction mode with a 3 meter camera length and the sample was illuminated with a 0.1 μm diameter probe. The GIF was aligned using a series of energy selecting slits ranging from 10 eV to 2 eV and tuned to have non-isochromaticity to 1st and 2nd order well below tolerance (0.05 eV and 0.43 eV, respectively). Although the total GIF alignment was performed (including tuning for image distortions, achromaticity, and magnification), no energy selecting slit was used during the k-EELS acquisition. The parallel illumination allows for the entire k-EELS energy-momentum map image for each sample to be recorded using a 1 second acquisition time integrated over 5 images in the GIF spectroscopy mode. As the Ag thin films have isotropic plasmonic properties in k-space the direction of critical points of the Brillouin zone were not considered however they should be addressed for a non-isotropic plasmonic response. In addition, energy per pixel and momentum per pixel calibrations of the CCD camera were corroborated with a 200 nm thick silicon sample with a known lattice spacing. The energy-momentum maps measured for the thin films in this chapter resulted in energy and momentum resolutions of $\approx$ 0.03 μrad/channel and $\approx$ 0.01 eV/channel, respectively down to $\approx$ 1.2 eV until the ZLP onset.

In addition to the TEM setup itself, sample preparation for k-EELS experiments are also of great importance. Smooth, thin film samples with continuous and large grains are needed for k-EELS measurements. Such films limit the scattering of valence electrons from grain boundaries and the surface of the film, reducing the spurious background and improving momentum resolution. Additionally, the films must be deposited on soluble substrates, such as NaCl, in order to make the films free-standing to allow the fast electrons in the TEM to pass through the sample. For the work done in this chapter, smooth 11 nm, 25 nm and 40 nm thick polycrystalline silver films were prepared by electron beam evaporation onto NaCl substrates with a 1 nm Ge wetting layer [66] (FESEM images in Figure 2.3 insets). The NaCl

substrates, with (100) orientation, were freshly cleaved less than 1 minute before they were placed in a vacuum chamber. High purity 99.999% Ag and Ge sources were evaporated at ambient temperature $(12^oC - 18^oC)$ under high vacuum $(8 \times 10^{-7}$ torr) at 1Å/s and 0.1Å/s respectively. The samples were then floated off the substrate onto a TEM grid (inset Figure 2.1(a)) and inserted into the Hitachi HF-3300 TEM that has pressures $< 5 \times 10^{-8}$ torr measured near the specimen. The sample was exposed to atmosphere for approximately 20 minutes during the float off process.
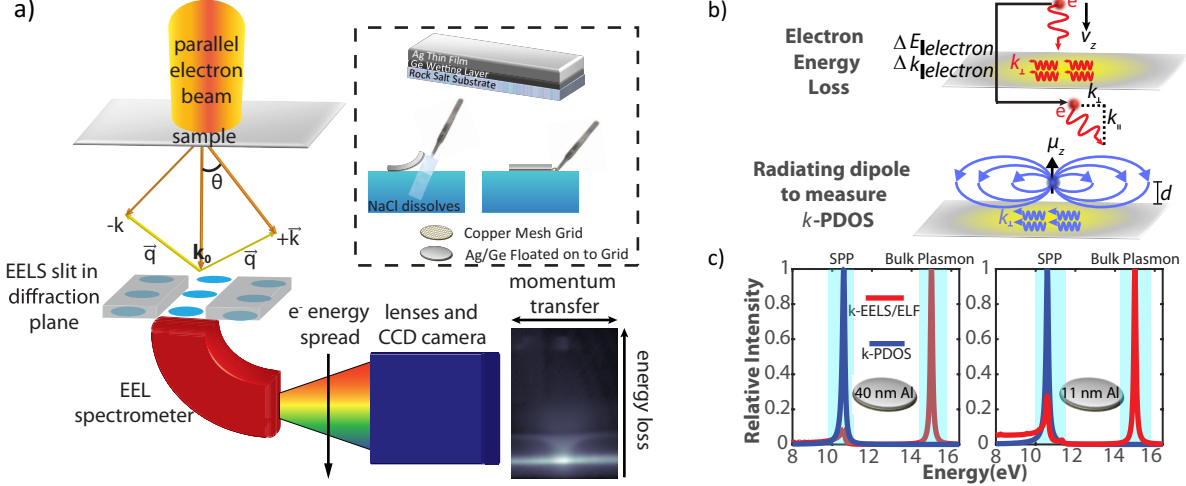
Figure 2.1: k-**EELS and** k-**PDOS** (a) The k-EELS experiment was performed with a Hitachi HF-3300 TEM with a GIF Tridiem$^{\text{TM}}$ in k-EELS mode at 300 keV incident energy with parallel illumination resulting in a quantitative energy-momentum dispersion map of the excitations in the sample. The inset shows the sample preparation for an e-beam evaporated Ag thin film with a Ge wetting layer onto a copper mesh grid. (b) Schematic illustrating k-EELS with electron motion along the direction of no translational invariance (top) and a radiating dipole above a medium (bottom) for determining optical excitations in a material. For k-EELS, we consider normally incident electrons with velocity v_z and probe momentum transfer parallel to the material interface $(\Delta k_\perp)$ and energy loss (ΔE) through the sample. The k-PDOS is measured by analyzing the power spectrum of a radiating dipole (with an oscillating source current) placed close to the material surface at a distance d. We only consider a dipole oriented perpendicular to the material interface (dipole moment μ only along z-direction).(c) The simulated relative k-EELS (determined by the energy loss function (ELF)) and the k-PDOS, integrated over the wavevector, for a 40 nm thick Al film (left) and a 11 nm thick Al film (right). The ELF is modeled for an electron with 300 keV incident energy while the k-PDOS is calculated for a radiating dipole 2 nm above the metal surface. For both thicknesses the ELF shows a strong peak at 15 eV corresponding to the bulk plasmon resonance of Al not seen in the k-PDOS. Both the k-PDOS and ELF show the surface plasmon polariton resonance at 10.6 eV. The aluminum is modeled with a simple Drude-like response with a plasma frequency (ω_p^{Al}) of 15 eV and a damping factor $(\gamma_p^{Al}) = 0.13$ eV.

2.3 Distinctions between the k-PDOS and k-EELS in Energy and Momentum Space

We now turn our attention to the theoretical foundations of the k-PDOS and its relation to k-EELS measurements. The k-PDOS (appendix B) provides a framework that leads to a direct connection to Fermi's golden rule, making it a valuable tool for spontaneous and thermal emission engineering [56, 57, 67]. Here, we consider the k-PDOS for an optical source in vacuum above the medium of interest akin to many nanophotonic systems (Figure 2.1 (b) bottom). It captures the near-field interactions with photonic nanostructures from the power dissipated by a stationary oscillating electric dipole: $P = \frac{\omega}{2} Im(\mu^* \cdot \vec{E})$ where $\vec{E}$ is the electric field at the dipole position (d) produced by an oscillating current source $j_{pdos}(z,t) = -i\omega\mu e^{-i\omega t}\delta(z-d)\delta(x)\delta(y)$ [68] and μ is the dipole moment.

Although k-EELS measurements and the k-PDOS are comparable quantities, for a system with no translational invariance along the direction of electron motion, several key distinctions between the two quantities exist due to the different nature of their source excitations. In stark contrast to the stationary radiating dipole source above the medium in the k-PDOS, measurements made by k-EELS require a formalism for the scattering of a swift electron as it moves through matter (appendix A). The energy loss and transferred momentum of an electron moving through a medium is described by the energy loss function (ELF) [69] which is the work done by the retarding force of the fields induced (E_{ind}) by the electron: $U = \int d^3r \int dt E_{ind}(r,t) \cdot j_{eels}(r,t)$ where r is the spatial position and j_{eels} is the source current [70]. Note, unlike the oscillating current source in the PDOS (j_{pdos}), the source current in k-EELS is that of a moving charge: $j_{eels} = ev_z\delta(x)\delta(y)\delta(z-v_zt)$ where v_z is the velocity of the electron perpendicular to the medium interface [70] (Figure 2.1 (b) top). This contrasting nature of the source excitations for a finite structure consequently leads to fundamental variations between the k-PDOS and k-EELS (as determined by the ELF) in both energy and momentum space.

Figure 2.1(c) contrasts the k-PDOS and the ELF of an aluminum film as a function of film thickness and highlights a key difference between the two quantities in energy space: the local k-PDOS (integrated over the wavevector) for an emitter above the medium does not show any signature of the bulk plasmon resonance (appendix C) at 15 eV although it is a strong peak in the ELF for both the 11 nm and 40 nm thickness. Unlike a moving electron, the stationary radiating dipole source above the film has no longitudinal electric fields and therefore is unable to couple to any epsilon-near-zero resonances [71, 72] (bulk charge density excitations in a medium where the permittivity approaches 0) due to their longitudinal nature. Additionally, we observe that the ELF sees an increase in intensity at the surface

plasmon polariton (SPP) energy (10.6 eV) relative to the bulk plasmon as the film thickness is decreased due to the electron probing more effective surface compared to the bulk of the medium. This trade-off between the bulk and surface contribution to electron energy losses is known as the Begrenzungs effect [20]. Although the ELF leads to a direct interpretation of the k-PDOS in energy space for an infinite medium, such intensity fluctuations of the surface plasmon as a function of film thickness do not occur in the local k-PDOS as it does not couple to the bulk plasmon for an emitter placed outside a finite structure.
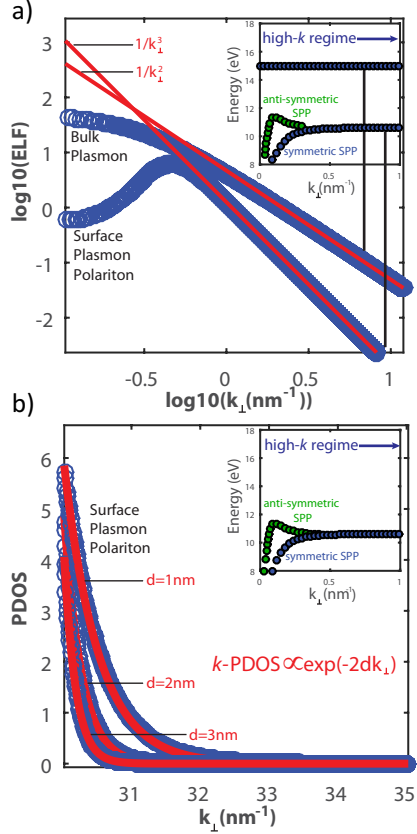
Figure 2.2: k-**PDOS and** k-**EELS Scaling with Wavevector** The scaling of the k-EELS (as determined by the ELF) (a) and k-PDOS (b) with respect to the wavevector parallel to the surface ($k_\perp$) is shown for an 11 nm thick Al film. At large wavevectors the ELF scales as $1/k^2$ and $1/k^3$ for the bulk and surface plasmon polariton, respectively. The k-PDOS scaling with wavevector for the surface plasmon is seen to scale as $\exp(-2dk)$ where d is the distance of the dipole from the top surface. The insets in (a) and (b) display the simulated k-EELS and k-PDOS dispersion, respectively. Note that both the k-EELS and k-PDOS show the symmetric and anti-symmetric surface plasmon in the band structure but only k-EELS shows the bulk plasmon dispersion at 15 eV.

We now turn our attention to the nature of the ELF and k-PDOS in momentum space with particular emphasis on the fundamentally different high-k behaviour of

plasmonic excitations. First, we consider the contribution to the k-PDOS ($\rho(\omega, d, k)$) for an emitter above a thin metal film from only the SPP (as there is no coupling to the bulk plasmon) and its dependence on the wavevector in the plane parallel to the material interface ($k_\perp$) [68]:

$$\rho_{spp}(\omega, d, k_{spp}) = \frac{\pi^2 c^2}{\omega} Re \left(\frac{\sqrt{-\epsilon_m} k_{sp}^5}{1 - \epsilon_m} e^{-2\sqrt{\frac{-1}{\epsilon_m}} k_{sp} d} \right) \tag{2.1}$$

where ρ_{spp} is the surface plasmon contribution to the k-PDOS, c is the speed of light in vacuum, $k_\perp = k_{spp}$ is the surface plasmon wavevector and ϵ_m is the permittivity of the metal. A similar expression can be derived for the ELF in the limit of high-k for a thin metal slab surrounded by vacuum showing its dependence on the wavevector for both the bulk and surface plasmon contributions:

$$
\begin{aligned}
ELF_{bulk} &= \frac{t}{k_\perp^2} \left(\frac{v_z^2}{c^2} - \frac{1}{\epsilon_m} \right) \\
ELF_{surf} &= \frac{2}{k_\perp^3 \epsilon_m} \frac{\left[-f^2.(1 + \epsilon_m) + \alpha - f(b^+ + b^-) \right] \alpha}{(1 + \epsilon_m)^2 f^2 - \alpha^2}
\end{aligned}
\tag{2.2}
$$

where t is the slab thickness, $\alpha = (1 - \epsilon_m)$, $f = \exp\left(\sqrt{k_\perp^2 - \epsilon_m \omega^2 / c^2} t \right)$, and $b^\pm = \exp\left(\frac{\pm \iota \omega t}{v_z} \right)$. It is clear from equation 2.1 and equation 2.2 that the scaling of the plasmonic excitations differ significantly for the ELF and k-PDOS intensity with respect to $k_\perp$. Figure 2.2(a) plots the ELF versus $k_\perp$ at the surface plasmon and bulk plasmon energy of Al in log scale. We note, that in the limit of large k, $ELF_{bulk} \propto 1/k_\perp^2$ and $ELF_{surf} \propto 1/k_\perp^3$. Conversely, at high-$k$, the PDOS scales such that PDOS $\propto \exp(-2dk_\perp)$ (Figure 2.2(b)). Thus, there is an increasing difference in momentum space between the ELF and the k-PDOS for finite structures as k is increased that must be taken into consideration when performing k-EELS measurements.[2]

Although there exist some fundamental differences between k-EELS and the k-PDOS magnitudes for the system discussed above, once these theoretical differences are taken into account, k-EELS measurements can help to map the local k-PDOS as well as the energy-momentum band structure of plasmonic/polaritonic excitations. The insets of Figure 2.2(a,b) clearly highlight the ability of k-EELS to map the energy-momentum dispersion of the k-PDOS to great accuracy. The insets show the energy-momentum dispersion of the SPP, the anti-symmetric SPP, and, in the case of the ELF, the bulk plasmon for a 11 nm thick aluminum film. In the particular case of the SPP, both the k-PDOS and k-EELS show the gradual convergence of

---

[2]Note, experimental verification of this scaling is seen in chapter 3 in figure 3.3 for the plasmonic excitations in silicon films.

the SPP resonance to its plateau energy at 10.6 eV with one to one correspondence from the low-k to high-k regime.

2.4 Dispersion mapping the k-PDOS with k-EELS

In this section, we perform k-EELS as a function of film thickness to determine the k-PDOS dispersion of the SPP. We fabricated 11 nm, 25 nm and 40 nm continuous large grain sized free standing silver films. Note, while analysis with Al films was considered in the previous sections to highlight the effects of the bulk plasmon, we switch to Ag films in experiment for two key reasons: the wide use of Ag in nanophotonics systems due to plasmonic excitations in the visible regime and the fact that there are no bulk plasmon contributions for Ag close to the SPP energy. Detailed experimental methods, including fabrication of free standing Ag films and the k-EELS specifications, are outlined in section 2.2.

Figure 2.3 shows the experimentally measured relative k-EELS scattering probability at different scattering angles (corresponding to transferred momentum k) for an 11 nm, 25 nm and 40 nm thick Ag film on a 1 nm Ge wetting layer. The insets in the top row of Figure 2.4 (a, b, c) show the raw experimental E-k dispersion map with energy loss in eV and momentum transfer in μrad. The intense band evident at 0 eV across all scattering angles is the zero-loss-peak (ZLP) representing unscattered and elastically scattered fast electrons present in all k-EELS spectra. The bright band at $\approx$3-3.5 eV (marked by the dashed white line) is the SPP peak of Ag and the series of bands in the 4-6 eV range evident at lower scattering angles ($\approx$5-10μrad) correspond to the interband transitions in Ag. Figure 2.3 is plotted by taking 1D line profiles along the designated scattering angles of the E-k map. The strongest peak in the experimental energy loss spectra is that of the surface plasmon of silver as is expected for relatively thin films ($<$ 100 nm thick) where surface loss contributions dominate bulk losses. The relative scattering intensity of the surface plasmon also decreases with increasing transferred momentum for all thicknesses as expected due to the scaling of the ELF with k observed in Figure 2.2 (a) and equation 2.2.

Direct proof of the ability of k-EELS to map the k-PDOS dispersion from low-k to high-k is demonstrated in Figure 2.4 as seen by the strong match between the k-EELS experiment, ELF and the k-PDOS while mapping the SPP dispersion of Ag. (d), (e), and (f) show the near perfect agreement between the theoretical ELF and the k-PDOS across all thicknesses and k implying the ability of the ELF (and therefore k-EELS measurements) to map the k-PDOS dispersion to high-k. This is further corroborated by the experimental k-EELS results shown in (a), (b) and (c) which shows a strong correspondence with the theory. Not only do the k-EELS
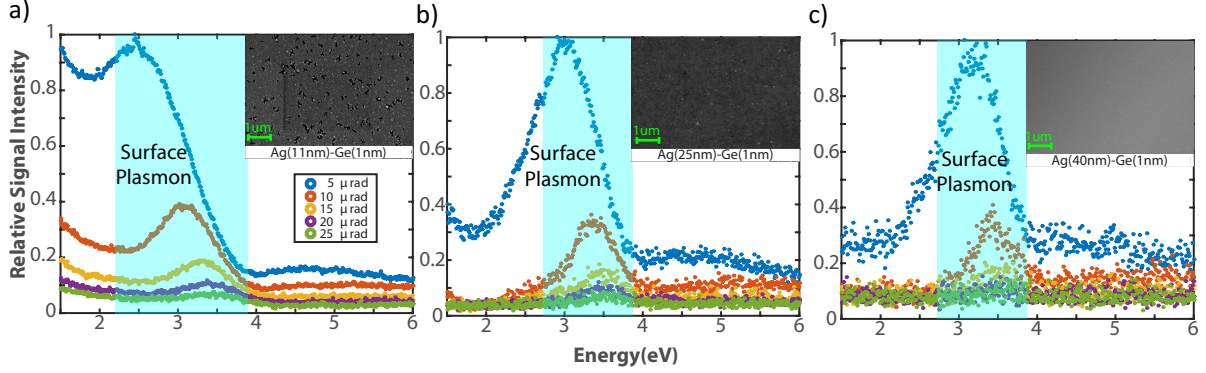
Figure 2.3: *k*-**EELS on Silver Films.** Relative experimental *k*-EELS scattering intensity at select scattering angles for an 11 nm (a) , 25 nm (b) and a 40 nm (c) Ag film. The film was deposited with 1 nm Ge wetting layer onto NaCl single crystals. A distinct peak (2.5 eV-3.5 eV) and a fainter peak at lower angles (4 eV-6 eV) correspond to the surface plasmon and the interband transitions of silver respectively. The inset is a scanning electron microscope image of the top surface of the silver film.

measurements and ELF capture the broad *k*-PDOS dispersion, but also the nuanced changes in the SPP dispersion as the film thicknesses is increased. This is evident as the SPP dispersion profile for the 11 nm film (Figure 2.4 (a,d)) is shifted to higher momentum at lower energies and shows a more gradual convergence to the surface plasmon plateau energy (3.5 eV) than either the 25 nm (Figure 2.4 (b,e)) or 40 nm (Figure 2.4 (c,f)) film in both theory and experiment. The slight shift of the SPP dispersion to lower momentum by ≈2 *μ*rad in experiment versus simulation is likely due to oxidation of the Ag film not included in the simulation.

In conclusion, despite being fundamentally different quantities for realistic finite structures with no translational invariance along the path of electron motion, *k*-EELS is a valuable tool for mapping the *k*-PDOS dispersion in photonic nanostructures from the low-*k* to high-*k* regime not possible with other techniques. The versatility of the *k*-EELS approach allows for mapping the *k*-PDOS dispersion for a wide variety of photonic nanostructures including photonic crystals, 2D materials, metamaterials, and metasurfaces including periodic arrays of structures composed of the wide array of nano plasmonic antennas. However, for periodic structures, the interplay between the periodicity, angular extent of the zero loss peak and the dynamic range of the *k*-EELS spectrum has to be optimized. Thus, *k*-EELS is a valuable tool for the *k*-space engineering of many exotic phenomena in nanophotonics including Cherenkov radiation [73], slow-light modes [59, 60], non-local plasmonic excitations [63], hyperbolic modes [56, 57, 58], and strong coupling [61, 62].
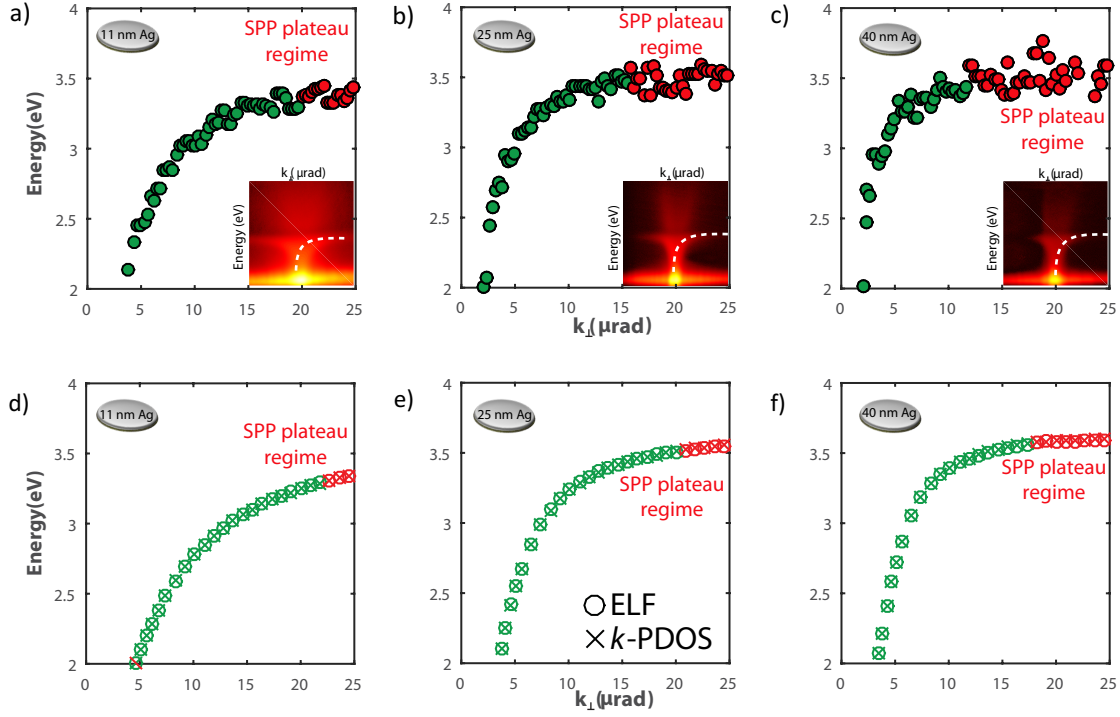
Figure 2.4: *k*-**PDOS Dispersion from *k*-EELS.** Experimental and theoretical *k*-EELS dispersion maps for an 11 nm (a,d), 25 nm (b,e) and a 40 nm thick (c,f) Ag film on a 1 nm Ge wetting layer. TOP: Energy-Momentum dispersion of the silver film from the raw experimental EELS data. A clear SPP dispersion is observed. Inset shows the generated experimental energy-momentum map with a dashed line indicating the SPP scattering intensity. Note the bright band at 0 eV in the inset corresponds to the zero-loss peak (ZLP). BOTTOM: Theoretical *k*-EELS scattering probability and *k*-PDOS for the various Ag films generating an energy-momentum map. A strong correspondence between the experimental and the simulated *k*-EELS and *k*-PDOS is observed for mapping the SPP dispersions. Note, that the SPP plateau appears at decreasing $k_\perp$ as the sample thickness increases in both theory and experiment.

17

Chapter 3

EUV Plasmonics and Cherenkov Radiation in Silicon

Silicon is the key material of choice in industry for applications in nano-electronics, on-chip photonics, solar cells and MEMS technologies. Interestingly, in this chapter, we show that silicon can also support surface and bulk plasmons in the EUV regime not possible with conventional plasmonic materials. We expand on the techniques and ideas presented in chapter 2 and use relativistic electrons to experimentally probe the plasmonic properties of silicon via k-EELS. Additionally, we propose a feasible EUV radiation source using the high energy plasmonic effect in silicon plasmonic metamaterials.

The goal of this chapter is to provide a stepping stone for the design and fabrication EUV plasmonic nanostructures that are severely lacking. Such structures include EUV waveguides, metamaterials and metasurfaces for potential applications in biotechnology, EUV lensing for imaging and lithography and integrated EUV sources. Additionally, this chapter highlights the ability of k-EELS to probe high energy excitations difficult to perform optically and addresses the need for advancing the current state of characterization tools in the field of nanophotonic to discover unique photonic excitations inside matter.

3.1 Introduction

Arrows indicate indirect interband transitions that are very weak in the EUV. This results in a sea of unbound electrons in the valence band that lead to silicon's metallic character [75].

Silicon is the most widely used material for applications in nano-electronics [42], photovoltaics [44], MEMs technologies [43], and on-chip photonics [45, 46, 47]. Its dominance in industry stems from multiple factors including the possibility to control
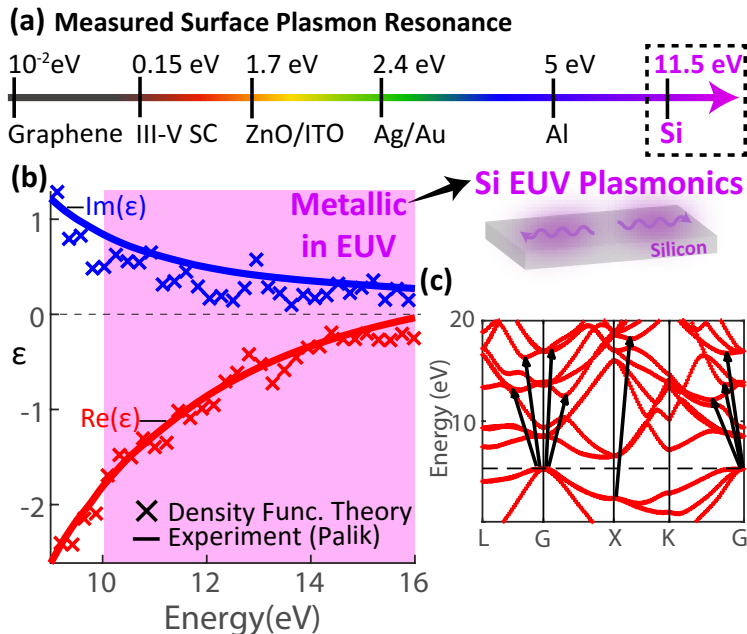
Figure 3.1: **Plasmonics across the EM Spectrum.** (a) The measured surface plasmon resonance for various materials across the EM spectrum from the terahertz (10^{-2} eV / 124 μm) to the EUV (11.5 eV / 107 nm). Doped semiconductors are limited to the mid-infrared region whereas transparent conducting oxides have plasmon resonances in the near-infrared. Alternative plasmonic media and conventional materials (Ag, Au) work well in the visible range. Al is the material of choice for UV applications. Plasmonic behaviour in the EUV has remained largely ignored. Here, we explore silicon for its EUV plasmonic properties at more than double the energy of aluminum. (b) Experimental (from Palik [74]) and theoretical (density functional theory (DFT) calculations with the GW approximation[1]) of the permittivity of silicon showing it's metallic character in the EUV ($\epsilon < 0$ in the 10-16 eV (124 - 77 nm) regime). (c) Electronic band structure of silicon calculated with DFT + GW approximations[1]. Arrows indicate indirect interband transitions that are very weak in the EUV. This results in a sea of unbound electrons in the valence band that lead to silicon's metallic character [75].

its crystallinity, tailoring of its conducting properties via doping, cost-effectiveness and availability as well as its high purity. Although universally known for its insulating and semiconducting properties, the goal of this chapter is to explore and exploit silicon's metallic and plasmonic properties which have remained largely ignored.

The plasmonic properties of a variety of different materials have been explored across the electromagnetic (EM) spectrum [76] (figure 3.1 (a)). This includes plasmons on graphene in the THz regime [77], highly doped III-V semiconductors that support plasmons in the infrared [78, 62], and the universally used plasmonic materials Ag and Au in the visible [79]. Aluminum has been the most widely explored plasmonic material at UV frequencies for applications such as tunable, integratable

surface plasmon sources [80, 81], medical assays and biotechnology applications with fluorophores [82], as well as lensing for imaging applications and optical lithography [83]. While aluminum has shown some promise in the ≈ 5 eV (248 nm) regime, achieving plasmonic effects at higher energies in the deep ultra-violet (DUV) and extreme-ultra-violet (EUV) is an open problem.

In this chapter, we show that extreme ultra-violet plasmons supported by silicon can pave the way for EUV waveguides, metamaterials and devices not possible with conventional plasmonic materials. We study the evolution of the plasmonic behavior in silicon thin films down to 60 nm and probe the photonic band structure of silicon in the EUV up to 5 times past the light line. This is made possible by probing silicon with relativistic electrons using momentum-resolved electron energy loss spectroscopy (k-EELS). Unlike the more traditional spatially resolved electron energy loss techniques [55], in this work, not only the energy but also the momentum dispersion of the EUV plasmonic excitations are mapped. We also show excellent agreement of our experimental results with first principles quantum density functional theory calculations as well as macroscopic electrodynamic electron energy loss theory. The silicon SPP is shown to have a resonance condition at approximately 11.5 eV (107 nm), more than twice as high in energy as what has been measured with aluminum for applications in the UV. Finally, we propose an EUV radiation source by exploiting the EUV plasmonic properties of undoped silicon. Our proposed EUV source is tunable and broadband, and uses thresholdless Cherenkov radiation in silicon plasmonic hyperbolic metamaterials. Our work paves the way for the field of EUV plasmonic devices with silicon.

The energy scales of the surface plasmon polariton (SPP) for silicon is between $4 \text{ eV} \leq \text{E} \leq 11.5 \text{ eV}$ ($310 \text{ nm} \leq \lambda \leq 107 \text{ nm}$) while the bulk plasmon (BP) exists at $\text{E} = 16 \text{ eV}$ ($\lambda = 77 \text{ nm}$). Even though previous work has shed light on the existence of such metallic behavior in bulk silicon [37], it's an open question whether plasmonic behavior would persist for nanoscale structures. In this work, we specifically focus on the thickness evolution of plasmonic behavior in silicon thin films which is in agreement with Drude metallic behavior. This validates that deep subwavelength excitations in the EUV regime are indeed possible for paving the way to EUV plasmonics.

Experimental measurement of the silicon permittivity at high energies [74] agrees strongly with our density functional theory (DFT) calculations under the GW approximation [84] (figure 3.1 (b)).[1]. Silicon's metallic character in the EUV is a result

---

[1] These calculations were performed by Harshad Sahasrahbudhe and Rajib Rahman at Purdue University. The dielectric constant is calculated using the GW approximation in the Vienna Ab initio simulation package (VASP [84]), where G is the single particle Green's function, and W is the screened Coulomb interaction between electrons. Quasiparticle energies and wavefunctions corresponding to unoccupied orbitals (bands) are obtained using this method. The dielectric constant is then evaluated using the wavefunctions and their derivatives with respect to momentum. In this

of the unbound nature of its valence electrons arising from the weak interband transitions strengths from the valence to the conduction band [75]. In fact, this leads to a nearly freely moving sea of electrons in the valence band that can support surface plasmon excitations from the free charge carrier oscillations. This is in contrast to the visible region of the spectrum where prominent interband transitions lead to strongly bound electron-hole pairs between the valence and conduction band which eliminates its metallic character [75, 85].

3.2 EUV Surface and Bulk Plasmons in Silicon Measured with k-EELS

We measure the EUV plasmonic properties of silicon with relativistic electrons and momentum-resolved electron energy loss spectroscopy (k-EELS) in a transmission electron microscope. Unlike traditional electron energy loss spectroscopy (EELS) techniques where only the amount of energy loss is measured, k-EELS probes both the energy and momentum transfer of the electron. The information on momentum loss is obtained by measuring the scattering angle (θ) of the electron after passing through the sample[2] (figure 3.2 (a)). Note the energy and momentum lost by the incident electron corresponds directly to the energy and momentum carried away by the excitations within the sample. Thus, the major advantage of k-EELS is the ability to map the photonic/polaritonic band structure and clearly identify photonic excitations such as Cherenkov radiation, waveguide modes and surface/bulk plasmons.

Figure 3.2 (b), (c), and (d) shows the measured photonic band structure as a function of thickness (200 nm, 100 nm and 60 nm) for free standing silicon films[3]. The samples are prepared via focused ion beam milling (FIB) and mounted to a TEM grid[4] to create free-standing structures (inset figure 3.2 (f), (g)). The band structure for all three films is measured using k-EELS up to an electron scattering

---

approximation, the self-energy (Σ) of the many-body electron system is truncated to the first order in G. A partially self-consistent method (GW_0 algorithm in VASP) is used, which is shown to closely match experiments, where G and Σ are updated until convergence and W is fixed.

Interestingly our calculations using the Bethe-Salpeter Equation (BSE), which describe electron-hole bound states, calculates the experimental permittivity of silicon well at lower energies but begins to deviate at energies into the UV regime and higher. Conversely, the DFT with the GW approximation shows a much stronger match to the experimental data at high energies which suggests that the electron-hole pairs are not strongly bound but move freely at higher energies.

[2]The details of the k-EELS methodology is very similar to what was outlined chapter 2. The incident electrons were traveling parallel to the c-axis perpendicular to the (100) silicon plane.

[3]The experimental data shown is a result of 10 integrated measurements on the silicon sample, where the filled circle is the average of the peaks taken in the 10 images. The error bars are 2 standard deviations above and below the average, indicating a 95% confidence interval for the data.

[4]FIB was performed with the aid of Douglas Vick at NRC-Nano. Details of the process can be seen in appendix I

21
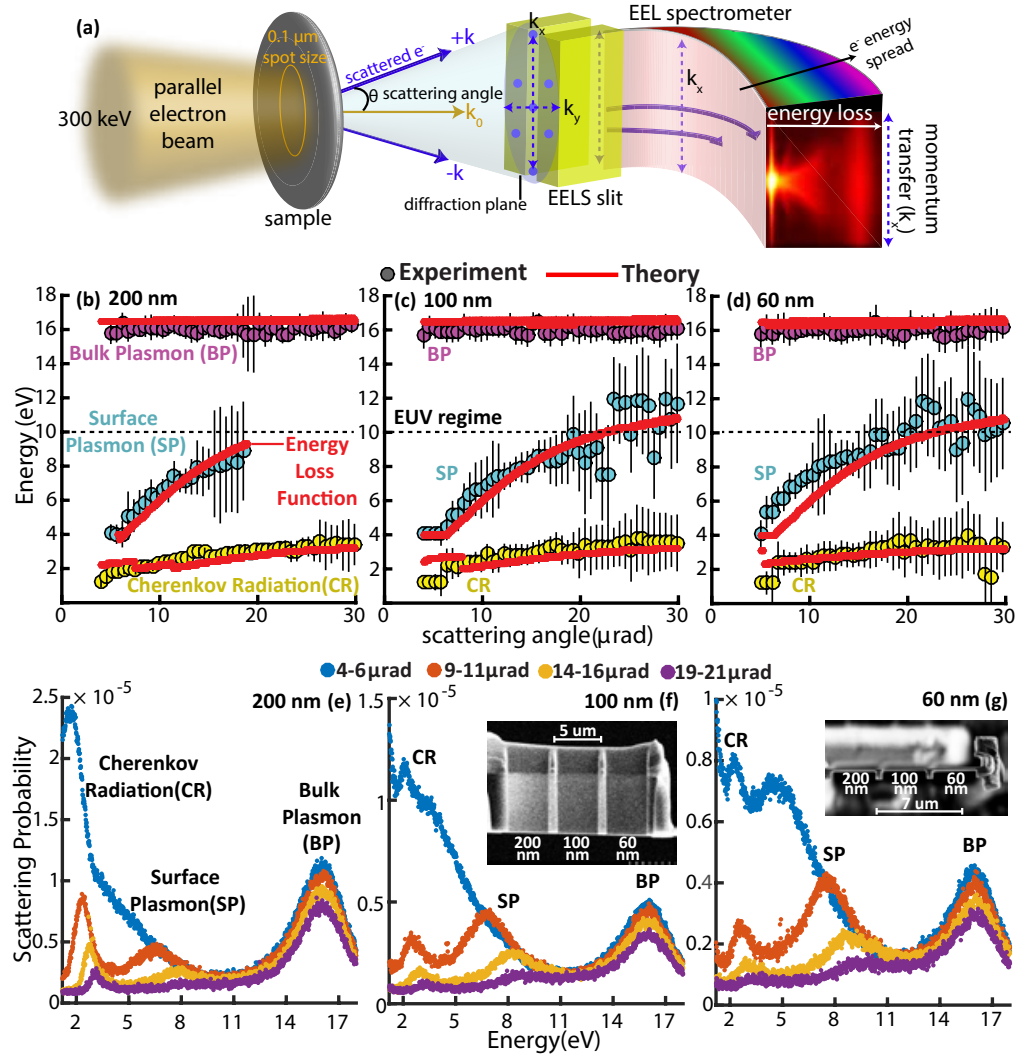
Figure 3.2: **EUV plasmons and Cherenkov radiation in silicon measured with k-EELS.** (a) Schematic showing the key components of the k-EELS technique for measuring the momentum-resolved photonic band structure of silicon. The k-EELS experiment was performed with a Hitachi HF-3300 TEM with a GIF Tridiem in k-EELS mode at 300 keV incident energy with parallel illumination resulting in a quantitative energy-momentum dispersion map of the excitations in the sample[2]. The photonic band structure of 200 nm (b) 100 nm (c) and 60 nm (d) thick silicon films measured with k-EELS (error bars show 95% confidence interval[3]). All three films show evidence of the bulk plasmon at (≈ 16 eV) and the surface plasmon at ($\approx$ 4-11.5 eV) in the EUV as well as Cherenkov radiation in the visible in the ($\approx$ 2-4 eV) region mapped to large scattering angles (large momentum with $k > 5 * k_0$). A good agreement to the macroscopic electrodynamic energy loss function (red line) is seen for all three thicknesses. (e),(f), and (g) show the electron scattering probability for the 3 excitations as measured by k-EELS integrated over the indicated scattering angles for the 200nm, 100 nm and 60 nm silicon films, respectively. Insets in (f) and (g) show SEM images of the free standing silicon films prepared via FIB milling and mounted to the TEM grid (details in appendix I).

22

angle of $\theta = 30\mu rad$ ($k_x \approx 0.1 nm^{-1}$) at 300 keV incident energy and probes the deep near field up to 5 times past the light line.

We now explain the physical origin of the three branches seen in the band structure data in figure 3.2 (b), (c), and (d). The dispersionless flat-band at 16 eV (77 nm) in all three films is the bulk plasmon (BP) excitation of silicon (ω_p^{Si}). The BP is a longitudinal resonance that is difficult to probe optically and occurs at the point $\epsilon_{Si} \to 0$ (figure 3.1 (b)) well into the EUV. We emphasize that bulk longitudinal plasma oscillations, even for aluminum, occur in this high energy regime. However, for waveguiding and nano-antenna applications, surface plasmon polaritons are necessary which do not exist in the EUV regime in the widely used plasmonic metals.

The highly dispersive band between $\approx$ 4-9 eV for the 200 nm film and $\approx$ 4-11.5 eV (107 nm - 310 nm) in the 100 nm and 60 nm film is the measured surface plasmon polariton (SPP) excitation of silicon in the EUV. Interestingly, surface excitations are stronger as compared to bulk excitations for thinner films in all EELS measurements due to the Bergrenzungs effect [22, 20]. As a result, the surface plasmon scattering intensity is large enough in the thinner 100 nm and 60 nm film to be probed into EUV energies. Interestingly, we note that $\omega_{sp}^{Si} = \omega_p^{Si}/\sqrt{2} \approx 11.5$ eV, which is indicative that silicon is a Drude-like metal in the EUV in agreement with DFT calculations. This is in fundamental contrast to the DC semiconducting properties or transparent insulator-like optical properties of silicon at the telecommunication wavelengths.

We immediately note that the measured EUV SPP resonance energy of silicon ($\approx$ 11.5 eV/107 nm) is more than double of what has been observed with aluminum, the traditional material for high energy plasmonic applications. Furthermore, figure 3.2 (e),(f) and (g) highlights the highly dispersive nature of the SPP (blue-shifting of the peak with increasing scattering angle) for the three silicon films across the untapped 5 - 11.5 eV range. Note, that the dispersive properties of the SPP would be hidden in traditional EELS techniques but is captured here by k-EELS. The k-EELS measurements prove that the SPP of silicon can be probed to an entirely new region of the spectrum as compared to other plasmonic materials opening the door for a wide range of plasmonic applications in the EUV.

To prove conclusively that we are observing bulk and surface plasmons in the measured data, we conduct simulations of the macroscopic electrodynamic electron energy loss function [87] (appendix A in silicon for electrons normally incident to the sample. The measured data show a strong match with the theoretical calculations (red line in figure 3.2 (b), (c), (d)). The energy loss function has been shown to be analogous to the photonic density of states [34, 86] and is thus an excellent quantifier for probing photonic excitations. Slight deviations at small scattering angles of

23
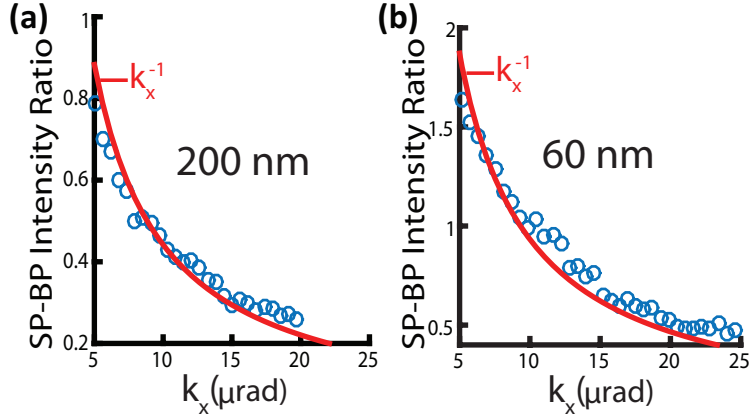
Figure 3.3: *k*-**EELS scattering intensity scaling with momentum** (*k*) The experimental (blue circles) surface plasmon (SP) and the bulk plasmon (BP) scattering peak intensity ratio is plotted as a function of k_x (scattering angle) for the 200 nm (a) and 60 nm (b) silicon films. In macroscopic electrodynamic electron energy loss theory, surface contributions (such as the SP) and bulk contributions (such as the BP) scale with momentum as k^{-3} and k^{-2}, respectively [86, 20]. As a result, the *k*-space scaling of the ratio of the surface to bulk intensity goes as k^{-1}. This is evident from the red line in the figure. We can thus unambiguously separate the surface plasmon polariton and bulk plasmon contributions using k-EELS.

the experimental surface plasmon peak from the predicted theoretical energy loss function in the 60 nm film is likely due to Ga+ implantation ($\approx$ 1-2 nm) during the FIB sample fabrication process and surface oxidation. Thinner samples, which are more sensitive to surface energy loss excitations, are more affected by such impurities along the sample surface. Recorded uncertainties (error bars) in the measured EUV plasmonic resonances increases at large scattering angles due to the decrease in probability of scattering[5].

Fig. 3 shows the ratio of the bulk and surface scattering probability scaling with momentum for silicon. Theoretical predictions reveal a k^{-3} dependence for bulk plasmons and k^{-2} scaling for surface plasmons [86, 20] (figure 3.3). The excellent

---

[5]It is evident from figure 3.2 (b) that there is an increased uncertainty in the *k*-EELS measurement at larger scattering angles. This is a result of the decreased signal to noise ratio (SNR) of the EELS measurement at large scattering angle (large *k*) due to the inherent *k*-space scaling of of EELS signal intensity (figure 3.3).

Furthermore, an increased uncertainty is observed in the surface contributions (the SP) as compared to the bulk contributions (the BP) in figure 3.2 (b) as the scattering angle increases. This is due to the fact that the surface scattering intensity decreases with scattering angle exponentially faster than bulk contributions (k^{-3} versus k^{-2}, respectively) (figure 3.3). This leads to a relatively lower SNR for the surface contributions compared to bulk contributions leading to increased uncertainty for surface contributions at larger *k*.

Additionally, an overall increase in the measurement uncertainty is observed for thinner films as compared to the thicker silicon films. This is a result of the inelastic mean free path of silicon ($\approx$ 180 nm for 300 keV electrons) being much larger than the film thickness leading to a decreased inelastic scattering signal intensity for the thinner films.

agreement between theory and experiment (ratio=k^{-1}) allows us to unambiguously separate the contributions of bulk and surface plasmons in silicon. We emphasize that this scaling effect of the EELS intensity with momentum can only be captured by k-EELS.

Finally, we explain the low energy branch in the visible range (1.5-4eV) that is observed in the data. Through analytical simulations and electron energy loss function theory, we confirm that this branch is the visible-region Cherenkov radiation in silicon. Cherenkov radiation (CR) is electromagnetic radiation generated when a charged moving particle passes through a medium with a velocity greater than the phase velocity of light in the medium. It has been studied in multitudes of dielectrics in energy loss experiments [37, 88, 20, 89, 90] as well as 2D materials [91], and metamaterials [92, 93]. Conventional CR in dielectrics will only be generated if the electron velocity is larger than the phase velocity in the medium ($v_z \geq c/\sqrt{\epsilon}$). The threshold electron velocity to observe Cherenkov radiation is thus defined as the phase velocity of light inside the medium ($v_{th} = c/\sqrt{\epsilon}$). The CR condition is satisfied in the visible region in silicon ($\epsilon_{Si} > 1.64$) (figure 3.1) for the relativistic electrons used in our experiment. The CR peak and band structure in the 200 nm, 100 nm and 60 nm silicon films between $\approx$ 2-4 eV (310-620 nm) in figure 3.2, respectively, is measured with k-EELS with an incident electron energy of 300 keV ($v_z = 0.78c$), well above the CR velocity threshold. Our results agree strongly with electron energy loss theory (red line in 3.2 (b), (c), (d)) as well as previous studies [37, 88, 94]. We emphasize the striking fact that our observation of visible Cherenkov radiation occurs in a 60 nm silicon thin film which is in the deep subwavelength nanophotonic regime. A detailed analysis of coherence properties of this visible Cherenkov radiation will be undertaken in a future study.

3.3 Pushing Cherenkov Radiation in Silicon from the Visible to the EUV

We now discuss how the plasmonic properties of silicon can be exploited to design EUV radiation sources by pushing the Cherenkov emission into the EUV regime. We propose to use the plasmonic properties of silicon to design a new class of high energy (EUV) hyperbolic metamaterials. Specifically, the multitude of applications possible with hyperbolic metamaterials can now be expanded into the EUV, specifically the generation of a tunable, broadband, and thresholdless Cherenkov radiation light source via electron excitation.

Interestingly, it has recently been shown that hyperbolic metamaterials (HMMs), a uniaxial metamaterial with a metallic response along one direction and a dielectric response along the orthogonal direction, can be used to eliminate the need for large

velocity electrons for generating Cherenkov radiation [95, 96, 97]. While on its own silicon can only support conventional Cherenkov radiation in the visible, its plasmonic properties in the DUV→EUV (section 3.2) can be used to realize structures with hyperbolic behaviour that generate thresholdless Cherenkov radiation in this untapped region of the spectrum.

The novel thresholdless CR phenomena possible in HMMs can be determined by first considering the CR cone angle (θ_c) in uniaxial media[6]:

$$tan(\theta_c) = \sqrt{\left(\frac{v_z}{c}\right)^2 \epsilon_z - \frac{\epsilon_z}{\epsilon_x}} \tag{3.1}$$

where θ_c is the angle between the Cherenkov wavevector (k_c) and the axis of the electron trajectory (figure 3.4 (a)), ϵ_x is the permittivity of the uniaxial structure in the planar direction and ϵ_z is the permittivity parallel to the c-axis.

In the case of a hyperbolic metamaterial, we impose the following conditions on our permittivity for the orthogonal directions of the metallic and dielectric response: $\epsilon_z < 0$, $\epsilon_x > 0$ (type I HMM) and $\epsilon_z > 0$, $\epsilon_x < 0$ (type II HMM). The CR velocity threshold with the imposed HMM permittivity conditions can be determined by requiring real values of θ_c in equation 3.1:

$$v_z \leq c/\sqrt{\epsilon_x} \quad \text{Type I} \tag{3.2}$$

$$0 \leq v_z \leq c \quad \text{Type II} \tag{3.3}$$

We see that in the case of a hyperbolic metamaterial for the type I case, the electron velocity now has an upper limit. This is the exact opposite of a conventional isotropic dielectric where a minimum velocity i.e. lower limit exists ($v_z \geq c/\sqrt{\epsilon}$). Furthermore, for the type II hyperbolic metamaterial any electron velocity will generate CR (details in appendix F). These are the cases of thresholdless Cherenkov radiation (TCR). Observe that if we consider a simple isotropic dielectric in equation

---

[6] The anistropic Cherenkov radiation dispersion in uniaxial media can be determined analytically from the uniaxial macroscopic electron energy loss function as defined in appendix A. Specifically, anistropic Cherenkov radiation is manifest in the volume loss contribution of the anistropic energy loss function, which has the form: $ELF_{volume} \propto \frac{(1-\epsilon_x(v_z/c)^2)}{(\epsilon_x \phi_z^2)} d$ where $\phi_z^2 = k_x^2 + (\epsilon_z/\epsilon_x)(\omega/v_z)^2 - \epsilon_z(\omega/c)^2$. In the limit where $\phi_z = 0$, we get a resonantly large enhancement to our anisotropic energy loss function which is the anistropic Cherenkov radiation in uniaxial media. We can determine the analytic uniaxial Cherenkov radiation dispersion by solving for the wavevector in the expression for ϕ_z^2 when $\phi_z = 0$:

$$k_x^c = \sqrt{\epsilon_z k_0^2 - \frac{\epsilon_z}{\epsilon_x}\left(\frac{\omega}{v_z}\right)^2} \quad \text{and} \quad k_z^c = \frac{\omega}{v_z}$$

where k_x^c is the component of the CR wavevector (k^c) parallel to the sample interface and k_z^c is the CR component along the c-axis fixed by the electron velocity (v_z). We define the anisotropic Cherenkov cone angle as seen in equation 3.1 and figure 3.4 (a) by realizing that $tan(\theta_c) = k_x^c/k_z^c$.

(a) $V_{electron} \ll c$

Si
SiO$_2$

k_x^c

θ_c

$k_z^c = \frac{\omega}{v_z}$

TCR Angle

Thresholdless Cherenkov Radiation (TCR) in the EUV

(b) ϵ_x ϵ_z

Type II

Type I

ϵ

Energy(eV)

(c) Resonance Cone Angle

θ_r

Resonance Condition:
$\theta_c = \theta_r$ as $v_z \to 0$

(d) **Anisotropic Dielectric Regime**

$v_z = 0.9$ c

$v_z = 0.5$ c

$v_z = 0.1$ c

$\frac{E_z}{\max(|\vec{E}|)}$

y (μm)

x (μm)

lower **cherenkov velocity threshold: $v_z \geq c/\epsilon_x$**

Type I HMM Regime

$v_z = 0.9$ c

$v_z = 0.5$ c

$v_z = 0.1$ c

$\frac{E_z}{\max(|\vec{E}|)}$

y (μm)

x (μm)

upper **cherenkov velocity threshold: $v_z \leq c/\epsilon_x$**

Decreasing $V_{electron}$

Figure 3.4: **Thresholdless Cherenkov Radiation (TCR) in the EUV** (a) Schematic of TCR ($v_z \ll c$) in the EUV excited in a hyperbolic metamaterial (HMM) composed of an 100 nm thick Si/SiO$_2$ multilayer stack in the effective medium limit. k^c is the TCR wavevector and θ_c is the TCR cone angle. (b) Uniaxial effective medium permittivity at 0.35 metallic fill fraction for the Si/SiO$_2$ multilayer stack highlighting the regions of type I and type II behaviour where TCR can be observed (c). Type II ($\epsilon_x < 0$, $\epsilon_z > 0$) HMM isofrequency typology that supports TCR. In the ideal limit, the strongest TCR resonance occurs as $v_z \to 0$ where θ_c lies along the asymptotes of the hyperbola in k-space (defined by angle θ_r) (details in appendix F). (d) Normalized E_z fields in the x-y plane plane of Cherenkov radiation in the dielectric and hyperbolic regimes of the Si/SiO$_2$ multilayer stack at different electron velocities in a lossless structure. Opposite trends are observed where the field strengths increase for the hyperbolic regime while they are suppressed in the dielectric regime as the electron velocity decreases. The type I regime is seen to support TCR in the EUV ($\approx$ 11-15.5 eV).

27
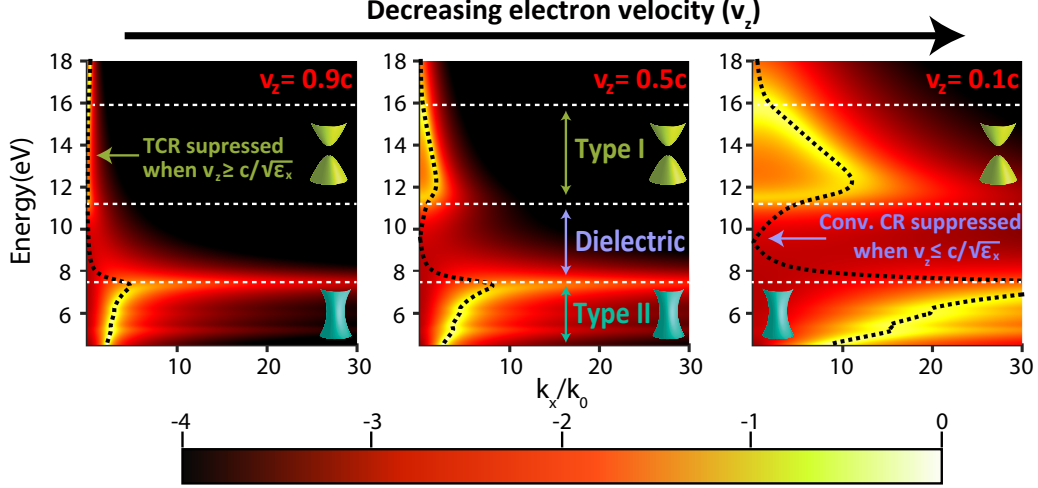
Figure 3.5: **TCR dispersion from the DUV to the EUV.** Simulation of the momentum-resolved electron scattering probability (details in appendix A) for the Si/SiO_2 structure described in figure 3.4 for different incident electron velocities. The simulations are performed in the effective medium (homogenized) low loss limit. The dashed black line shows the analytical Cherenkov radiation dispersion in a uniaxial metamaterial[6]. TCR is clearly observed in the type I and type II HMM regimes where the scattering probability increases with decreasing electron velocity. Note that the type I region has an upper threshold when $v_z \geq c/\sqrt{\epsilon_x}$ and is suppressed at $v_z = 0.9c$. The type II region has no velocity threshold. Additionally, the TCR dispersion extends to larger wavevectors as the velocity decreases as it is approaching the resonance condition described in figure 3.4 (b) where infinitely large wavevectors are supported in the structure and $v_{phase} = \omega/k \to 0$.

3.1 ($\epsilon_x = \epsilon_z \geq 0$) we retrieve the conventional CR limit ($v_z \geq c/\sqrt{\epsilon}$). Additionally note that the conditions for the type I and type II CR velocity thresholds would be flipped for an electron traveling along the x direction, as was seen in [95].

Via harnessing silicon's unique EUV plasmonic properties (section 3.2), novel EUV hyperbolic metamaterials can be designed using widely used materials in a simple geometry such as a Si/SiO_2 multilayer stack. Figure 3.4 (a) shows such a Si/SiO_2 multilayer structure whose permittivities in the effective medium limit (homogenized with Maxwell-Garnett theory) possess both type I and type II hyperbolic behaviour from the DUV to the EUV (figure 3.4 (b)). We envision that a practical realization of this structure would consist of approximately 16-20 alternating 8-10 nm layers of SiO_2 and crystalline Si. We strongly emphasize that our silicon based metamaterial design is unique and is unrelated to previous approaches exploiting doped semiconductors [78, 62] or alternate plasmonic media [76]. Also note, that doped semiconductors cannot have plasmonic responses at high frequencies beyond the infra-red region.

The hyperbolic regimes of the Si/SiO_2 multilayer stack give rise to the unique

TCR excitation. This is clearly seen in figure 3.4 (d) which shows the simulated Cherenkov radiation fields in the dielectric and hyperbolic regimes of the Si/SiO$_2$ multilayer at different electron velocities.[7] We observe in the type I regime that as the electron velocity decreases the relative Cherenkov radiation fields increase. This is the fundamental characteristic of TCR and is the exact opposite trend seen in the dielectric regime which supports conventional CR. Cherenkov radiation in the hyperbolic regime can be seen down to electron velocities as low as $v_z = 0.001c$ in the effective medium limit, however there is a fundamental trade-off between the velocity threshold reduction and the loss in the structure (details in appendix F).

Note that the type I regime supports TCR in the EUV ($\approx$ 11-15.5 eV) for the Si/SiO$_2$ structure. This allows for a potential EUV source from low energy electrons not possible with conventional CR. Additionally, the hyperbolic regions can be shifted in energy space by adjusting the silicon (metallic) fill fraction allowing for a TCR excitation that is highly tunable and considerably broadband. This is in contrast to other high energy CR sources that are narrowband, non-tunable and are subject to the conventional CR threshold [98, 99].

The origin of the TCR phenomena is due to the unique hyperbolic topology of the HMM isofrequency surface (figure 3.4 (c)). Note, the phase velocity in the medium approaches 0 at the asymptotes ($v_{phase} = \omega/k \to 0$). As explained previously, the threshold velocity of Cherenkov radiation can be connected to the phase velocity of light in the medium $v_{th} = v_{phase}$. In the limit of a vanishing electron velocity $v_z \to 0$, the Cherenkov wavevector can lie along the asymptotes of the hyperbola ($\theta_c = \theta_r$) where infinitely large wavevectors can be supported by the structure in the ideal limit (appendix F). Consequently the threshold velocity also vanishes ($v_{th} \to 0$) in hyperbolic media.

This point is further clarified in figure 3.5 which plots the momentum-resolved electron scattering probability for Cherenkov radiation in the Si/SiO$_2$ multilayer stack for different electron velocities (as calculated from the energy loss function [87]) . Our numerical simulation uses effective medium theory. We observe that as the velocity decreases, the scattering probability in the hyperbolic regions increases. There is an excellent agreement between the results of our numerical simulation and analytical theory of Cherenkov radiation denoted by the black dashed line. Additionally, this analytic TCR dispersion[6] highlights that the TCR extends to larger wavevectors as the electron velocity decreases (dashed black line). This is due to the fact that we are approaching closer to the resonance condition (figure 3.4 (c)) where infinitely large wavevectors are supported by the structure. We emphasize

---

[7]These calculations were performed by Sarang Pendharker. The electric fields are first computed in the k_x, k_y, ω domain. The fields in the space-time domain are computed by taking the inverse fourier transform. The FFT2 algorithm in the Numpy package in Python is used to compute the space-domain fields

that the fundamental limit to how low the velocity can reach in practice will be determined by absorption and the finite unit cell size (appendix F).

3.4 Conclusion

In conclusion, we experimentally demonstrate the generation of extreme ultra-violet plasmons supported by silicon with energies twice as large as those seen with aluminum via momentum-resolved electron energy loss spectroscopy. k-EELS is the ideal tool to observe such high energy excitations while simultaneously mapping the photonic band structure of plasmonic excitations to large wavevectors not possible with conventional EELS techniques. Our experimental observations are rigorously validated using macroscopic electrodynamic simulations of k-EELS and also first-principles density functional theory. Additionally, we proposed a simple Si/SiO_2 multilayer stack with a hyperbolic isofrequency response that can generate tunable and broadband thresholdless Cherenkov radiation in the EUV by harnessing silicon's unique EUV plasmonic properties. This can lead to applications in EUV waveguides/metamaterials/nano-antennas/hybrid-MEMS based on silicon, EUV light sources generated with low energy excitations, detectors for observation of non-relativistic particles, and the development of TCR free-electron lasers [97].

Chapter 4

Momentum-resolved Electron Energy Loss Spectroscopy in Natural Hyperbolic Media: Bismuth Telluride

In this chapter we use k-EELS to perform the first measurements of high-k modes and the hyperbolic Cherenkov radiation mode of Bi_2Te_3, a naturally occurring hyperbolic material. Recently, interest in the avenue of naturally occurring hyperbolic materials has gained traction as they have been seen to curtail the limitations of the finite size of the unit cell prevalent in artificial hyperbolic structures. Bi_2Te_3 is one of only 2 naturally occurring hyperbolic materials that have recently been shown to possess hyperbolic behaviour in the visible, and we confirm these properties here with k-EELS.

This chapter is the first attempt to demonstrate the ideas presented about high-k modes and hyperbolic Cherenkov radiation in the second half of chapter 3 with k-EELS. Specifically, naturally hyperbolic materials are the ideal hyperbolic structures to probe hyperbolic phenomena as they are not nearly as limited due to the constraints of fabrication and are the closest thing to a true hyperbolic effective medium. The hope is that experimental demonstrations in this chapter are a stepping stone to observe the more exotic properties of high-k modes and hyperbolic Cherenkov radiation in future studies in a wide array of material systems.

Note details about the nature of hyperbolic media can be seen in appendix E.

4.1   Introduction

Hyperbolic materials, uniaxial structures with a metallic response along one direction and dielectric response along the orthogonal direction, support unique electromagnetic modes with a wide variety of applications. They derive their name from their unique hyperbolic isofrequency typology that can support photonic excitations at large wave-vectors (high-k modes) that would normally decay in conventional media (details in appendix E). This has lead to a multitude of deep subwavelength applications in waveguiding, imaging, sensing, quantum and thermal engineering beyond conventional devices [58, 100, 56]. Additionally, there has been recent interest in the ability of hyperbolic materials to support thresholdless Cherenkov radiation [95, 96] (also discussed in chapter 3).

Recent interest in naturally occurring hyperbolic materials, composed of "individual layers" on the atomic scale, have been seen to curtail the limitations of the finite size of the unit cell prevalent in artificial hyperbolic structures. As the constituent components of naturally hyperbolic media are orders of magnitude smaller than the wavelength in the infrared to the UV, it can be treated as a true effective hyperbolic medium [101, 102, 62, 56]. Some examples of naturally hyperbolic materials include hBN in the infrared [103, 104] and graphite in the UV [105, 106]. Additionally, recent ellipsometry measurements have shown that the naturally occurring tetradymite Bi_2Te_3 possesses hyperbolic behaviour in the visible. The strong anisotropy is clearly evident in the uniaxial dielectric permittivity of Bi_2Te_3 parallel (ϵ_z) and perpendicular (ϵ_x) to the crystal axis shown in figure 4.1 (a) (note a parameter fit is used for ϵ_z, see figure caption). Bi_2Te_3 has a characteristic type II hyperbolic isofrequency response ($\epsilon_x < 0$, $\epsilon_z > 0$) (figure 4.1 (b)). Bi_2Te_3 and Bi_2Se_3 are the only known naturally occurring materials to exhibit hyperbolic behaviour in the visible [101, 107].

While the hyperbolic characteristics of Bi_2Te_3 have been determined [107], direct measurement of its high-k modes has yet to be performed. This is difficult to accomplish with optical techniques which use sources with small incident wavevectors that are unable to couple effectively to the high-k states. However, electron spectroscopy techniques are particularly useful for probing materials that support excitations at large-wavevectors (high-k modes) due to the inherently large momentum and evanescent field of the electron probe [22, 86].

In this chapter, we use momentum-resolved electron energy loss spectroscopy (k-EELS) to perform the first measurements of the high-k modes in Bi_2Te_3 and confirm its natural hyperbolic character from the visible to the UV. The k-EELS technique uses relativistic electrons with high energy and momentum that are able to couple to Bi_2Te_3's large momentum (high-k) states that are difficult to probe optically (figure 4.1 (c)). In addition, unlike more traditional spatially resolved
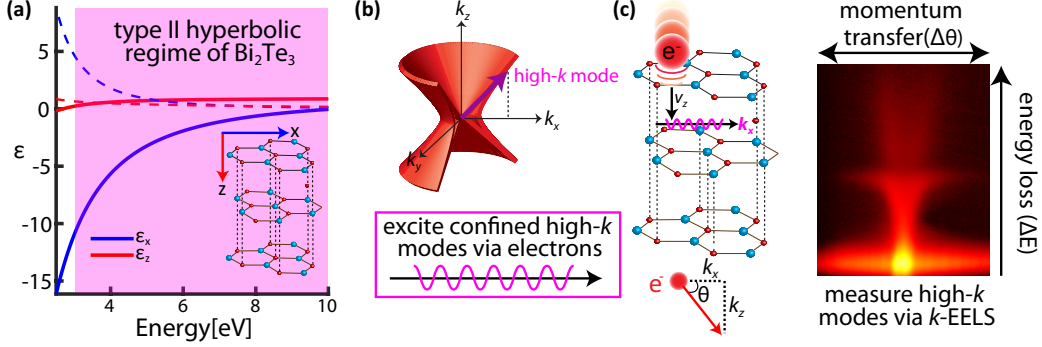
Figure 4.1: (a) Uniaxial dielectric permittivity of Bi_2Te_3 parallel (ϵ_z) and perpendicular (ϵ_x) to the c-axis showing type II hyperbolic behaviour ($\epsilon_x < 0$, $\epsilon_z > 0$) in the visible to the UV. Note the estimated plasma frequency of the ϵ_z component is blue shifted by 1.5 eV compared to [107] as a parameter fit to our experimental data. (b) The type II hyperbolic isofrequency surface of Bi_2Te_3 that can support photonic excitations with large momentum (high-k modes) that would normally decay in conventional media. (c) Schematic showing the excitation of high-k modes in Bi_2Te_3 via k-EELS. The subsequent energy loss (ΔE) and scattering angle (θ) of the electron as it passes through the sample is measured and corresponds directly to the energy and momentum (k) of the excited modes in the structure.

electron energy loss techniques, both the energy and the momentum dispersion of the high-k modes are measured. Alongside optical excitations, electron spectroscopy techniques can also probe photonic excitations generated by fast moving charges, such as Cherenkov radiation. Here, with k-EELS, we show the first measurement of hyperbolic Cherenkov radiation in a natural hyperbolic material (Bi_2Te_3) and discuss its unique thresholdless Cherenkov radiation properties (also discussed in chapter 3 for silicon metamaterials). We corroborate our experimental results using macroscopic electron energy loss theory. This work paves the way for realizing Bi_2Te_3 as a viable natural hyperbolic material from the visible to UV through its ability to support high-k modes and thresholdless Cherenkov radiation. Furthermore, we establish k-EELS as a fundamental tool to probe high-k excitations in any hyperbolic media.

4.2 Electron Scattering Probability of Bi_2Te_3 in the Hyperbolic Regime

Probing optical excitations in nanophotonic structures with electrons has been conducted with a variety of techniques such as cathodoluminescence, photoemission electron microscopy, and EELS [22]. In k-EELS, relativistic electrons normally incident on a sample will lose a characteristic amount of energy (ΔE) and be scattered
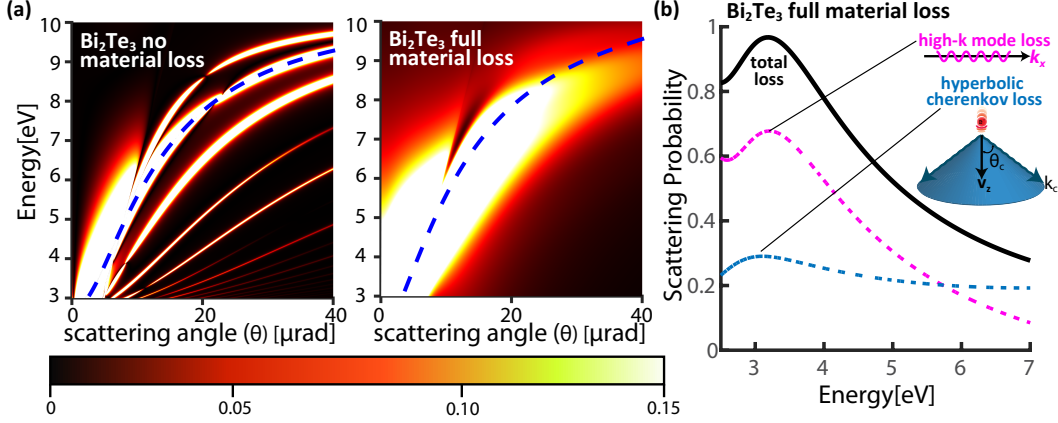
Figure 4.2: (a) The calculated total momentum-resolved electron energy loss probability (appendix A) in a 60 nm thick Bi_2Te_3 film with electrons impinging normal to the sample interface with a velocity $v_z = 0.78c$. In the case of Bi_2Te_3 with no material damping (left) a series of dispersive bands are calculated corresponding to the high-k modes of the structure. In the case with full material damping (right) dampening and broadening of the high-k modes is seen. The dashed blue line is the analytic dispersion of the hyperbolic CR mode (equation 4.1) excited in the sample alongside the high-k modes. (c) The theoretical electron energy loss probability integrated over the scattering angle (θ) showing the total loss as well as the individual contributions to the loss spectrum from high-k modes and hyperbolic CR.

at a particular scattering angle (θ) which corresponds directly to the energy and the momentum (k) of excitations supported by the sample (figure 4.1 (c)). The predicted energy loss and scattering angle of the electron in experiment can be calculated via the semi-classical electron energy loss probability [87, 20] (details in appendix A). Additionally, the energy loss probability has been shown to be closely related to the photonic density of states [22, 86].

Figure 4.2 (a) shows the simulated momentum-resolved electron energy loss probability for a 60 nm thick Bi_2Te_3 film with electrons normally incident on the structure with a velocity of $v_z = 0.78c$ with (right) and without (left) material damping. Note that figure 4.2 (a) is a representation of the photonic bandstructure of Bi_2Te_3 in the hyperbolic regime as $\theta \propto k$. For the case of no material damping, the dispersion profiles for a series of bands is apparent in the $3 - 9.5$ eV ($\approx 130 - 410$ nm) range which are the characteristic type II hyperbolic high-k modes of the structure. Unfortunately, Bi_2Te_3 is highly lossy in the hyperbolic regime [101] and, with regular material damping, the individual high-k mode dispersions become broadened and damped (figure 4.2 (a) (right)).

In addition to the high-k modes, the high velocity electron probe used in k-EELS can also excite Cherenkov radiation (CR) in Bi_2Te_3. CR is electromagnetic radiation

generated when a moving charged particle passes through a medium with a velocity greater than the phase velocity of light in the medium $v_{particle} \geq c/\sqrt{\epsilon}$. It has been studied in many electron energy loss experiments [37, 88, 20, 90]. CR in a uniaxial structure such as Bi_2Te_3 is emitted in the shape of a cone (figure 4.2 (inset)) with a Cherenkov cone angle (θ_c) described by the dispersion:

$$tan(\theta_c) = k_c^x/k_c^z = \sqrt{\left(\frac{v_z}{c}\right)^2 \epsilon_z - \frac{\epsilon_z}{\epsilon_x}} \tag{4.1}$$

where v_z is the electron velocity and k_c^x and k_c^z are components of the Cherenkov wavevector k_c [87] (additional details in chapter 3). The CR dispersion is plotted in figure 4.2 (a) as the dashed blue line and exists in the hyperbolic regime of Bi_2Te_3. Hyperbolic CR has recently gathered interest as it can be excited with no electron velocity threshold [95, 96, 97] (thresholdless Cherenkov radiation discussed in section 4.4 and in chapter 3).

The total loss probability of Bi_2Te_3 in the hyperbolic regime is thus predominately composed of contributions from high-k modes as well has the hyperbolic CR mode. This is seen in figure 4.2 (c) which plots the total relative electron scattering probability integrated over the scattering angle. The total loss (black line) alongside the isolated contributions from high-k modes and the hyperbolic CR mode are shown. The hyperbolic CR mode, which is a coherent effect across the bulk of the structure, has a relatively lower scattering probability in a thin 60 nm film.

4.3 Probing high-k Modes and Hyperbolic CR in Bi_2Te_3 with k-EELS

Figure 4.3 (a) shows the experimental k-EELS measurements over a range of different scattering angles (momentum) for a 60 nm Bi_2Te_3 film prepared via focused ion beam.[1] Electrons with an energy of 300 keV ($v_z = 0.78c$) are incident on the freestanding sample with the electron trajectory parallel to the c-axis of the hexagonal crystal structure.[2] Electron scattering angles up to 20 μrad ($\approx$ 2-3 times past the light line) were collected to probe both the high-k modes and the hyperbolic CR mode of Bi_2Te_3.

The experimental k-EELS measurements are plotted as a sum over a range of scattering angles with increasing magnitude as indicated by the 3 curves in figure 4.3 (a). The broad peak for all 3 angle sets corresponds to the high-k modes and hyperbolic CR excited in the sample. This is the first measurement of high-k modes

---

[1]Focused ion beam sample preparation was performed by Doug Vick. Details about the methodology are outlined in appendix I

[2]The details of k-EELS methodology are very similar to those outlined at the beginning of chapter 2
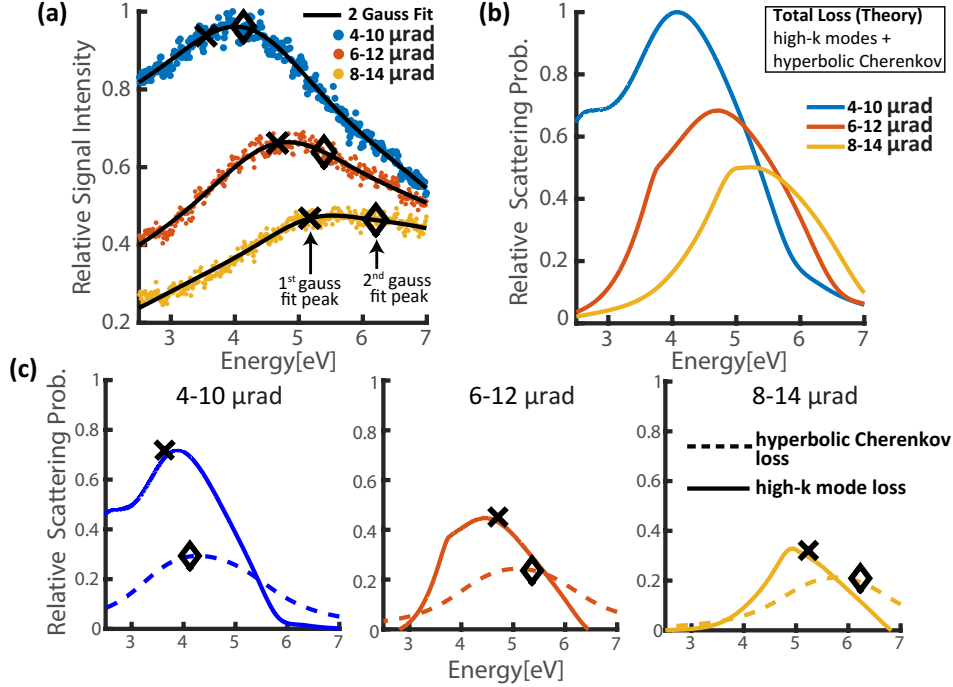
Figure 4.3: (a) Experimental k-EELS peaks of a 60 nm Bi$_2$Te$_3$ film summed over three sets of angular ranges for electrons normally incident on the sample with a velocity of $v_z = 0.78c$. The broad peak in each of the 3 sets consist of the high-k modes and the hyperbolic Cherenkov mode in Bi$_2$Te$_3$. A summation of two gaussian distributions is used to fit the data (cross and diamond mark peak positions) (b) Calculated relative electron scattering probability of the total loss in the structure corroborating the experimental data. (c) The calculated contributions to the total electron scattering probability from the high-k modes and the hyperbolic Cherenkov radiation mode. A strong correlation between the predicted high-k mode and hyperbolic Cherenkov radiation peaks is seen with the gaussian fit peak positions used to fit the experimental data (overlayed cross and diamond).

probed by k-EELS in any hyperbolic media and the first probe of hyperbolic CR in a natural hyperbolic media. To corroborate our experimental results, the theoretical relative electron scattering probability (equivalent to the relative signal intensity as measured in the experiment) for Bi$_2$Te$_3$ is plotted in figure 4.3 (b). A strong correlation between the peak positions and the scattering intensity magnitudes is seen between the theory and the experiment. The blue shifting of the energy loss peak with increasing scattering angle in figure 4.3(a) and (b) is a result of the dispersive nature of the high-k modes and hyperbolic CR mode (figure 4.2 (a)). Note that more conventional EELS techniques would not be able to capture the dispersive nature of such modes but can be captured here by k-EELS. Additionally, the scattering probability in both theory and experiment decreases with increasing scattering angle (as is well known from the inverse scaling of the two parameters as

36

described in chapter 2 and in figure 3.3 in chapter 3).

In figure 4.3 (a) a summation of two gaussian distributions are seen to accurately fit the experimental data (black line) for all 3 angle sets. The peak positions of the two separate gaussian distributions are shown as a cross and diamond and correspond to the high-k mode peak and the hyperbolic CR peak, respectively. This is validated in figure 4.3 (c) which breaks down the total Bi_2Te_3 loss probability (figure 4.3 (b)) into the separate contributions from the high-k modes and the hyperbolic CR mode. The gaussian fit peak positions extracted from experiment (overlayed on the plots) match well with the theoretical predictions for the two predominant peaks. To emphasize, this would be the first experimental measurement of the hyperbolic CR mode in natural hyperbolic media and the first measurement by k-EELS of hyperbolic high-k modes.

4.4   Thresholdless Cherenkov Radiation in Bi_2Te_3

Recently, it has been shown that hyperbolic materials eliminate the need for high velocity electrons in order to generate CR (normally $v_z \geq c/\sqrt{\epsilon}$ in conventional dielectrics). In fact, in the ideal limit, CR in a type II hyperbolic material can be generated for an electron traveling with any velocity ($0 \leq v_z \leq c$), known as thresholdless Cherenkov radiation (TCR) (details in appendix F). Note that hyperbolic CR (as measured in section 4.3) and TCR correspond to the same phenomena. Figure 4.4 (a) shows the generation of TCR in Bi_2Te_3 with a Cherenkov cone angle θ_c wavevector k_c. The foundation of the TCR phenomena is due to the unique typology of the hyperbolic isofrequency surface. We note that for the case of a type II hyperbolic material ($\epsilon_z > 0$, $\epsilon_x < 0$), if we take the limit $v_z \to 0$ in equation 4.1, θ_c projects k_c along the asymptotes of the type II hyperbola (figure 4.4 (c) inset) where infinitely large wavevectors are supported in the ideal limit. As such, the phase velocity in the medium also approaches 0 at this point ($v_{phase} = \omega/k \to 0$). The minimum electron velocity where the CR condition is satisfied is as at the point where $v_z = v_{phase}$ and consequently the minimum CR velocity threshold is also $v_{th} \to 0$ in hyperbolic media (these ideas are also presented in chapter 3).

The electron scattering probability for TCR (integrated over the scattering angle) at different incident electron velocities is plotted in figure 4.3 (b) for 60 nm Bi_2Te_3 (with regular damping) in the hyperbolic regime. The TCR scattering probability increases with decreasing electron velocity since k_c approaches closer to the resonance condition of lying along the asymptotes of the hyperbola. This is the exact opposite trend observed for conventional CR in dielectrics where the CR scattering probability becomes suppressed as v_z decreases. This resonance condition is also the basis for the fact that the TCR dispersion (equation 4.1) extends to larger scattering angles

37
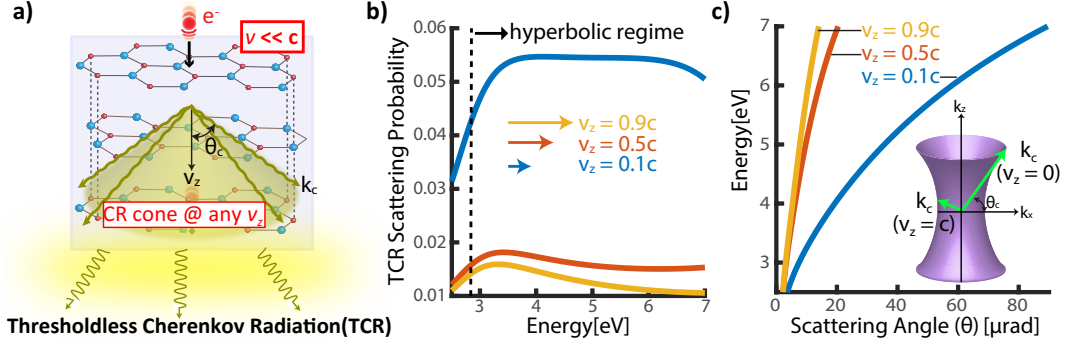
Figure 4.4: (a) Schematic showing the generation of thresholdless Cherenkov radiation (TCR) in Bi_2Te_3 in the hyperbolic regime with a Cherenkov cone angle θ_c and Cherenkov wavevector k_c. (b) Calculated electron scattering probability integrated over the scattering angle for TCR in a 60 nm Bi_2Te_3 film (with regular material damping) for normally incident electrons with different velocities. (c) Analytic TCR dispersion profiles (equation 4.1) for a 60 nm Bi_2Te_3 film at different electron velocities. The TCR dispersion extends to larger scattering angles (higher k) for the slower electrons due to the unique hyperbolic dispersion (inset).

(or wavevector, k_c) as the electron velocity is decreased (figure 4.4 (c)).

Natural hyperbolic media are far more effective at generating TCR than artificial HMMs which are limited by the finite size of their unit cell (d) and can only support wavevector magnitudes reaching the edge of the brillioun zone ($k \approx \pi/d$). This fundamentally limits their ability to reduce the phase velocity (and thus the TCR threshold). However, as natural hyperbolic materials have a unit cell size on the atomic scale, very large magnitudes of k can be supported in the structure to achieve TCR with much smaller threshold velocities.

4.5   Conclusion

In conclusion, we have performed the first measurement of hyperbolic CR and high-k modes in Bi_2Te_3 using k-EELS. Furthermore, we theoretically show that the hyperbolic CR mode has no electron velocity threshold. This work paves the way for realizing Bi_2Te_3 as viable natural hyperbolic material in the visible/low-UV and establishes k-EELS as fundamental tool to probe hyperbolic materials across large regions of the spectrum.

Chapter 5

Conclusions

In this chapter we briefly summarize the results of the previous chapters as well as provide broad impacts of the results for the field of nanophotonics.

5.1 Summary

5.1.1 Chapter 2: Momentum-resolved Electron Energy Loss Spectroscopy for Mapping the Photonic Density of States

In this chapter, momentum-resolved electron energy loss spectroscopy (k-EELS) was used as an approach to experimentally measure the momentum-resolved photonic density of states (k-PDOS) dispersion of plasmonic systems up to large wavevectors not possible with optical techniques. Some of the key points chapter include the following:

- Scanning transmission electron microscopy EELS (STEM-EELS) has recently received attention for its ability to spatially probe classical and quantum excitations outside the light cone at sub-nanometer resolution. We show in contrast to STEM-EELS, widely utilized in plasmonics, k-EELS provides information on not only the energy loss but also the momentum characteristics of plasmonic excitations accurately up to high-k

- Although connections between k-EELS and the k-PDOS have been made in the past for infinite structures with no translational invariance, here we provide insight into the fundamental differences between k-EELS and the k-PDOS for realistic finite structures of great interest to current research in both energy and momentum space

- We measure the k-PDOS dispersion and explore the role of electron energy and momentum loss for a plasmonic thin film as a function of thickness up

to wavevectors 5 times past the light line showing a strong correspondence between theory and experiment.

Broad Impact

Optical techniques are severely limited in their ability to measure the photonic density of states at large wavevectors in photonic nanostructures. STEM-EELS circumvents this limitation using the inherently evanescent field of the electron to couple to high-k excitations providing a direct measure of the PDOS. Despite this, STEM-EELS provides no information about the momentum-resolved PDOS that is possible with k-EELS. Our work emphasizes k-EELS as a valuable tool for the k-space mapping of the PDOS for plasmonic systems up to large wavevectors which can give key insights into classical, quantum and non-local optical phenomena (such as hyperbolic polaritons, slow light modes and strong coupling) from the measured band structure. Furthermore, it can help shed more light on questions and controversies related to the nature of non-local vs. quantum plasmonic excitations in photonic nanostructures. The popularity of the STEM-EELS approach highlights the pressing need for advancing the current state of characterization tools in the field of nanophotonics. k-EELS addresses this need and will only expand on this interest while providing even greater insight.

5.1.2 Chapter 3: Extreme Ultra-violet Plasmonics and Cherenkov Radiation in Silicon

In this chapter, we experimentally demonstrate that silicon can support plasmonic excitations at high energies in the EUV which is beyond any other material used in the field of nanophotonics. We use relativistic electrons to experimentally probe the optical properties of silicon using k-EELS. We also propose a feasible EUV radiation source using this high energy plasmonic effect in silicon plasmonic metamaterials. We hope that this chapter acts as a stepping stone for the field EUV plasmonics and devices. Some of the key points of the chapter include the following:

- Similar to chapter 2 we highlight that k-EELS provides information on not only the energy loss but also the momentum characteristics of plasmonic excitations not possible with STEM-EELS

- Specifically, we use k-EELS to probe the unique plasmonic properties of silicon in the EUV with a surface plasmon resonance twice as large as seen in aluminum (the material of choice for high energy plasmonic systems). This can lay the foundation for on-chip EUV silicon photonics as well as EUV photonic MEMS.

- We corroborate our experimental findings with a strong match to macroscopic electrodynamic electron energy loss theory as well as quantum density functional theory calculations. There is a strong agreement between theory and experiment.

- We also propose a tunable, broadband EUV radiation source based on thresholdless Cherenkov radiation made possible by exploiting the EUV plasmonic properties of silicon. A compact EUV source is an open problem for the field of photonics and we hope our design will act as stepping stone for future work in this field.

Broad Impact

Silicon is the key material of choice in nano-electronics, on-chip photonics, solar cells and MEMS. Interestingly, in this chapter, we show that silicon can support surface and bulk plasmons in the EUV regime not possible with conventional plasmonic materials. This work can pave the way for applications such as EUV waveguides, metamaterials, and devices with potential applications in biotechnology, EUV lensing for imaging and lithography, and integrated EUV sources.
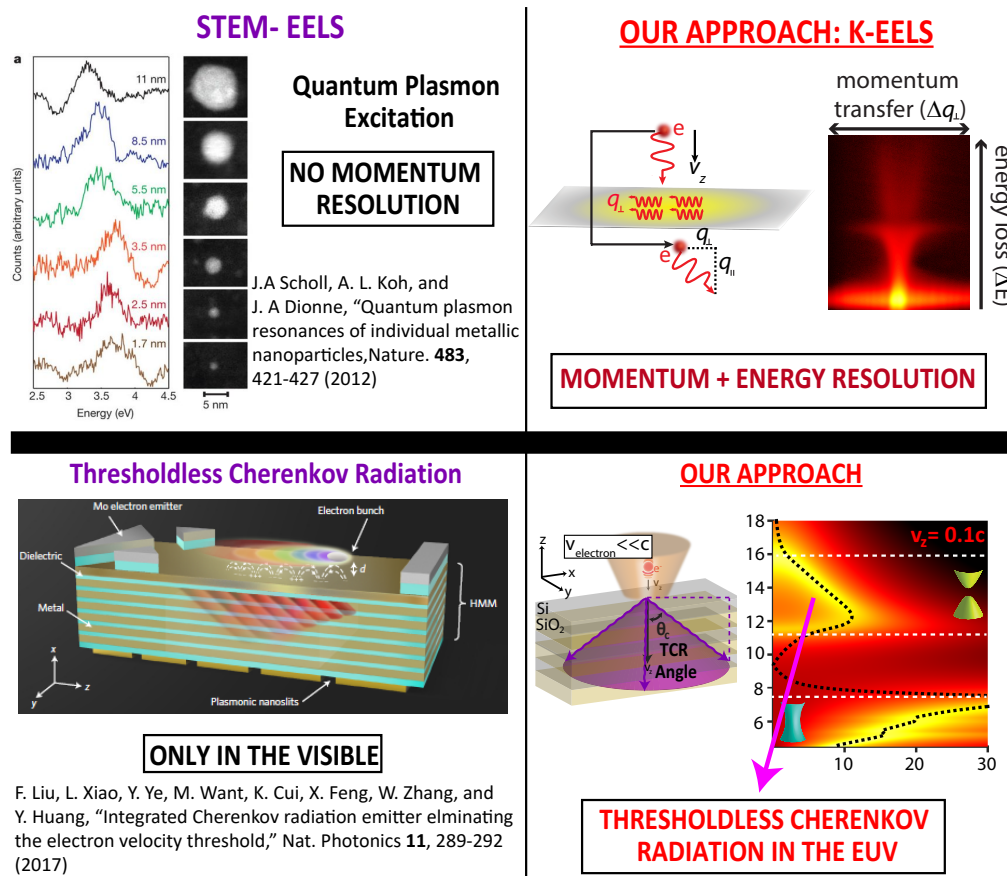
Figure 5.1: Broad impact of the contributions in this thesis.

5.1.3 Chapter 4: Momentum-resolved Electron Energy Loss Spectroscopy in Natural Hyperbolic Media: Bismuth Telluride

In this chapter we use k-EELS to perform the first measurements of high-k modes and the hyperbolic Cherenkov radiation mode of Bi_2Te_3, a naturally occurring hyperbolic material. Bi_2Te_3 is one of only 2 naturally occurring hyperbolic materials that have recently been shown to possess hyperbolic behaviour in the visible, and we confirm these properties in this chapter with k-EELS. This chapter is the first attempt to demonstrate the ideas presented about high-k modes and hyperbolic Cherenkov radiation in the second half of chapter 3 with k-EELS. Some of the key points of the chapter include the following:

- Hyperbolic materials are able to support photonic excitations up to large wavevectors (high-k modes) that are difficult to probe optically but much more feasible with a technique like k-EELS. As a result, in this chapter, we perform the first measurement of the high-k modes and the hyperbolic Cherenkov radiation mode in Bi_2Te_3 using the technique.

- We perform detailed simulations with electron energy loss theory on the nature of the hyperbolic Cherenkov radiation mode in Bi_2Te_3 and discuss its thresholdless Cherenkov radiation properties. We highlight that thresholdless cherenkov radiation is most feasibly achieved in natural hyperbolic materials as they can be treated as a true hyperbolic effective medium that has the ability to truly reduce the Cherenkov threshold velocity to minute quantities.

- The experimental demonstrations in this chapter are a stepping stone to observe the more exotic properties of high-k modes and hyperbolic Cherenkov radiation (amongst other unique metamaterial modes) in future studies in a wide array of material systems.

Broad Impact

Hyperbolic metamaterials have the potential for a wide array of deep subwavelength applications such as waveguiding, imaging, sensing, quantum and thermal engineering beyond conventional devices. Recently, interest in the avenue of naturally occurring hyperbolic materials has gained traction as they have been seen to curtail the limitations of the finite size of the unit cell prevalent in artificial hyperbolic structures. Specifically, naturally hyperbolic materials are the ideal hyperbolic structures to probe hyperbolic phenomena as they are not nearly as limited due to the constraints of fabrication and are the closest thing to a true hyperbolic effective medium. As all hyperbolic phenomena of interest are deeply subwavelength (high-k), k-EELS is the ideal platform to probe such media due to the large momentum of

the relativistic electrons that are able to couple to the high-k excitations. The versatility of the approach also allows it to probe hyperbolic media across large regions of the spectrum from the low visible to the EUV.

Bibliography

[1] Xiang Zhang and Zhaowei Liu. Superlenses to overcome the diffraction limit. *Nature Materials*, 7(6):435–441, June 2008.

[2] Zubin Jacob, Leonid V. Alekseyev, and Evgenii Narimanov. Optical Hyperlens: Far-field imaging beyond the diffraction limit. *Optics Express*, 14(18):8247–8256, September 2006.

[3] Zhaowei Liu, Hyesog Lee, Yi Xiong, Cheng Sun, and Xiang Zhang. Far-Field Optical Hyperlens Magnifying Sub-Diffraction-Limited Objects. *Science*, 315(5819):1686–1686, March 2007.

[4] Deep Punj, Mathieu Mivelle, Satish Babu Moparthi, Thomas S. van Zanten, Herv Rigneault, Niek F. van Hulst, Mara F. Garca-Paraj, and Jrme Wenger. A plasmonic antenna-in-box platform for enhanced single-molecule analysis at micromolar concentrations. *Nature Nanotechnology*, 8(7):512–516, July 2013.

[5] R. Zhang, Y. Zhang, Z. C. Dong, S. Jiang, C. Zhang, L. G. Chen, L. Zhang, Y. Liao, J. Aizpurua, Y. Luo, J. L. Yang, and J. G. Hou. Chemical mapping of a single molecule by plasmon-enhanced Raman scattering. *Nature*, 498(7452):82–86, June 2013.

[6] A. Femius Koenderink, Andrea Al, and Albert Polman. Nanophotonics: Shrinking light-based technology. *Science*, 348(6234):516–521, May 2015.

[7] M. D. Eisaman, J. Fan, A. Migdall, and S. V. Polyakov. Invited Review Article: Single-photon sources and detectors. *Review of Scientific Instruments*, 82(7):071101, July 2011.

[8] William L. Barnes, Alain Dereux, and Thomas W. Ebbesen. Surface plasmon subwavelength optics, August 2003.

[9] A. Yu. Nikitin, F. Guinea, F. J. Garca-Vidal, and L. Martn-Moreno. Edge and waveguide terahertz surface plasmon modes in graphene microribbons. *Physical Review B*, 84(16):161407, October 2011.

[10] Pierre Berini and Israel De Leon. Surface plasmonpolariton amplifiers and lasers. *Nature Photonics*, 6(1):16–24, January 2012.

[11] S. Nie, D. T. Chiu, and R. N. Zare. Probing individual molecules with confocal fluorescence microscopy. *Science*, 266(5187):1018–1021, November 1994.

[12] Lothar Schermelleh, Rainer Heintzmann, and Heinrich Leonhardt. A guide to super-resolution fluorescence microscopy. *The Journal of Cell Biology*, 190(2):165–175, July 2010.

[13] S. H. Lin. *Multiphoton Spectroscopy of Molecules*. Elsevier, December 2012.

[14] Michael J. Rust, Mark Bates, and Xiaowei Zhuang. Sub-diffraction-limit imaging by stochastic optical reconstruction microscopy (STORM). *Nature Methods*, 3(10):793–796, October 2006.

[15] Bo Huang, Wenqin Wang, Mark Bates, and Xiaowei Zhuang. Three-Dimensional Super-Resolution Imaging by Stochastic Optical Reconstruction Microscopy. *Science*, 319(5864):810–813, February 2008.

[16] Eric Betzig and Robert J. Chichester. Single Molecules Observed by Near-Field Scanning Optical Microscopy. *Science*, 262(5138):1422–1425, November 1993.

[17] Satoshi Kawata, Yasushi Inouye, and Prabhat Verma. Plasmonics for near-field nano-imaging and superlensing. *Nature Photonics*, 3(7):388–394, July 2009.

[18] R. H. Ritchie. Plasma Losses by Fast Electrons in Thin Films. *Physical Review*, 106(5):874–881, June 1957.

[19] E. Kretschmann and H. Raether. Notizen: Radiative Decay of Non Radiative Surface Plasmons Excited by Light. *Zeitschrift fr Naturforschung A*, 23(12):2135–2136, 2014.

[20] R.F. Egerton. *Electron Energy-Loss Spectroscopy in the Electron Microscope*. Springer US, 2011.

[21] James Hillier and R. F. Baker. Microanalysis by Means of Electrons. *Journal of Applied Physics*, 15(9):663–675, September 1944.

[22] F. J. Garcia de Abajo. Optical excitations in electron microscopy. *Reviews of Modern Physics*, 82(1):209–275, February 2010.

[23] Viktor Myroshnychenko, Jaysen Nelayah, Giorgio Adamo, Nicolas Geuquet, Jessica Rodrguez-Fernndez, Isabel Pastoriza-Santos, Kevin F. MacDonald, Luc Henrard, Luis M. Liz-Marzn, Nikolay I. Zheludev, Mathieu Kociak, and F. Javier Garca de Abajo. Plasmon Spectroscopy and Imaging of Individual Gold Nanodecahedra: A Combined Optical Microscopy, Cathodoluminescence, and Electron Energy-Loss Spectroscopy Study. *Nano Letters*, 12(8):4172–4180, August 2012.

[24] Michel Bosman, Vicki J. Keast, Masashi Watanabe, Abbas I. Maaroof, and Michael B. Cortie. Mapping surface plasmons at the nanometre scale with an electron beam. *Nanotechnology*, 18(16):165505, 2007.

[25] Jaysen Nelayah, Mathieu Kociak, Odile Stphan, F. Javier Garca de Abajo, Marcel Tenc, Luc Henrard, Dario Taverna, Isabel Pastoriza-Santos, Luis M. Liz-Marzn, and Christian Colliex. Mapping surface plasmons on a single metallic nanoparticle. *Nature Physics*, 3(5):348–353, May 2007.

[26] Christian Colliex, Mathieu Kociak, and Odile Stphan. Electron Energy Loss Spectroscopy imaging of surface plasmons at the nanometer scale. *Ultramicroscopy*, 162:A1–A24, March 2016.

[27] Richard G. Hobbs, Vitor R. Manfrinato, Yujia Yang, Sarah A. Goodman, Lihua Zhang, Eric A. Stach, and Karl K. Berggren. High-Energy Surface and Volume Plasmons in Nanopatterned Sub-10 nm Aluminum Nanostructures. *Nano Letters*, 16(7):4149–4157, July 2016.

[28] Sren Raza, Shima Kadkhodazadeh, Thomas Christensen, Marcel Di Vece, Martijn Wubs, N. Asger Mortensen, and Nicolas Stenger. Multipole plasmons and their disappearance in few-nanometre silver nanoparticles. *Nature Communications*, 6:8788, November 2015.

[29] F. Ouyang, P. E. Batson, and M. Isaacson. Quantum size effects in the surface-plasmon excitation of small metallic particles by electron-energy-loss spectroscopy. *Physical Review B*, 46(23):15421–15425, December 1992.

[30] Jonathan A. Scholl, Aitzol Garca-Etxarri, Ai Leen Koh, and Jennifer A. Dionne. Observation of Quantum Tunneling between Two Plasmonic Nanoparticles. *Nano Letters*, 13(2):564–569, February 2013.

[31] Wu Zhou, Jaekwang Lee, Jagjit Nanda, Sokrates T. Pantelides, Stephen J. Pennycook, and Juan-Carlos Idrobo. Atomically localized plasmon enhancement in monolayer graphene. *Nature Nanotechnology*, 7(3):161–165, March 2012.

[32] Shu Fen Tan, Lin Wu, Joel K. W. Yang, Ping Bai, Michel Bosman, and Christian A. Nijhuis. Quantum Plasmon Resonances Controlled by Molecular Tunnel Junctions. *Science*, 343(6178):1496–1499, March 2014.

[33] Gabriel D. Bernasconi, Jrmy Butet, Valentin Flauraud, Duncan Alexander, Juergen Brugger, and Olivier J. F. Martin. Where Does Energy Go in Electron Energy Loss Spectroscopy of Nanostructures? *ACS Photonics*, 4(1):156–164, January 2017.

[34] F. J. Garcia de Abajo and M. Kociak. Probing the Photonic Local Density of States with Electron Energy Loss Spectroscopy. *Physical Review Letters*, 100(10):106804, March 2008.

[35] Rong-Chun Ge and Stephen Hughes. Quasinormal mode theory and modelling of electron energy loss spectroscopy for plasmonic nanostructures. *Journal of Optics*, 18(5):054002, 2016.

[36] R. B. Pettit, J. Silcox, and R. Vincent. Measurement of surface-plasmon dispersion in oxidized aluminum films. *Physical Review B*, 11(8):3116–3123, April 1975.

[37] C. H. Chen, J. Silcox, and R. Vincent. Electron-energy losses in silicon: Bulk and surface plasmons and Cerenkov radiation. *Physical Review B*, 12(1):64–71, July 1975.

[38] P. E. Batson and J. Silcox. Experimental energy-loss function, Im[-1(q,)], for aluminum. *Physical Review B*, 27(9):5224–5239, May 1983.

[39] Sren Raza, Nicolas Stenger, Shima Kadkhodazadeh, Sren V. Fischer, Natalie Kostesha, Antti-Pekka Jauho, Andrew Burrows, Martijn Wubs, and N. Asger Mortensen. Blueshift of the surface plasmon resonance in silver nanoparticles studied with EELS. *Nanophotonics*, 2(2):131–138, 2013.

[40] Aeneas Wiener, Huigao Duan, Michel Bosman, Andrew P. Horsfield, John B. Pendry, Joel K. W. Yang, Stefan A. Maier, and Antonio I. Fernndez-Domnguez. Electron-Energy Loss Study of Nonlocal Effects in Connected Plasmonic Nanoprisms. *ACS Nano*, 7(7):6287–6296, July 2013.

[41] Thomas Christensen, Wei Yan, Sren Raza, Antti-Pekka Jauho, N. Asger Mortensen, and Martijn Wubs. Nonlocal Response of Metallic Nanospheres Probed by Light, Electrons, and Atoms. *ACS Nano*, 8(2):1745–1758, February 2014.

[42] Amir H. Atabaki, Sajjad Moazeni, Fabio Pavanello, Hayk Gevorgyan, Jelena Notaros, Luca Alloatti, Mark T. Wade, Chen Sun, Seth A. Kruger, Huaiyu Meng, Kenaish Al Qubaisi, Imbert Wang, Bohan Zhang, Anatol Khilo, Christopher V. Baiocco, Milo A. Popovi, Vladimir M. Stojanovi, and Rajeev J. Ram. Integrating photonics with silicon nanoelectronics for the next generation of systems on a chip. *Nature*, 556(7701):349–354, April 2018.

[43] Ehsan Arbabi, Amir Arbabi, Seyedeh Mahsa Kamali, Yu Horie, Mohammad-Sadegh Faraji-Dana, and Andrei Faraon. MEMS-tunable dielectric metasurface lens. *Nature Communications*, 9(1):812, February 2018.

[44] Francesco Priolo, Tom Gregorkiewicz, Matteo Galli, and Thomas F. Krauss. Silicon nanostructures for photonics and photovoltaics. *Nature Nanotechnology*, 9(1):19–32, January 2014.

[45] Saman Jahani, Sangsik Kim, Jonathan Atkinson, Justin C. Wirth, Farid Kalhor, Abdullah Al Noman, Ward D. Newman, Prashant Shekhar, Kyunghun Han, Vien Van, Raymond G. DeCorby, Lukas Chrostowski, Minghao Qi, and Zubin Jacob. Controlling evanescent waves using silicon photonic all-dielectric metamaterials for dense integration. *Nature Communications*, 9(1):1893, May 2018.

[46] Saman Jahani and Zubin Jacob. All-dielectric metamaterials. *Nature Nanotechnology*, 11(1):23–36, January 2016.

[47] Isabelle Staude and Jrg Schilling. Metamaterial-inspired silicon nanophotonics. *Nature Photonics*, 11(5):274–284, May 2017.

[48] Dennis F. Gardner, Michael Tanksalvala, Elisabeth R. Shanblatt, Xiaoshi Zhang, Benjamin R. Galloway, Christina L. Porter, Robert Karl Jr, Charles Bevis, Daniel E. Adams, Henry C. Kapteyn, Margaret M. Murnane, and Giulia F. Mancini. Subwavelength coherent imaging of periodic samples using a 13.5 nm tabletop high-harmonic light source. *Nature Photonics*, 11(4):259–263, April 2017.

[49] Zhensheng Tao, Cong Chen, Tibor Szilvsi, Mark Keller, Manos Mavrikakis, Henry Kapteyn, and Margaret Murnane. Direct time-domain observation of attosecond final-state lifetimes in photoemission from solids. *Science*, 353(6294):62–67, July 2016.

[50] Jianwei Miao, Tetsuya Ishikawa, Ian K. Robinson, and Margaret M. Murnane. Beyond crystallography: Diffractive imaging using coherent x-ray light sources. *Science*, 348(6234):530–535, May 2015.

[51] Bjorn A. M. Hansson, Alexander N. Bykanov, Igor V. Fomenkov, and David C. Brandt. Laser produced plasma EUV light source, July 2017.

[52] Daniel T. Elg, John R. Sporre, Gianluca A. Panici, Shailendra N. Srivastava, and David N. Ruzic. In situ collector cleaning and extreme ultraviolet reflectivity restoration by hydrogen plasma for extreme ultraviolet sources. *Journal of Vacuum Science & Technology A*, 34(2):021305, February 2016.

[53] David C. Brandt, Igor V. Fomenkov, Nigel R. Farrar, Bruno La Fontaine, David W. Myers, Daniel J. Brown, Alex I. Ershov, Norbert R. Bwering, Daniel J. Riggs, Robert J. Rafac, Silvia De Dea, Rudy Peeters, Hans Meiling, Noreen Harned, Daniel Smith, Alberto Pirati, and Robert Kazinczi. LPP EUV source readiness for NXE 3300b. In *Extreme Ultraviolet (EUV) Lithography V*, volume 9048, page 90480C. International Society for Optics and Photonics, March 2014.

[54] M. Kuttge, E. J. R. Vesseur, A. F. Koenderink, H. J. Lezec, H. A. Atwater, F. J. Garca de Abajo, and A. Polman. Local density of states, spectrum, and far-field interference of surface plasmon polaritons probed by cathodoluminescence. *Physical Review B*, 79(11):113405, March 2009.

[55] Jonathan A. Scholl, Ai Leen Koh, and Jennifer A. Dionne. Quantum plasmon resonances of individual metallic nanoparticles. *Nature*, 483(7390):421–427, March 2012.

[56] Prashant Shekhar, Jonathan Atkinson, and Zubin Jacob. Hyperbolic metamaterials: fundamentals and applications. *Nano Convergence*, 1(1):1–17, December 2014.

[57] C. L. Cortes, W. Newman, S. Molesky, and Z. Jacob. Quantum nanophotonics using hyperbolic metamaterials. *arXiv:1204.5529*, April 2012.

[58] Alexander Poddubny, Ivan Iorsh, Pavel Belov, and Yuri Kivshar. Hyperbolic metamaterials. *Nature Photonics*, 7(12):948–957, December 2013.

[59] Cristian L. Cortes and Zubin Jacob. Photonic analog of a van Hove singularity in metamaterials. *Physical Review B*, 88(4):045407, July 2013.

[60] Toshihiko Baba. Slow light in photonic crystals. *Nature Photonics*, 2(8):465–473, August 2008.

[61] Jonathan Plumridge, Edmund Clarke, Ray Murray, and Chris Phillips. Ultrastrong coupling effects with quantum metamaterials. *Solid State Communications*, 146(910):406–408, June 2008.

[62] Prashant Shekhar and Zubin Jacob. Strong coupling in hyperbolic metamaterials. *Physical Review B*, 90(4):045313, July 2014.

[63] Sren Raza, Thomas Christensen, Martijn Wubs, Sergey I. Bozhevolnyi, and N. Asger Mortensen. Nonlocal response in thin-film waveguides: Loss versus nonlocality and breaking of complementarity. *Physical Review B*, 88(11):115401, September 2013.

[64] Wei Yan and N. Asger Mortensen. Nonclassical effects in plasmonics: An energy perspective to quantify nonclassical effects. *Physical Review B*, 93(11):115439, March 2016.

[65] M. Bergen, M. Malac, R.a. McLeod, D. Hoyle, Y. Taniguchi, T. Yaguchi, J. Chen, and T. Yotsuji. Centralized Instrument Control for a TEM Laboratory. *Microscopy and Microanalysis*, 19(Supplement S2):1394–1395, August 2013.

[66] Weiqiang Chen, Mark D. Thoreson, Satoshi Ishii, Alexander V. Kildishev, and Vladimir M. Shalaev. Ultra-thin ultra-smooth and low-loss silver films on a germanium wetting layer. *Optics Express*, 18(5):5124–5134, March 2010.

[67] P. N. Dyachenko, S. Molesky, A. Yu Petrov, M. Strmer, T. Krekeler, S. Lang, M. Ritter, Z. Jacob, and M. Eich. Controlling thermal emission with refractory epsilon-near-zero metamaterials via topological transitions. *Nature Communications*, 7:11809, June 2016.

[68] G.W. Ford and W.H. Weber. Electromagnetic interactions of molecules with metal surfaces. *Physics Reports*, 113(4):195–287, November 1984.

[69] J. P. R. Bolton and M. Chen. Electron energy loss in multilayered slabs. I. Normal incidence. *Journal of Physics: Condensed Matter*, 7(18):3373, 1995.

[70] J. B. Chase and K. L. Kliewer. Electron Energy Loss Due to Surface Modes in a Thin Ionic Crystal Film. *Physical Review B*, 2(11):4389–4400, December 1970.

[71] Andrea Al, Mrio G. Silveirinha, Alessandro Salandrino, and Nader Engheta. Epsilon-near-zero metamaterials and electromagnetic sources: Tailoring the radiation phase pattern. *Physical Review B*, 75(15):155410, April 2007.

[72] Ruben Maas, James Parsons, Nader Engheta, and Albert Polman. Experimental realization of an epsilon-near-zero metamaterial at visible wavelengths. *Nature Photonics*, 7(11):907–912, November 2013.

[73] Aycan Yurtsever, Martin Couillard, and David A. Muller. Formation of Guided Cherenkov Radiation in Silicon-Based Nanocomposites. *Physical Review Letters*, 100(21):217402, May 2008.

[74] Edward D. Palik. *Handbook of Optical Constants of Solids*. Academic Press, 1998.

[75] H. R. Philipp and H. Ehrenreich. Optical Properties of Semiconductors. *Physical Review*, 129(4):1550–1560, February 1963.

[76] P.r. West, S. Ishii, G.v. Naik, N.k. Emani, V.m. Shalaev, and A. Boltasseva. Searching for better plasmonic materials. *Laser & Photonics Reviews*, 4(6):795–808, 2010.

[77] Long Ju, Baisong Geng, Jason Horng, Caglar Girit, Michael Martin, Zhao Hao, Hans A. Bechtel, Xiaogan Liang, Alex Zettl, Y. Ron Shen, and Feng Wang. Graphene plasmonics for tunable terahertz metamaterials. *Nature Nanotechnology*, 6(10):630–634, October 2011.

[78] Anthony J. Hoffman, Leonid Alekseyev, Scott S. Howard, Kale J. Franz, Dan Wasserman, Viktor A. Podolskiy, Evgenii E. Narimanov, Deborah L. Sivco, and Claire Gmachl. Negative refraction in semiconductor metamaterials. *Nature Materials*, 6(12):946–950, December 2007.

[79] Dmitri K. Gramotnev and Sergey I. Bozhevolnyi. Plasmonics beyond the diffraction limit. *Nature Photonics*, 4(2):83–91, February 2010.

[80] Ignacy Gryczynski, Joanna Malicka, Zygmunt Gryczynski, Kazimierz Nowaczyk, and Joseph R. Lakowicz. Ultraviolet Surface Plasmon-Coupled Emission Using Thin Aluminum Films. *Analytical Chemistry*, 76(14):4076–4081, July 2004.

[81] Mark W. Knight, Lifei Liu, Yumin Wang, Lisa Brown, Shaunak Mukherjee, Nicholas S. King, Henry O. Everitt, Peter Nordlander, and Naomi J. Halas. Aluminum Plasmonic Nanoantennas. *Nano Letters*, 12(11):6000–6004, November 2012.

[82] Atsushi Ono, Masakazu Kikawada, Rentaro Akimoto, Wataru Inami, and Yoshimasa Kawata. Fluorescence enhancement with deep-ultraviolet surface plasmon excitation. *Optics Express*, 21(15):17447–17453, July 2013.

[83] Zhaowei Liu, Jennifer M. Steele, Werayut Srituravanich, Yuri Pikus, Cheng Sun, and Xiang Zhang. Focusing Surface Plasmons with a Plasmonic Lens. *Nano Letters*, 5(9):1726–1729, September 2005.

[84] G. Kresse and J. Furthmller. Efficient iterative schemes for ab initio total-energy calculations using a plane-wave basis set. *Physical Review B*, 54(16):11169–11186, October 1996.

[85] P. Lautenschlager, M. Garriga, L. Vina, and M. Cardona. Temperature dependence of the dielectric function and interband critical points in silicon. *Physical Review B*, 36(9):4821–4830, September 1987.

[86] Prashant Shekhar, Marek Malac, Vaibhav Gaind, Neda Dalili, Al Meldrum, and Zubin Jacob. Momentum-Resolved Electron Energy Loss Spectroscopy for Mapping the Photonic Density of States. *ACS Photonics*, 4(4):1009–1014, April 2017.

[87] C. H. Chen and J. Silcox. Calculations of the electron-energy-loss probability in thin uniaxial crystals at oblique incidence. *Physical Review B*, 20(9):3605–3614, November 1979.

[88] Aycan Yurtsever, Martin Couillard, and David A. Muller. Formation of Guided Cherenkov Radiation in Silicon-Based Nanocomposites. *Physical Review Letters*, 100(21), May 2008.

[89] F. J. Garca de Abajo and A. Howie. Retarded field calculation of electron energy loss in inhomogeneous dielectrics. *Physical Review B*, 65(11):115418, March 2002.

[90] I. Frank and Ig Tamm. Coherent Visible Radiation of Fast Electrons Passing Through Matter. In *Selected Papers*, pages 29–35. Springer, Berlin, Heidelberg, 1991.

[91] Ido Kaminer, Yaniv Tenenbaum Katan, Hrvoje Buljan, Yichen Shen, Ognjen Ilic, Josu J. Lpez, Liang Jie Wong, John D. Joannopoulos, and Marin Soljai. Efficient plasmonic emission by the quantum erenkov effect from hot carriers in graphene. *Nature Communications*, 7:ncomms11880, June 2016.

[92] G. Adamo, K. F. MacDonald, Y. H. Fu, C-M. Wang, D. P. Tsai, F. J. Garca de Abajo, and N. I. Zheludev. Light Well: A Tunable Free-Electron Light Source on a Chip. *Physical Review Letters*, 103(11):113901, September 2009.

[93] Vincent Ginis, Jan Danckaert, Irina Veretennicoff, and Philippe Tassin. Controlling Cherenkov Radiation with Transformation-Optical Metamaterials. *Physical Review Letters*, 113(16):167402, October 2014.

[94] Rolf Erni and Nigel D. Browning. The impact of surface and retardation losses on valence electron energy-loss spectroscopy. *Ultramicroscopy*, 108(2):84–99, January 2008.

[95] Fang Liu, Long Xiao, Yu Ye, Mengxuan Wang, Kaiyu Cui, Xue Feng, Wei Zhang, and Yidong Huang. Integrated Cherenkov radiation emitter eliminating the electron velocity threshold. *Nature Photonics*, 11(5):289–292, May 2017.

[96] David E. Fernandes, Stanislav I. Maslovski, and Mrio G. Silveirinha. Cherenkov emission in a nanowire material. *Physical Review B*, 85(15), April 2012.

[97] Jin-Kyu So, Jong-Hyo Won, M. A. Sattorov, Seung-Ho Bak, Kyu-Ha Jang, Gun-Sik Park, D. S. Kim, and F. J. Garcia-Vidal. Cerenkov radiation in metallic metamaterials. *Applied Physics Letters*, 97(15):151107, October 2010.

[98] W. Knulst, M. J. van der Wiel, O. J. Luiten, and J. Verhoeven. High-brightness, narrowband, and compact soft x-ray Cherenkov sources in the water window. *Applied Physics Letters*, 83(19):4050–4052, November 2003.

[99] W. Knulst, O. J. Luiten, M. J. van der Wiel, and J. Verhoeven. Observation of narrow-band Si L-edge erenkov radiation generated by 5 MeV electrons. *Applied Physics Letters*, 79(18):2999–3001, October 2001.

[100] Mikhail Noginov, Mikhail Lapine, Viktor Podolskiy, and Yuri Kivshar. Focus issue: hyperbolic metamaterials. *Optics Express*, 21(12):14895–14897, June 2013.

[101] Evgenii E. Narimanov and Alexander V. Kildishev. Metamaterials: Naturally hyperbolic. *Nature Photonics*, 9(4):214–216, April 2015.

[102] M. N. Gjerding, R. Petersen, T. G. Pedersen, N. A. Mortensen, and K. S. Thygesen. Layered van der Waals crystals with hyperbolic light dispersion. *Nature Communications*, 8(1):320, August 2017.

[103] Joshua D. Caldwell, Andrey V. Kretinin, Yiguo Chen, Vincenzo Giannini, Michael M. Fogler, Yan Francescato, Chase T. Ellis, Joseph G. Tischler, Colin R. Woods, Alexander J. Giles, Minghui Hong, Kenji Watanabe, Takashi Taniguchi, Stefan A. Maier, and Kostya S. Novoselov. Sub-diffractional volume-confined polaritons in the natural hyperbolic material hexagonal boron nitride. *Nature Communications*, 5:5221, October 2014.

[104] Peining Li, Martin Lewin, Andrey V. Kretinin, Joshua D. Caldwell, Kostya S. Novoselov, Takashi Taniguchi, Kenji Watanabe, Fabian Gaussmann, and Thomas Taubner. Hyperbolic phonon-polaritons in boron nitride for near-field optical imaging and focusing. *Nature Communications*, 6:7507, June 2015.

[105] Jingbo Sun, Ji Zhou, Bo Li, and Feiyu Kang. Indefinite permittivity and negative refraction in natural material: Graphite. *Applied Physics Letters*, 98(10):101901, March 2011.

[106] Robert Warmbier, George S. Manyali, and Alexander Quandt. Surface plasmon polaritons in lossy uniaxial anisotropic materials. *Physical Review B*, 85(8):085442, February 2012.

[107] Moritz Esslinger, Ralf Vogelgesang, Nahid Talebi, Worawut Khunsin, Pascal Gehring, Stefano de Zuani, Bruno Gompf, and Klaus Kern. Tetradymites as Natural Hyperbolic Materials for the Near-Infrared to Visible. *ACS Photonics*, 1(12):1285–1289, December 2014.

[108] J Hubbard. The dielectric theory of electronic interactions in solids. *Proceedings of the Physical Society. Section A*, 68(11):976, 1955.

[109] Lukas Novotny and Bert Hecht. *Principles of Nano-Optics*. Cambridge University Press, Cambridge, 2 edition, 2012.

[110] Zubin Jacob and Vladimir M. Shalaev. Plasmonics Goes Quantum. *Science*, 334(6055):463–464, October 2011.

[111] Jorge Zuloaga, Emil Prodan, and Peter Nordlander. Quantum Description of the Plasmon Resonances of a Nanoparticle Dimer. *Nano Letters*, 9(2):887–891, February 2009.

[112] Giuseppe Toscano, Sren Raza, Antti-Pekka Jauho, N. Asger Mortensen, and Martijn Wubs. Modified field enhancement and extinction by plasmonic nanowire dimers due to nonlocal response. *Optics Express*, 20(4):4176–4188, February 2012.

[113] G.W. Hanson. Drift-Diffusion: A Model for Teaching Spatial-Dispersion Concepts and the Importance of Screening in Nanoscale Structures. *IEEE Antennas and Propagation Magazine*, 52(5):198–207, October 2010.

[114] R. F. Egerton. Electron energy-loss spectroscopy in the TEM. *Reports on Progress in Physics*, 72(1):016502, January 2009.

[115] J. B. Pendry. Negative Refraction Makes a Perfect Lens. *Physical Review Letters*, 85(18):3966–3969, October 2000.

[116] Graeme W. Milton, Nicolae-Alexandru P. Nicorovici, Ross C. McPhedran, and Viktor A. Podolskiy. A proof of superlensing in the quasistatic regime, and limitations of superlenses in this regime due to anomalous localized resonance.

Proceedings of the Royal Society of London A: Mathematical, Physical and Engineering Sciences, 461(2064):3999–4034, December 2005.

[117] D. Schurig, J. J. Mock, B. J. Justice, S. A. Cummer, J. B. Pendry, A. F. Starr, and D. R. Smith. Metamaterial Electromagnetic Cloak at Microwave Frequencies. *Science*, 314(5801):977–980, November 2006.

[118] Graeme W. Milton and Nicolae-Alexandru P. Nicorovici. On the cloaking effects associated with anomalous localized resonance. *Proceedings of the Royal Society of London A: Mathematical, Physical and Engineering Sciences*, 462(2074):3027–3059, October 2006.

[119] A. V. Kabashin, P. Evans, S. Pastkovsky, W. Hendren, G. A. Wurtz, R. Atkinson, R. Pollard, V. A. Podolskiy, and A. V. Zayats. Plasmonic nanorod metamaterials for biosensing. *Nature Materials*, 8(11):867–871, November 2009.

[120] Alexander A. Govyadinov and Viktor A. Podolskiy. Metamaterial photonic funnels for subdiffraction light compression and propagation. *Physical Review B*, 73(15):155108, April 2006.

[121] Igor I. Smolyaninov and Yu-Ju Hung. Modeling of time with metamaterials. *Journal of the Optical Society of America B*, 28(7):1591–1595, July 2011.

[122] J. B. Pendry, D. Schurig, and D. R. Smith. Controlling Electromagnetic Fields. *Science*, 312(5781):1780–1782, June 2006.

[123] Jonathan Plumridge and Chris Phillips. Ultralong-range plasmonic waveguides using quasi-two-dimensional metallic layers. *Physical Review B*, 76(7), August 2007.

[124] Na Liu, Hui Liu, Shining Zhu, and Harald Giessen. Stereometamaterials. *Nature Photonics*, 3(3):157–162, March 2009.

[125] David R. Smith, Pavel Kolinko, and David Schurig. Negative refraction in indefinite media. *JOSA B*, 21(5):1032–1043, May 2004.

[126] Viktor A. Podolskiy and Evgenii E. Narimanov. Strongly anisotropic waveguide as a nonmagnetic left-handed system. *Physical Review B*, 71(20):201101, May 2005.

[127] Pavel A. Belov, Constantin R. Simovski, and Pekka Ikonen. Canalization of subwavelength images by electromagnetic crystals. *Physical Review B*, 71(19):193105, May 2005.

[128] K. G. Balmain, A. A. E. Luttgen, and P. C. Kremer. Resonance cone formation, reflection, refraction, and focusing in a planar anisotropic metamaterial. *IEEE Antennas and Wireless Propagation Letters*, 1:146–149, 2002.

[129] Yu Guo, Ward Newman, Cristian L. Cortes, and Zubin Jacob. Applications of Hyperbolic Metamaterial Substrates. *Advances in OptoElectronics*, 2012, December 2012.

[130] M. A. Noginov, H. Li, Yu. A. Barnakov, D. Dryden, G. Nataraj, G. Zhu, C. E. Bonner, M. Mayy, Z. Jacob, and E. E. Narimanov. Controlling spontaneous emission with metamaterials. *Optics Letters*, 35(11):1863–1865, June 2010.

[131] Z. Jacob, J.-Y. Kim, G. V. Naik, A. Boltasseva, E. E. Narimanov, and V. M. Shalaev. Engineering photonic density of states using metamaterials. *Applied Physics B*, 100(1):215–218, July 2010.

[132] Jie Yao, Zhaowei Liu, Yongmin Liu, Yuan Wang, Cheng Sun, Guy Bartal, Angelica M. Stacy, and Xiang Zhang. Optical Negative Refraction in Bulk Metamaterials of Nanowires. *Science*, 321(5891):930–930, August 2008.

[133] Jie Yao, Xiaodong Yang, Xiaobo Yin, Guy Bartal, and Xiang Zhang. Three-dimensional nanometer-scale optical cavities of indefinite medium. *Proceedings of the National Academy of Sciences*, 108(28):11327–11331, July 2011.

[134] Zubin Jacob, Igor I. Smolyaninov, and Evgenii E. Narimanov. Broadband Purcell effect: Radiative decay engineering with metamaterials. *Applied Physics Letters*, 100(18):181105–181105–4, May 2012.

[135] Ivan Iorsh, Alexander Poddubny, Alexey Orlov, Pavel Belov, and Yuri S. Kivshar. Spontaneous emission enhancement in metaldielectric metamaterials. *Physics Letters A*, 376(3):185–187, January 2012.

[136] Alexander N. Poddubny, Pavel A. Belov, and Yuri S. Kivshar. Spontaneous radiation of a finite-size dipole emitter in hyperbolic media. *Physical Review A*, 84(2):023807, August 2011.

[137] Andrey S. Potemkin, Alexander N. Poddubny, Pavel A. Belov, and Yuri S. Kivshar. Green function for hyperbolic media. *Physical Review A*, 86(2):023848, August 2012.

[138] Alexander N. Poddubny, Pavel A. Belov, and Yuri S. Kivshar. Purcell effect in wire metamaterials. *Physical Review B*, 87(3):035136, January 2013.

[139] Yu Guo and Zubin Jacob. Thermal hyperbolic metamaterials. *Optics Express*, 21(12):15014–15019, June 2013.

[140] S.-A. Biehs, M. Tschikin, and P. Ben-Abdallah. Hyperbolic Metamaterials as an Analog of a Blackbody in the Near Field. *Physical Review Letters*, 109(10):104301, September 2012.

[141] Igor S. Nefedov and Constantin R. Simovski. Giant radiation heat transfer through micron gaps. *Physical Review B*, 84(19):195459, November 2011.

[142] D. R. Smith and D. Schurig. Electromagnetic Wave Propagation in Media with Indefinite Permittivity and Permeability Tensors. *Physical Review Letters*, 90(7):077405, February 2003.

[143] Dmitriy Korobkin, Burton Neuner, Chris Fietz, Nikoletta Jegenyes, Gabriel Ferro, and Gennady Shvets. Measurements of the negative refractive index of sub-diffraction waves propagating in an indefinite permittivity medium. *Optics Express*, 18(22):22734–22746, October 2010.

[144] Yi Xiong, Zhaowei Liu, Cheng Sun, and Xiang Zhang. Two-Dimensional Imaging by Far-Field Superlens at Visible Wavelengths. *Nano Letters*, 7(11):3360–3365, November 2007.

[145] Dylan Lu and Zhaowei Liu. Hyperlenses and metalenses for far-field super-resolution imaging. *Nature Communications*, 3:1205, November 2012.

[146] Gururaj V. Naik, Jongbum Kim, and Alexandra Boltasseva. Oxides and nitrides as alternative plasmonic materials in the optical range [Invited]. *Optical Materials Express*, 1(6):1090–1099, October 2011.

[147] Gururaj V. Naik and Alexandra Boltasseva. Semiconductors for plasmonics and metamaterials. *physica status solidi (RRL) Rapid Research Letters*, 4(10):295–297, October 2010.

[148] Sean Molesky, Christopher J. Dewalt, and Zubin Jacob. High temperature epsilon-near-zero and epsilon-near-pole metamaterial emitters for thermophotovoltaics. *Optics Express*, 21(101):A96–A110, January 2013.

[149] Alexandra Boltasseva and Harry A. Atwater. Low-Loss Plasmonic Metamaterials. *Science*, 331(6015):290–291, January 2011.

[150] Jean-Jacques Greffet, Rmi Carminati, Karl Joulain, Jean-Philippe Mulet, Stphane Mainguy, and Yong Chen. Coherent emission of light by thermal sources. *Nature*, 416(6876):61–64, March 2002.

[151] Thomas Taubner, Dmitriy Korobkin, Yaroslav Urzhumov, Gennady Shvets, and Rainer Hillenbrand. Near-Field Microscopy Through a SiC Superlens. *Science*, 313(5793):1595–1595, September 2006.

[152] M. A. Noginov, Yu A. Barnakov, G. Zhu, T. Tumkur, H. Li, and E. E. Narimanov. Bulk photonic metamaterial with hyperbolic dispersion. *Applied Physics Letters*, 94(15):151105, April 2009.

[153] W. Dickson, G. A. Wurtz, P. Evans, D. OConnor, R. Atkinson, R. Pollard, and A. V. Zayats. Dielectric-loaded plasmonic nanoantenna arrays: A metamaterial with tuneable optical properties. *Physical Review B*, 76(11):115411, September 2007.

[154] Jyotirmayee Kanungo and Joerg Schilling. Experimental determination of the principal dielectric functions in silver nanowire metamaterials. *Applied Physics Letters*, 97(2):021903, July 2010.

[155] B. D. F. Casse, W. T. Lu, Y. J. Huang, E. Gultepe, L. Menon, and S. Sridhar. Super-resolution imaging using a three-dimensional metamaterials nanolens. *Applied Physics Letters*, 96(2):023114, January 2010.

[156] Evgenii Narimanov and Igor Smolyaninov. Beyond Stefan-Boltzmann Law: Thermal Hyper-Conductivity. In *Conference on Lasers and Electro-Optics 2012*, OSA Technical Digest, page QM2E.1. Optical Society of America, May 2012.

[157] Evgenii Narimanov, M. A. Noginov, H. Li, and Yu. Barnakov. Darker than Black: Radiation-absorbing Metamaterial. In *Conference on Lasers and Electro-Optics 2010*, OSA Technical Digest (CD), page QPDA6. Optical Society of America, May 2010.

[158] Brahim Lounis and Michel Orrit. Single-photon sources. *Reports on Progress in Physics*, 68(5):1129, May 2005.

[159] Harish N. S. Krishnamoorthy, Zubin Jacob, Evgenii Narimanov, Ilona Kretzschmar, and Vinod M. Menon. Topological Transitions in Metamaterials. *Science*, 336(6078):205–209, April 2012.

[160] R. F. Egerton. *Physical Principles of Electron Microscopy: An Introduction to TEM, SEM, and AEM*. Springer US, 2005.

Appendix A

The Energy Loss Function and Electron Scattering Probability in Uniaxial Media

A.1 Introduction

In this appendix, we provide a derivation of the dielectric theory of the scattering and energy loss of fast electrons in uniaxial media. Fast moving electrons (or any charged particle) ionize atoms and lose energy as they pass through matter. For solid and liquid matter, the energy loss of the electron can be macroscopically determined to be a result of the dielectric polarization of the medium by the charge. The work done on the fast electron by the induced fields is directly related to the energy loss of the electron.

Specifically, here we will discuss the energy loss of electrons in anistropic uniaxial structures via the macroscropic uniaxial dielectric permittivity of the structure with the aid of Maxwell's equations. This treatment is outlined in detail in the work of Chen et. al [87] but we provide an overview in this thesis for completeness. The equations presented here are the primary equations used to calculate the theoretical momentum-resolved electron scattering probability in chapters 2,3 and 4 of this thesis used to corroborate the k-EELS measurements.

A.2 The Energy Loss Function and Electron Scattering Probability in Uniaxial Media: Dielectric Approximation

A schematic representing the geometry of our system is shown in figure A.1. We consider an electron traveling in the z-direction parallel to c-axis of a uniaxial struc-
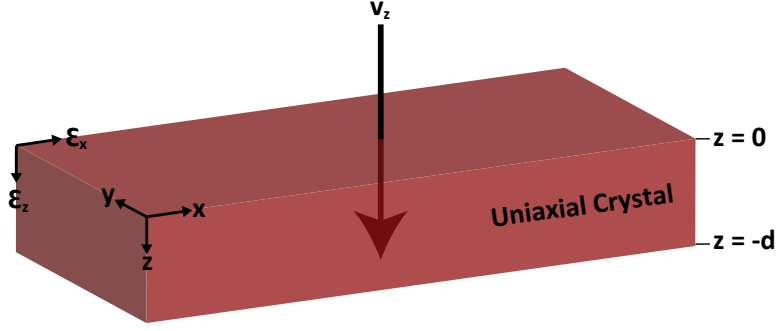
Figure A.1: Schematic of a uniaxial crystal of thickness d with an electron normally incident with velocity v_z

ture with thickness d. The uniaxial crystal is describe with a dielectric permittivity perpendicular (ϵ_x) and parallel (ϵ_z) to the c-axis, respectively. Note, that we assume the magnitude of the velocity of the electron to remain constant. This is valid as we are looking at very small energy losses of the electron compared to the initial electron energy (an order of magnitude difference of $\approx 10^5$ eV).

The electron is treated as a moving point charge ($-e$) with a charge distribution $\rho(z,t) = -e\delta(z - v_z t)\delta(x)\delta(y)$, where v_z is the velocity of the electron. The time and space (in the $x - y$ plane) fourier transform of the charge distribution is thus defined as:

$$\rho(z, k_x, k_y, \omega) = \frac{-e}{v_z} e^{-i\omega z/v_z} \tag{A.1}$$

with a current density

$$\vec{j}(z, k_x, k_y, \omega) = v_z \rho(z, k_x, k_y, \omega) \tag{A.2}$$

From the full set of Maxwell's equations for a nonmagentic material ($\vec{B} = \vec{H}$), we can eliminate the magnetic field to write it in the following form:

$$\vec{\nabla}(\vec{\nabla} \cdot \vec{E}) - \nabla^2 \vec{E} + \frac{1}{c^2}\frac{\partial^2 \vec{D}}{\partial t^2} + \frac{4\pi}{c^2}\frac{\partial \vec{j}}{\partial t} = 0 \tag{A.3}$$

where we have an external charge density from the electron and thus $\nabla \cdot \vec{D} = 4\pi\rho$ and $\vec{D} = \bar{\epsilon}E$. We thus get a set of 3 differential equations for a uniaxial structure with an external point charge source with a velocity v_z:

$$\left(k_x^2 - \frac{\epsilon_z}{\epsilon_x}\frac{\partial^2}{\partial z^2} - \epsilon_z\frac{\omega^2}{c^2}\right) E_z(z, k_y, k_x, \omega) = \frac{4\pi e}{i\epsilon_x v_z}\left(k_z - \frac{\omega}{c^2}\epsilon_x v_z\right) e^{-ik_z z} \tag{A.4}$$

$$\left(k_x^2 - \frac{\partial^2}{\partial z^2} - \epsilon_z \frac{\omega^2}{c^2}\right) E_x(z, k_y, k_x, \omega) = \frac{4\pi e}{i\epsilon_x v_z}(-k_x e^{-ik_z z}) - ik_x \left(1 - \frac{\epsilon_z}{\epsilon_x}\right) \frac{\partial E_z(z, k_y, k_x, \omega)}{\partial z} \tag{A.5}$$

$$\left(k_x^2 - \frac{\partial^2}{\partial z^2} - \epsilon_z \frac{\omega^2}{c^2}\right) E_y(z, k_y, k_x, \omega) = \frac{4\pi e}{i\epsilon_x v_z}(-k_y e^{-ik_z z}) - ik_y \left(1 - \frac{\epsilon_z}{\epsilon_x}\right) \frac{\partial E_z(z, k_y, k_x, \omega)}{\partial z} \tag{A.6}$$

As stated earlier, the work done (W) on the electron by the fields induced by the electron corresponds to the energy lost by the electron. As our electron is traveling only along the z-direction (as multiple scattering events are ignored), the force acting on the electron can only come from the fields also in the z-direction (i.e $F_z = -eE_z(z, k_y, k_x, \omega)$). Therefore, we integrate this force component along the path of the incident electron to find the energy loss from the fourier components of the field:

$$W(k_y, k_x, \omega) = \frac{-e}{(2\pi)^3} \int_{-\infty}^{\infty} E_z(z, k_y, k_x, \omega) e^{ik_z z} dz \tag{A.7}$$

The energy loss probability (P), as described in [87] and in detail in [108], per unit frequency and wavevector is thus:

$$\frac{\partial^3 P(k_y, k_x, \omega)}{\partial \omega \partial k_y \partial k_x} = \frac{2}{\hbar \omega} Re(W(k_y, k_x, \omega)) \tag{A.8}$$

Now all that is left to determine the energy loss probability is to solve for the fields. As we have an external source, the solutions to equations A.5, A.6, and A.4 will have both particular and homogeneous (source free solutions). The particular solutions correspond to volume losses in the structure while the homogeneous solutions correspond to what are known as surface losses in the structure. We will first look at the volume loss contributions to the energy loss.

Volume Energy Loss Probability

As stated the volume loss contributions to the total energy loss can be determined from the particular solutions of equations A.5, A.6, and A.4. Note, as we are only considering electrons with normal incidence, we are only interested in the E_z field component which acts directly on the electron. We can easily solve for E_z directly from equation A.4:

$$E_z^{vol}(z, k_x, k_y, \omega) = \frac{4\pi e}{i\epsilon_x v_z \phi_z^2} \left(k_z - \frac{\omega}{c^2} v_z \epsilon_x \right) e^{-ik_z z}$$

(A.9)

$$where \quad \phi_z^2 = k_x^2 + \frac{\epsilon_z}{\epsilon_x} k_z^2 - \epsilon_z \frac{\omega^2}{c^2}$$

Now that we determined the form E_z we can solve the integral in equation A.7 to determine the energy loss of the electron. We can subsequently substitute W into equation A.8 to determine the *volume* energy loss scattering probability in a uniaxial material for electrons with normal incidence:

$$\boxed{P_{volume} = \frac{e^2}{\pi^2 \hbar^2 v_z^2} Im \left(\frac{1 - \epsilon_x \frac{v_z^2}{c^2}}{\epsilon_x \phi_z^2} \right) d}$$

(A.10)

Surface Energy Loss Probability

Now that we have solved the particular solutions for the series of differential equations A.5, A.6 and A.4 to determine the volume loss contributions, we must now solve the homogeneous solutions for the same equations to determine what are called the "surface losses". These are essentially the homogeneous solutions to Maxwell's equations arising from the boundary conditions at the interfaces.

The total electric field induced in the uniaxial material by the electron is of course the sum of the particular and homogeneous solutions. Thus the homogeneous solutions will also result in a force acting along the path of the incident electron that will contribute to the total energy loss experienced by the electron.

We start with the source free ($\vec{\nabla} \cdot \vec{D} = 0$) homogeneous solutions to equation A.3

$$\left(k_x^2 - \frac{\epsilon_z}{\epsilon_x} \frac{\partial^2}{\partial z^2} - \epsilon_z \frac{\omega^2}{c^2} \right) E_z(z, k_y, k_x, \omega) = 0$$

(A.11)

$$\left(k_x^2 - \frac{\partial^2}{\partial z^2} - \epsilon_z \frac{\omega^2}{c^2} \right) E_x(z, k_y, k_x, \omega) = -ik_x \left(1 - \frac{\epsilon_z}{\epsilon_x} \right) \frac{\partial E_z(z, k_y, k_x, \omega)}{\partial z}$$

(A.12)

$$\left(k_x^2 - \frac{\partial^2}{\partial z^2} - \epsilon_z \frac{\omega^2}{c^2} \right) E_y(z, k_y, k_x, \omega) = -ik_y \left(1 - \frac{\epsilon_z}{\epsilon_x} \right) \frac{\partial E_z(z, k_y, k_x, \omega)}{\partial z}$$

(A.13)

We once again must solve for the field component E_z (the component acting on

the electron), which has the general form:

$$E_z^{surf} = Acosh(\eta z) + Bsinh(\eta z)$$

$$(A.14)$$

$$where \quad \eta = \sqrt{(\epsilon_x(k_x^2 - \epsilon_z\omega^2/c^2)/\epsilon_z}$$

and A and B are unknown constants. We can achieve similar expressions for E_x^{surf} and E_y^{surf} by subbing our general solution for E_z^{surf} into equations A.12 and A.13, respectively. The expressions for the fields outside of the sample thickness (d) (figure A.1) can be expressed as:

$$\vec{E}_0^{surf}(x, k_y, k_x, \omega) = \vec{C}e^{-\lambda_0(z)}, \quad 0 < z < \infty$$
$$\vec{E}_0^{surf}(x, k_y, k_x, \omega) = \vec{F}e^{\lambda_0(z-d)}, \quad -\infty < z < -d \qquad (A.15)$$
$$where \quad \lambda_0 = \sqrt{k_x^2 - \epsilon_0\omega^2/c^2}$$

and $\vec{C}$ and $\vec{F}$ are constants with 3 components that need to be determined.

There is now the issue of solving for the series of unknown constants. Using Maxwell's equations, we can write expressions for the magnetic field using the total electric field (i.e $\vec{E} = \vec{E}^{vol} + \vec{E}^{surf}$). We can then apply the boundary conditions for both the electric and magnetic fields at each of the interfaces to determine the series of unknowns and solve for $E_z^{surf}(z, k_y, k_z, \omega)$ seen in equation A.14. Once the solution to $E_z^{surf}(z, k_y, k_z, \omega)$ has been determined, it can once again be subbed into equations A.7 and A.8 to determine the *surface* energy loss probability. This is a tedious process that will not be derived in detail here, however further details can be seen in [87]. Instead, we provide the final form for the surface energy loss scattering

probability in a uniaxial crystal from normally incident electrons:

$$P_{surf} = \frac{e^2}{\pi^2\hbar^2 v_z^2} Im\left[- \frac{2k_x^2}{\phi_z^2\phi_x^2\phi_0^4\epsilon_0\epsilon_x}\left[(\epsilon_0\phi_0^2 - \epsilon_x\phi_z^2)(\epsilon_0(1+\Delta)\phi_0^2 - \epsilon_x\phi_x^2) \right.\right.$$

$$\times\left(\frac{sin^2(\omega d/(2v_z))}{L^+} + \frac{cos^2(\omega d/(2v_z))}{L^-}\right)$$

$$+\lambda_0\eta\epsilon_0\frac{\phi_x^2}{\phi_z^2}(\epsilon_z\mu^2 - \epsilon_x\mu_0^2)(\phi_0^2 - \phi_x^2)\left(\frac{cos^2(\omega d/(2v_z))tanh(\eta d/2)}{L^+} + \frac{sin^2(\omega d/(2v_z))coth(\eta d/2)}{L^-}\right)$$

$$+\left(\frac{v_z}{\omega}\lambda_0\epsilon_x(\phi_z^2 - \phi_0^2)(\epsilon_0(1+\Delta)\phi_0^2 - \epsilon_x\phi_x^2) + \frac{\omega\phi_x^2}{v_z\phi_z^2}\lambda_0(\epsilon_z\mu^2 - \epsilon_x\mu_0^2)(\epsilon_0\phi_0^2 - \epsilon_x\phi_z^2)\right)$$

$$\left.\left.\times\left(\frac{1}{L^+} - \frac{1}{L^-}\right)sin(\omega d/(2v_z))cos(\omega d/(2v_z))\right]\right]$$

$$where \quad \phi_x^2 = \frac{\omega^2}{v_z}^2 + k_x^2 - \epsilon_x\frac{\omega^2}{c^2}, \quad \phi_0^2 = \frac{\omega^2}{v_z}^2 + k_x^2 - \epsilon_0\frac{\omega^2}{c^2},$$

$$\Delta = \left(1 - \frac{\epsilon_z}{\epsilon_x}\right)\frac{(\omega/v_z)^2}{\phi_z}(1 - \epsilon_x(v_z/c)^2), \quad \mu^2 = 1 - \epsilon_x(v_z/c)^2, \quad \mu_0^2 = 1 - \epsilon_0(v_z/c)^2,$$

$$L^+ = \lambda_0\epsilon_x + \eta\epsilon_0tanh(\eta d/2), \quad and \quad L^- = \lambda_0\epsilon_x + \eta\epsilon_0coth(\eta d/2)$$

$$(A.16)$$

Appendix B

The Photonic Density of States

B.1 Introduction

In general the density of states (DOS) describes the number of available states to be occupied per interval of energy in a given system. Depending on the type of system and parameter of interest the density of states can be calculated for electrons, photons or phonons and is generally a function of the energy, E, the wavevector, k, or both (sometimes called the wavevector-resolved density of states). The DOS for photons, known as the photonic density of states (PDOS), provides us a means by which to quantify light matter interactions. One can think of it as a mode counting procedure of the photonic states available per interval of energy in k-space.

For example, to determine the number and types of photonic modes supported by a structure, we consider Maxwell's wave equation in the following form:

$$\nabla \times \nabla \times \vec{E} + \frac{\bar{\epsilon}}{c^2} \frac{\partial^2 \vec{E}}{\partial t^2} = 0 \tag{B.1}$$

where the dielectric permittivity tensor $\bar{\epsilon}$ gives the macroscopic material response through which our wave is propagating, and we can find solutions for $\vec{E}$ of the form $\vec{E} = E_0 e^{\vec{k} \cdot r - i\omega t}$. If we now consider an isotropic medium ($\bar{\epsilon} = \epsilon$), we see that our dispersion relation takes on the form: $k_x^2 + k_y^2 + k_z^2 = \epsilon k_0^2$, where $k_0 = \omega/c$. We see that at one particular frequency, ω, we can map the dispersion visually in k-space, known as the isofrequency surface. For an isotropic material, where $\epsilon > 0$, we see that we get an isofrequency surface in the shape of a sphere (figure B.1 (a)). We see that the magnitudes of the wavevectors that our supported by our structure must be at the bounds of the surface of the sphere, and modes with wavevectors larger than this bound will not be supported by the material and evanescently decay.

Through the dispersion relation and isofrequency surface, we see that we now have means to quantify the types of modes that are supported by our structure at a single frequency. If we now consider our system at two separate frequencies, ω_1 and ω_2 with a difference $d\omega$, we see that we can overlay two separate isofrequency surfaces on top of one another (figure B.1 (b)). The volume in between these two isofrequency surface provides us means by which to quantify the *number* of modes that exist within the range dω which is defined as the photonic density of states.
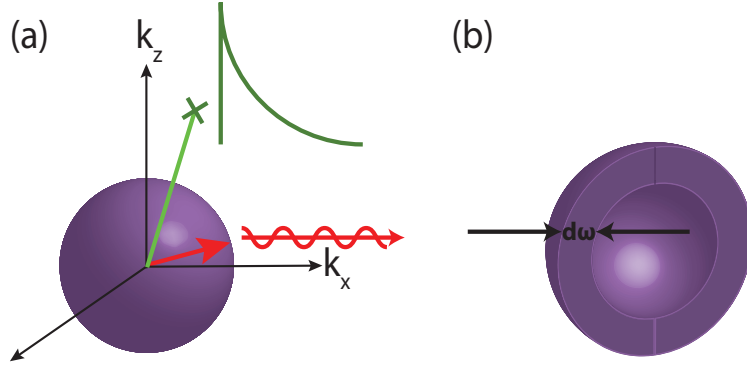
Figure B.1: (a) Spherical isofrequency surface in k-space for an isotropic dielectric with $\epsilon > 0$. Photonic modes with wavevector magnitudes greater than the bound surface of the sphere will evanescently decay and are not supported by the structure. (b) Two isofrequency surfaces at frequency ω_1 and ω_2 with a difference $d\omega$ overlayed on top of each other. The volume in between the two spheres is a measure of the photonic density of states used to quantify light matter interaction.

As an aside, it is important to note that the general approach taken to define of the density of states above for photons can also be applied analogously to electrons with the Fermi surface. However, the differing dispersion relations of the two elementary particles consequently leads to different shapes of their constant energy surfaces (i.e the isofrequency surface or the Fermi surface). This, in turn, changes the proportionality of the DOS with respect to the energy for the electron and photon. For example, the electrons have a parabolic dispersion, $E = E_0 + \frac{(\hbar k)^2}{2m_e}$, and photons have a linear dispersion, $E = E_0 + \hbar kc$, where m_e is the electron mass and c is the speed of light in vacuum. In general, the DOS in 3D for a dispersion relation of the form $E = E_0 + Ck^p$, in units of $energy^{-1}volume^{-1}$ can be expressed as:

$$DOS(E)_{3D} = \frac{4\pi}{pC^{3/p}}(E - E_0)^{3/p-1} \tag{B.2}$$

where p is the order of the dispersion relation and C is a constant. From the case of linear dispersion of the photon $p = 1$ and for the parabolic disperison of the electron we have $p = 2$ we immediately see:

$$
\begin{aligned}
DOS(E)_{3D} &\propto E^{1/2} \quad electrons \\
DOS(E)_{3D} &\propto E^2 \quad photons
\end{aligned}
\tag{B.3}
$$

While the mode counting approach explained above provides an intuitive picture about the photonic density of states, there is still the question about how one actually measures the quantity in experiment. The PDOS is in fact directly proportional to the average power

66

dissipated ($\langle P \rangle$) from a source [109, 68]. One can express this average power dissipation of a dipole in vacuum through the imaginary component of the electromagnetic Green's tensor ($\bar{G}$):

$$\langle P \rangle \quad = \quad \frac{2\pi\mu\omega^3}{c^2}\mathrm{Im}\left[\vec{\mu}^* \cdot \bar{G}(\vec{r_o}, \vec{r_o}) \cdot \vec{\mu}\right] \tag{B.4}$$

where $\vec{\mu}$ is the dipole moment. The use of the Green's function to define our PDOS will prove useful when looking at more complicated systems with a variety of materials and complex electromagnetic fields.

In the following sections, we will derive the form of $\bar{G}$ used for electrodynamics in this thesis. At the end, we provide a mathematical definition for calculating the photonic density of states for a planar structure normalized by the free space density of states.

B.2 Green's Function Technique

Generally, the mathematical Green's function technique can be understood as a spatial extension of the impulse response formalism employed in introductory signals and systems. In such descriptions, a complete temporal relation between cause and effects is built up by considering a systems response to an unitary impulse input. Building on this notion, the Green's function technique is a prescription for fully describing the spatial and temporal correlation of inputs and outputs based on point sources.

Mathematical Description. One dimensional time independent example: Φ a one dimensional function, $\hat{D}$ a one dimensional operator, $G(x, x')$ the greens function of the solution, δ the delta Dirac function and f(x) a source term.

$$\hat{D}\langle \Phi \rangle \quad = \quad f(x) \tag{B.5}$$

$$\hat{D}\langle G(x, x')\rangle \quad = \quad \delta(x - x') \tag{B.6}$$

$$f(x')\hat{D}\langle G(x, x')\rangle \quad = \quad f(x')\delta(x - x') \tag{B.7}$$

$$\int f(x')\hat{D}\langle G(x, x')\rangle\,\mathrm{d}x \quad = \quad f(x) \tag{B.8}$$

$$\hat{D}\left\langle \int f(x')G(x, x')\mathrm{d}x \right\rangle \quad = \quad f(x) \tag{B.9}$$

Leading to the conclusion that Φ may be represented as

$$\boxed{\Phi = \int f(x')G(x, x')\mathrm{d}x + \Phi_o} \tag{B.10}$$

The Green's function $G(x, x')$ correlates the response Φ to the source $f(x)$.

B.3 Green's Function for Electromagnetic Sources

B.3.1 The Helmholtz Equation

Having some notion of the Green's function technique, we will now turn our attention to solving a differential form which may be used for electrodynamics. First, it is useful to start with the Helmholtz equation, which is a differential equation for the function $\Psi(\vec{r})$ of the form

$$\left(\nabla^2 + k^2\right)\Psi(\vec{r}) = S(\vec{r}) \tag{B.11}$$

where $S(\vec{r})$ is some source function.

Following the outline dictated in the preceding subsection, in order to use the Green's function approach we must first find a solution to the equation

$$\left(\nabla^2 + k^2\right)g(\vec{r}, \vec{r'}) = \delta(\vec{r} - \vec{r'}) \tag{B.12}$$

which, by taking $\vec{r'}$ to be at the origin, and performing a Fourier transform

$$g(r) = \iiint \frac{\mathrm{d}^3 q}{(2\pi)^3} \tilde{g}(\vec{q}) e^{i\vec{q}\cdot\vec{r}} \tag{B.13a}$$

$$\delta(\vec{r}) = \iiint \frac{\mathrm{d}^3 q}{(2\pi)^3} e^{i\vec{q}\cdot\vec{r}} \tag{B.13b}$$

may be rearranged to produce

$$\iiint \frac{\mathrm{d}^3 q}{(2\pi)^3}(-q^2 + k^2)\tilde{g}(\vec{q}) e^{i\vec{q}\cdot\vec{r}} = \iiint \frac{\mathrm{d}^3}{(2\pi)^3} e^{i\vec{q}\cdot\vec{r}} \tag{B.14}$$

As this equation must hold for all k and q, we may equate the terms under the integral and solve for the fourier transform of the greens function, $\tilde{g}(\vec{q})$ as

$$\tilde{g}(q) = \frac{1}{k^2 - q^2} \tag{B.15}$$

and therefore, $g(r)$ can be expressed as

$$\iiint \frac{\mathrm{d}^3 q}{(2\pi)^3} \frac{1}{k^2 - q^2} e^{i\vec{q}\cdot\vec{r}} \tag{B.16}$$

By orienting $\vec{r}$ along the polar axis, switching to polar coordinates, and making use of the Cauchy integral formula, this result may be solved to yield the scalar green's function for the Helmholtz equation which can be used to solve any equation that may be placed in the Helmholtz form.

$$\boxed{g(r) = -\frac{e^{ikr}}{4\pi r}} \tag{B.17}$$

B.3.2 Relating Maxwell's Equations to the Helmholtz Form

Recalling the standard differential forms of Maxwell's equation:

$$\vec{\nabla} \cdot \vec{D} = 4\pi\rho \tag{B.18}$$

$$\vec{\nabla} \cdot \vec{B} = 0 \tag{B.19}$$

$$\vec{\nabla} \times \vec{E} = -\frac{1}{c}\frac{\partial \vec{B}}{\partial t} \tag{B.20}$$

$$\vec{\nabla} \times \vec{H} = \frac{4\pi}{c}\vec{J} + \frac{1}{c}\frac{\partial \vec{D}}{\partial t} \tag{B.21}$$

and the potential definitions:

$$\vec{B} = \vec{\nabla} \times \vec{A} \tag{B.22}$$

$$\vec{E} = -\frac{1}{c}\frac{\partial \vec{A}}{\partial t} - \vec{\nabla}\phi \tag{B.23}$$

It is possible to cast Maxwell's equations into the familiar form of the Helmholtz equation. By taking the source free Maxwell's equation B.21 and subbing in the appropriate potential formulations, described by equations B.22 and B.23, we get

$$\vec{\nabla} \times \left(\vec{\nabla} \times \vec{A} \right) = \frac{4\pi\mu}{c}\vec{J} + \frac{\epsilon\mu}{c^2}\frac{\partial}{\partial t}\left(-\frac{\partial \vec{A}}{\partial t} - \vec{\nabla}\phi c \right) \tag{B.24}$$

which can then be manipulated by employing differential vector identities and making use of the Lorenz gauge[1] to return us to an equation of the Helmholtz form as follows.

$$\nabla^2 \vec{A} - \frac{\epsilon\mu}{c^2}\frac{\partial^2 \vec{A}}{\partial t^2} = \frac{-4\pi\mu\vec{J}}{c} \tag{B.25}$$

$$\frac{\partial^2 \vec{A}}{\partial t^2} = -\omega^2 \vec{A} \tag{B.26}$$

$$\Rightarrow \boxed{\left(\nabla^2 \cdot + \epsilon\mu k_0^2 \right)\vec{A} = -\frac{4\pi\mu}{c}\vec{J}} \tag{B.27}$$

In turn, this result also allows us to solve for the electric field by noting the relation between the scalar and vector fields imposed by the Lorenz gauge and noting the potential relation B.23.

$$\vec{E} = -\frac{1}{c}\frac{\partial \vec{A}}{\partial t}\frac{1}{i\epsilon\mu k_0}\vec{\nabla}\left(\vec{\nabla} \cdot \vec{A} \right) \tag{B.28}$$

As shown above, under the assumption of time harmonic fields, equation B.27 can be rewritten as:

$$(k_1^2 + \nabla^2\cdot)\vec{A} = \frac{-4\pi\mu}{c}\vec{J} \tag{B.29}$$

where $k_1^2 := \epsilon\mu k_0^2 = \frac{\epsilon\mu\omega^2}{c^2}$. This then leads to the formula for $\vec{E}$

$$\left(-k_1^2 + \vec{\nabla} \times \vec{\nabla} \times \right)\vec{E} = i\frac{4\pi\mu k_0}{c}\vec{J} \tag{B.30}$$

---

[1]The Lorenz gauge under time harmonic assumptions is $0 = \nabla \cdot \vec{A} - \epsilon\mu\frac{\partial\phi}{\partial t}$.

Therefore, by drawing from the arguments presented earlier about Green's functions we may now write

$$\left(-k_1^2 + \vec{\nabla} \times \vec{\nabla} \times\right) \bar{G}_x = i\frac{4\pi\mu k_0}{c}\vec{\delta_x} \tag{B.31}$$

By performing this computation in each direction $(x, y, \text{and } z)$ we can determine the expression for the Dyadic Green's function for electromagnetic sources and therefore arrive at a general result for computing electric fields due to a general source $\vec{J}$

$$\vec{E}(\vec{r}) = 0 + i\frac{4\pi\mu k_0}{c}\int \bar{G}\vec{J}\mathrm{d}V' \tag{B.32}$$

Recalling that an oscillating, and therefore radiating, point dipole positioned at $\vec{r}'$ and pointed in the direction $\vec{\mu}$ may be written as

$$\vec{\mu}(\vec{r}, t) = \vec{\mu}\delta(\vec{r} - \vec{r'})e^{-i\omega t} \tag{B.33}$$

and that this approximately corresponds to a current of $\vec{J}(\vec{r}, t) = \frac{\partial \vec{u}}{\partial t}$, by setting the phase of the dipole equal to unity we may conclude that[2]

$$\begin{aligned} \vec{E}(\vec{r}) &= i\frac{4\pi\mu\omega}{c^2}\int \bar{G}\left(\vec{r}, \vec{r}\right)(-i\omega)\vec{\mu}\delta(\vec{r} - \vec{r}\,')\mathrm{d}V' \\ &= 4\pi\mu k_0^2 \bar{G}\left(\vec{r}, \vec{r}\right)\vec{\mu} \end{aligned} \tag{B.34}$$

As we are aware that,

$$\vec{E} = ik_0\left[1 + \frac{\vec{\nabla}\vec{\nabla}}{k_1^2}\right]\vec{A} \tag{B.35}$$

we may finally establish that a fixed form for our Dyadic Green's function is given by: [3]

$$\boxed{\bar{G} = \left[\bar{I} + \frac{\vec{\nabla}\vec{\nabla}}{k_1^2}\right]g(\vec{r})} \tag{B.36}$$

where $g(\vec{r})$ is the Green's function of the Helmholtz equation. Which, following the derivation of the Weyl's identity, may be written as:

$$g(r) = -\frac{e^{ikr}}{4\pi r} = \frac{i}{8\pi^2}\iint\limits_{-\infty}^{\infty}\mathrm{d}k_x\mathrm{d}k_y\frac{1}{k_z}e^{i(k_x x + k_y y + k_z|z|)} \tag{B.37}$$

We now have a useful form for finding extremely complicated electric fields due to general sources.

---

[2]μ denotes magnetic permeability, $\vec{\mu}$ the dipole moment.

[3]The $\vec{\nabla}$ operator acts to increase the dimension of the operand.

B.4   Semi Classical Theory of Spontaneous Emission

B.4.1   Introduction

Building off the results of the previous section we are now in a position to use the Green's function formalism to determine the lifetime of a spontaneous emitter, such as a simple system with two quantized energy levels.

Recalling Fermi's Golden rule:

$$\Gamma_s = \frac{2\pi}{\hbar} \left| \langle \Psi_f \left| H_{int} \right| \Psi_i \rangle \right|^2 n(\epsilon_f) \tag{B.38}$$

(where Ψ is used to represent quantum states, $n(\epsilon_f)$ the final density of states, H the Hamiltonian of the system and Γ the rate of decay of the system.)

It quickly becomes clear that the lifetime of an excited state relies heavily on the density of final available states to the excitation; or, from an anthropomorphic perspective, the likelihood of a transition to another state depends on how much space the excitation knows is available at that particular energy. If we now make use of semi-classical techniques, we can deduce from arguments about the proportionality of the density of states that

$$\Gamma = \frac{P}{\hbar\omega} \tag{B.39}$$

(where P is the average power emitted from the system).

B.4.2   Lifetime of a Spontaneous Emitter Dipole

Using the Green's function result from equation B.34 along with knowledge from classical electrodynamics that

$$\langle P \rangle = \int \frac{1}{2} \mathrm{Re} \left(\vec{J}^* \cdot \vec{E} \right) \mathrm{d}V' \tag{B.40}$$

we can now determine the average power emitted by a dipole. Using a time harmonic approach, identical to the one used in the preceding section, we will assume that the dipole produces a current of

$$\vec{J} = -i\omega\vec{\mu}e^{-i\omega t}\delta(\vec{r} - \hat{z}d) \tag{B.41}$$

Which then leads to the result:

$$\langle P \rangle = \int \frac{1}{2} \mathrm{Re} \left[i\omega\vec{\mu}^* \left(\frac{\omega}{c} \right)^2 \delta(\vec{r} - \vec{r_o}) 4\pi\mu G(\vec{r},\vec{r_o})\vec{\mu} \right] \mathrm{d}V' \tag{B.42}$$

$$\langle P \rangle = \frac{2\pi\mu\omega^3}{c^2} \mathrm{Im} \left[\vec{\mu}^* \cdot \bar{G}(\vec{r_o},\vec{r_o}) \cdot \vec{\mu} \right] \tag{B.43}$$

with $\bar{G}$ given by

$$\bar{G} = \left[\bar{I} + \frac{\vec{\nabla}\vec{\nabla}}{k_1^2} \right] \left(\frac{i}{8\pi^2} \iint\limits_{-\infty}^{\infty} \mathrm{d}k_x \mathrm{d}k_y \frac{1}{k_z} e^{i(k_x x + k_y y + k_z|z|)} \right) \tag{B.44}$$

If we orient our space such that the dipole is oriented along a single direction, say the $\hat{z}$ direction, and is positioned at the origin, B.44 may be solved by the aid of trigonometric

substitutions to yield:

$$\langle P \rangle = \frac{n\mu\omega^4}{3c^3}\, |\vec{\mu}|^2 \qquad\qquad\text{(B.45)}$$

where n is the index of refraction, and $|\vec{\mu}|$ is the magnitude of the dipole vector. All other symbols follow the standard convention. *Note* that this is an expression for the average power emitted for a dipole in free space and is analogous to the photonic density of states in *vacuum*.

B.4.3 Lifetime of a Spontaneous Emitter in the Presence of a Planar Material

Given the manner and formalism of the previous subsection, calculating the lifetime of a spontaneous emitter in the presence of material is actually much simpler than one might initially think. As we must only consider the Green's function at the location of the current, in this case the dipole, in order to calculate the emitted power, and associated decay rate, our task is simplified to determining the electric field at the position of the dipole. Thus, the only change that must be made to the conclusions of the previous subsection is to replace free emission electric field by:

$$\vec{E} = 4\pi \left(\frac{\omega}{c}\right)^2 (\bar{G}_{free} + \bar{G}_{ref}) \cdot \vec{\mu} \qquad\qquad\text{(B.46)}$$

Where $\bar{G}_{free}$ is identical to the Green's function presented in the previous subsection, and $\bar{G}_{ref}$ is defined using the p-polarization (TM) reflection coefficient r_p as $\bar{G}_{ref} = r_p \bar{G}_{inc}$.[4]

Drawing from the previous subsection, and normalizing the power with result from equation B.45, leads us to the conclusion that the normalized decay rate of a spontaneous emitter a distance d from a planar interface is found to be:

$$\frac{\Gamma}{\Gamma_o} \propto \frac{P}{P_o} = \text{Re}\left[\int_0^\infty \rho(k,\omega,d) dk_x \right] \qquad\qquad\text{(B.47)}$$

where $\rho(k,\omega,d)$ is the momentum-resolved photonic density of states normalized to free space for a vertically oriented dipole:

$$\rho(k,\omega,d) = \frac{3}{2(k_0\sqrt{\epsilon_1})^3} \frac{k_x^3}{k_z}\left(1 + r_p e^{i2k_z d}\right) \qquad\qquad\text{(B.48)}$$

Note that r_p can be calculated in the effective medium limit for a slab or for a multilayer structure via the transfer matrix method as seen in appendix G.

---

[4]a dipole oriented perpendicular to an interface will emit only p-polarized light (TM) with respect to that interface.

Appendix C

Surface Plasmon Polaritons in a Local Drude Metal

The local drude model is a widely adapted framework to describe free electron motion in metallic structures. It is termed "local" as the dielectric permittivity (ϵ) depends only on the frequency (ω) and not the wavevector (k) of the incoming excitation radiation. Specifically, in the local model, the response of a material to an electric field depends on the field at a particular point (k) with no dependence of the response at another point (k').

In this appendix we briefly discuss the dispersive characteristics of surface plasmon polaritons (SPPs) of a local drude metal. Note, the SPP dispersion probed by k-EELS in Ag (chapter 2) and silicon (chapter 3)) can be described by a local drude model with additional lorentzian terms that incorporate the interband transitions in the material. Here we only look at the free electron (drude) component of the permittivity that is the basis of the SPP excitation.

Metals interact with electromagnetic radiation through the motion of their free electrons as described by the permittivity for the local drude model:

$$\epsilon(\omega) = 1 - \frac{\omega_p^2}{\omega^2 + i\gamma\omega} \tag{C.1}$$

$$\omega_p = \sqrt{\frac{Ne^2}{m_e\epsilon_0}} \tag{C.2}$$

γ is the electron dephasing or scattering rate. It is a representation of the inherent losses in the metal due to non-idealities, phonon scattering and other material absorptions that dampen any resonant behaviour of the electrons. Here, m_e is the effective electron mass and ω_p represents the plasma frequency of the metal, which is proportional to the square root of the electron density, N. The plasma frequency is measure of the nature of the response of the electrons in the metal and it indicates the ability of the electrons in the metal to screen incoming fields. ω_p also indicates the bulk plasmon frequency of the metal. The bulk plasmon is a resonant charge density fluctuation occurring in the volume (or bulk) of the metal as result of the resonant interaction of the electrons with the incoming radiation (as
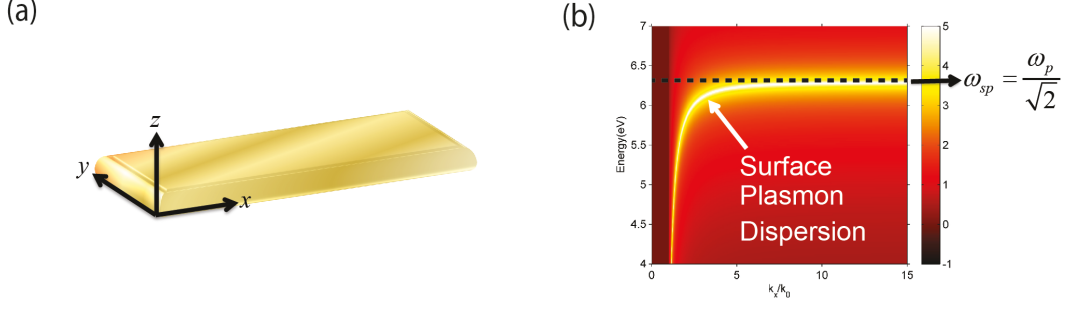
Figure C.1: (a) Simple drude metal displaying coordinate axis in relation to the metal interface. (b) Surface plasmon dispersion for an arbitrary local metal with 0 loss found from the poles of the reflection coefficient r_p. k_x/k_0 is the normalized in plane wavevector.

was probed by k-EELS in silicon in chapter 3).

Alongside bulk oscillations of the electron gas, one can also witness resonant electron oscillations that occur only at the surface of the metal which are the surface plasmon polaritons. Surface plasmons exist at the interface between a metal and a dielectric and are strongly confined to the surface of the metal and have characteristically large optical fields. The charge density fluctuations propagate along the metal-dielectric interface. Applying Maxwells Equations and the standard electromagnetic boundary conditions for a surface bound mode with fields decaying away from the interface, one can derive the analytic dispersion for a surface plasmon at an idealistic metal-vacuum halfspace:

$$k_x^{spp} = \frac{\omega}{c}\sqrt{\frac{\epsilon_{vac}\epsilon_{metal}}{\epsilon_{vac} + \epsilon_{metal}}} \qquad (C.3)$$

Here k_x^{spp} represents the in plane wavevector along the interface of the metal-vacuum halfspace for the surface plasmon. c is the speed of light and ϵ_{vac} and ϵ_{metal} are the permittivities in vacuum and the metal, respectively. The SPP resonant frequency (ω_{spp}) can be found from the pole of equation C.3 where $\epsilon_{vac} + \epsilon_{metal} = 0$ and as a result:

$$\omega_{spp} = \frac{\omega_p}{\sqrt{2}} \qquad (C.4)$$

In addition to the analytic expression above, one can map the SPP dispersion from the poles of the local p-polarized reflection coefficient (r_p) given by the Fresnel equations for a halfspace:

$$r_p = \frac{\epsilon_{metal}k_z^{vac} - \epsilon_{vac}k_z^{metal}}{\epsilon_{metal}k_z^{vac} + \epsilon_{vac}k_z^{metal}} \qquad (C.5)$$

Here, k_z is the wavevector defined perpendicular to the metallic interface. Using equation C.5 we can plot the reflection for an arbitrary metal with 0 loss as a function of the in plane wavevector, k_x, normalized by the free-space wavevector $k_0 = \omega/c$ (figure C.1). We see that the poles of the local reflection coefficient give us the dispersion of our surface plasmon at a metal halfspace.
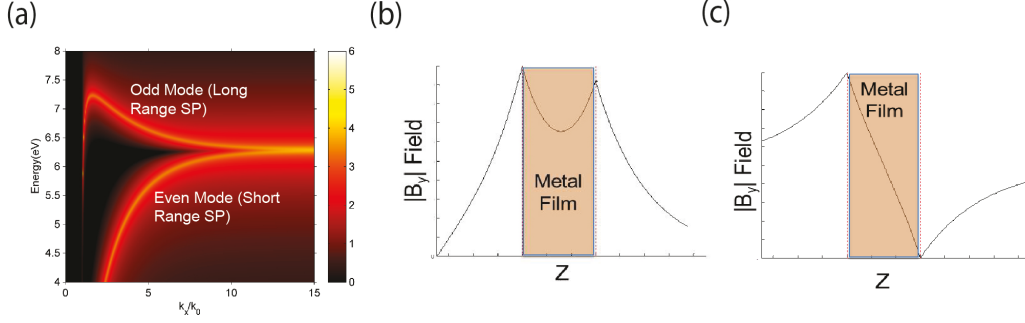
Figure C.2: (a) Reflection (log scale) from a 12 nm gold film. The gold is modeled with a simple Drude model with $\gamma = 1x10^{14}s^{-1}$ and $\omega_p = 8.9$ eV and we see a surface plasmon frequency at $\omega_{spp} = 6.3$. Near field coupling of the SPPs at each metal-vacuum interface results in an even and odd SPP mode. The magnetic field profile for such an even (b) and odd (c) mode is shown.

Now that we have a better understanding of the surface plasmon dispersion for an arbitrary metal halfspace, we can turn our attention to a more realistic thin film. Performing a similar electromagnetic boundary condition derivation, we can determine the reflection coefficient from a metallic thin film by considering that we now have an additional metal/dielectric interface in our problem.

$$r_p^{film} = \frac{r_{vac-metal} + r_{metal-vac}e^{2idk_z^{metal}}}{1 + r_{vac-metal}r_{metal-vac}e^{2idk_z^{metal}}} \tag{C.6}$$

Here $r_{vac-metal}$ and $r_{metal-vac}$ represent the reflections from the vacuum to the metal film at the first interface and the reflections from the metal film to the vacuum at the second interface, respectively. d is the thickness of the metal. Plotting our new reflection coefficient for a slab given by equation C.6 versus the normalized in plane wavevector k_x/k_0 we get the SPP dispersion seen in figure C.2 for an arbitrary Drude metal. One immediately notes that we now have two SPP modes present for this thin film. This is due to the fact that thin film can support two SPP modes, one at each of the metal-vacuum interfaces. If the metal film is thin enough, the two SP modes can hybridize as a result of near field coupling. As the fields across the metal do not completely decay away, the two SPPs can couple in two ways forming the even (figure C.2 (b)) and odd (figure C.2 (c)) modes.

Additionally, we note that as we increase the in-plane wavevector (or momentum) k_x, the two modes converge to the characteristic SPP energy given by equation C.4. Note that the SPP dispersions of Ag and silicon in chapters 2 and 3 , respectively do not show signatures of the odd SPP mode, even for the thinnest films. This is due to the fact that a series of interband transitions near the SPP energy severely damp the odd SPP mode.

75

Appendix D

Probing Quantum versus Nonlocal Effects in Nanophotonics with k-EELS

D.1 Introduction

The quantum nature of excitations in plasmonics and the control of non-classical light with metamaterials has opened the doors for new applications in nanophotonics [1, 2]. Recent experiments with electron energy loss spectroscopy on plasmonic nanoparticles have shown the effect of electron wavefunction quantization in disagreement with the characteristic predictions of plasmonic spectra using a local dielectric constant model [110, 55]. Effects such as electron tunneling between dimers also requires a quantum picture of plasmons [111, 112]. However, there also exists the question whether a non-local model for the dielectric constant can capture these effects without invoking electron quantization in nanoparticles, dimers and thin films [111, 112].

 Here, we show that along with the energy loss of electrons, the momentum transferred to the plasmons plays a key role in extracting the entire energy-momentum dispersion relation revealing deviations from a local dielectric response. We compare the local drude picture of an arbitrary metal (appendix C) with a nonlocal hydrodynamic model that captures the microscopic quantum effects with a macroscopic formalism. In the final section, we suggest that momentum-resolved electron energy loss spectroscopy (k-EELS) is an experimental technique that can map the non-local as well as quantum nature of collective electron-photon excitations in metallic nanostructures.

D.2 The Hydrodynamic Model for Nonlocal Reflection

In a majority of cases a good conductor, such as a metal, can be described very well by a completely local model as discussed in appendix C and as has been assumed throughout this thesis in chapters 2, 3, and 4. This is due to the fact that changes in the electron density in the bulk of a metal are essentially zero (i.e where ρ is the charge density), as any excess

charge transfers straight to the surface at extremely small timescales (≈ 50 ps). However, as the metal film becomes thinner, surface effects become comparable to those in the bulk and changes in the electron density become important when we start resolving the microscopic nature of the electrons at the surface of the metal.

Excess charge density results in a "smearing out" of charge on the scale of the Thomas-Fermi screening length at the surface of a metal due to a quantum pressure. This quantum pressure is a result of the Pauli Exclusion Principle creating a repulsive force between fermions spreading out the charge. As a result, along with the classic Coulomb force, the quantum repulsion manifests itself as a pressure in an electron gas that resists compression from an applied electric field.

One method that can provide a link between the intricate microscopic details of a quantum pressure and the macroscopic behaviour of a metal is to invoke material nonlocality, or spatial dispersion, into our material descriptions. Locality assumes that the permittivity response depends only on frequency ($\epsilon(\omega)$) such that, in real space, the permittivity at a location r does not depend on the permittivity at a location r'. With nonlocality, we bring in this spatial dependence by allowing our permittivity to not only depend on ω, but to also depend on the wavevector (k) such that $\epsilon(k,\omega)$. A macroscopic nonlocal description can describe the quantum "smearing of charge" as it takes into consideration the inhomogeneous distribution of electron density inside a metal.

The nonlocal hydrodynamic model describes the free electron motion inside a metal where the quantum pressure is modeled by a hydrodynamic flow from the kinetic theory of gasses. This results in a term described as the hydrodynamic polarization current added to the conventional equation of motion of an electron described by the local model (neglecting any nonlinear and magnetic contributions) [113]:

$$\frac{dv_d}{dt} + \gamma v_d = -\frac{eE}{m_e} - \frac{\beta^2}{n_e}\nabla n_e \tag{D.1}$$

v_d is the electron drift velocity, m_e is the effective mass of the electron, E is the applied electric field and n_e is the electron charge density. $\beta^2 = 3/5v_F^2$ is the phenomenological nonlocal constant dependent on the fermi velocity (v_F). The second term on the right-hand side of equation D.1 is the force from the quantum pressure modeled by the macroscopic hydrodynamic theory. Note that the force from the applied field (the first term on the right hand side) and the quantum pressure work in opposite directions (since $\rho = -e\nabla n_e$) which makes intuitive sense as the applied field will tend to "clump" the electrons together and the repulsive quantum pressure will work to spread the charges back in the opposite direction.

Expanding from equation D.1 we can express the current density for such a hydrodynamic equation of motion as follows where τ is the characteristic scattering time of the metal [113]:

$$J(r,\omega) = \sigma(\omega)E(r,\omega) - D(\omega)\nabla\rho(r,\omega)$$

$$\text{where} \quad \sigma(\omega) = \frac{e^2 n_e \tau}{m_e(1 - i\omega\tau)} \quad and \quad D(\omega) = \frac{\beta^2 \tau}{1 - i\omega\tau} \tag{D.2}$$

We note that the current density not only depends on the drift current (first term on RHS of equation D.2) proportional to the conductivity (σ) as seen in a local metal, but also to the diffusion current (second term on RHS of equation D.2) proportional to the diffusion constant ($D(\omega)$). Therefore, the hydrodynamic model incorporates the quantum pressure by an additional diffusive current proportional to the fermi velocity in the expression for the total current density of the metal.

Using continuity and expanding our fields we can also express the current density in terms of the total electric field where (I) is the identity dyadic:

$$J(r,\omega) = \sigma(\omega)\left[I - \frac{D(\omega)}{i\omega}\nabla\nabla\right]^{-1}\cdot E(r,\omega) \tag{D.3}$$

Equation D.3 allows us to make an important assessment regarding the longitudinal and transverse fields in our system. Recall that we can split our total E-field into transverse (E_T) and longitudinal (E_L) components. Transverse E-fields have wavevectors perpendicular to the direction of propagation and are divergence free, namely $\nabla \cdot E_T = 0$. This implies that the transverse fields are not affected by spatial dispersion (the second term on the right-hand side of equation D.3). The longitudinal fields however, are not divergence free ($\nabla \cdot E_L \neq 0$), and thus will be influenced by the $D(\omega)$ (the spatially dispersive) term in the above expression.

Due to the different behavior of transverse and longitudinal fields with spatially dispersive media, we can also define different permittivity responses for the respective fields. From our hydrodynamic model, we can derive the following longitudinal (ϵ_L) and transverse (ϵ_T) permittivities:

$$\epsilon_L = 1 - \frac{\omega_p^2}{\omega(\omega + i\gamma) - \beta^2 k^2} \tag{D.4}$$

$$\epsilon_T = 1 - \frac{\omega_p^2}{\omega(\omega + i\gamma)} \tag{D.5}$$

Additionally, we can derive the nonlocal reflection coefficient for a metal halfspace where $\Omega = \beta k_x^2$:

$$r_{nonlocal} = \frac{\epsilon_{metal}k_{z,vac} - \epsilon_{vac}k_{z,metal} - \Omega}{\epsilon_{metal}k_{z,vac} + \epsilon_{vac}k_{z,metal} + \Omega} \tag{D.6}$$

Equation D.4 and equation D.6 highlight the fact that nonlocal behavior results in a wavevector dependence in the material response. We note that if the nonlocal parameter $\beta \to 0$ we return to our local descriptions of the permittivity and reflection coefficient as seen in appendix C. We also note that at relatively low wavevector magnitudes (i.e small k) nonlocal effects can be neglected and the material can be described by a purely local response.

To analyze the effect of nonlocality on the plasmonic behavior of thin metal films we can plot the nonlocal reflection coefficient to map the SPP dispersion similar to the approach taken with the local reflection coefficient in appendix C. Figure D.1 shows the comparisons of the SPP dispersions for a local and nonlocal metal. One can clearly see deviations as the k_x dependence of the nonlocal model results in a non-plateauing SPP dispersion at the characteristic SPP energy. The deviations become prominent at high k_x as suggested by equation D.4 and equation D.6.

The nonlocal picture of metal thin film becomes extremely important to take into con-
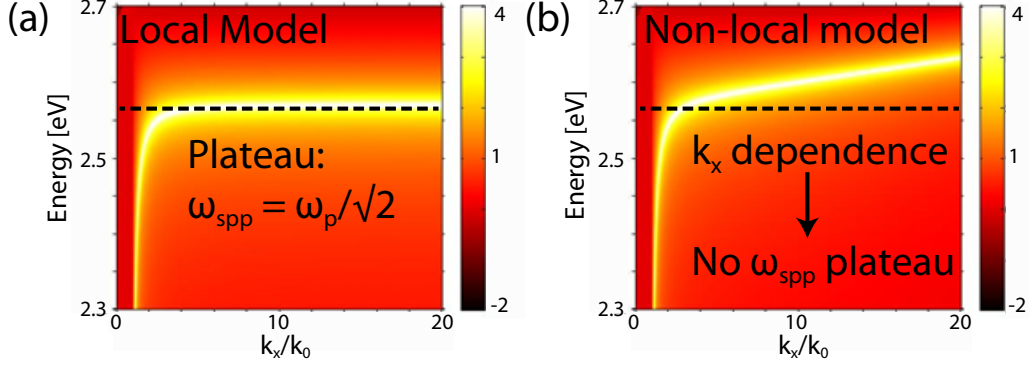
Figure D.1: (a) Local (a) and nonlocal reflection (b) for an ideal lossless metal in log scale. The bright band in each plot is the surface plasmon polariton dispersion of the metal that is manifest from the poles of the reflection coefficient. For the nonlocal description a fermi velocity of $v_F = 1.4m/s$ is assumed. At large magnitudes of the wavevector the nonlocal model begins to deviate from the local picture, and the traditional SPP resonant energy (or plataeu) no longer holds due ot the k_x dependence.

sideration when an electron spill out or an electron smearing effect at the surface of a metal introduce a charge density distribution in the metal which is not normally taken into consideration for bulk conductors. These effects are noticeable as the film approaches the 10 nm thickness range especially when probing high momentum states (i.e $k_x/k_0 > 10$). Accurately mapping the nonlocal plasmonic behaviour can be achieved with momentum resolved electron energy loss spectroscopy (k-EELS) as will be discussed in next section.

D.3 Mapping Nonlocal/Quantum Plasmonic Excitations with k-EELS

The k-EELS approach is a valuable technique to quantitatively compare non-local vs. quantum effects in plasmonics. As seen in figure D.1, high momentum states show the largest deviation in the SPP dispersion from the local model and thus are an important regime to potentially probe quantum and nonlocal behaviour. This is possible with k-EELS as a beam of electrons are able to induce excitations in material far past the light line (i.e $k_x/k_0 \gg 1$). In addition momentum-resolved EELS techniques are able to probe the non-local band structure (k_x dependence) alongside the energy (ω dispersion). Thirdly, optical techniques probe the transverse properties of a material, as incident optical radiation displaces electrons perpendicular to the direction of propagation. Electrons, however, probe the longitudinal response of a medium as they displace free electrons in the medium in the longitudinal direction and cause fluctuations in the local electron density [114]. Equation D.3 specifies that in order to probe the nonlocal behaviour of a material the longitudinal response must be investigated which is made possible with k-EELS techniques. As a result, k-EELS is the best experimental method to bridge the macroscopic non-local plasmonic

behaviour of a medium with its associated quantum effects to determine the excitation response.

Appendix E

Hyperbolic Metamaterials

E.1   Introduction and Background

Metamaterials research has captured the imagination of optical engineers and materials scientists because of their varied applications including imaging [115, 116, 2], cloaking [117, 118], sensing [119], waveguiding [120], and simulating space-time phenomena [121] (Figure 1). The field of metamaterials started with the search for negative dielectric permittivity and magnetic permeability however the range of electromagnetic responses achievable using nanostructured media far surpass the concept of negative index. The invisibility cloak is the best example where an inhomogeneous anisotropic electromagnetic response causes light to bend smoothly around an object rendering it invisible [122]. Another example is that of chiral metamaterials, where the response of a medium to polarized light can be enhanced by orders of magnitude through artificial structures [123, 124].

While all the above media have specific domains of application, hyperbolic metamaterials are a multi-functional platform to realize waveguiding, imaging, sensing, quantum and thermal engineering beyond conventional devices [125, 126, 127, 58, 100, 128]. This metamaterial uses the concept of engineering the basic dispersion relation of waves to provide unique electromagnetic modes that can have a broad range of applications [57, 129]. One can consider the hyperbolic metamaterial as a polaritonic crystal where the coupled states of light and matter give rise to a larger bulk density of electromagnetic states [130, 131]. Some of the applications of hyperbolic metamaterials include negative refraction [132, 78], sub-diffraction imaging [2, 3], sub-wavelength modes [120, 133] [26], and spontaneous [134, 135, 136, 137, 138] and thermal emission engineering [139, 140, 141].

The initial work in artificial structures with hyperbolic behavior started in the microwave regime (indefinite media) with phenomena such as resonance cones [128], negative refraction [142] and canalization of images [127]. In the optical domain, it was proposed that non-magnetic media can show hyperbolic behavior leading to negative index waveguides [126], sub-wavelength imaging [2] and sub-diffraction photonic funnels [120].

E.2 Hyperbolic Isofrequency Surfaces

Hyperbolic metamaterials (HMMs) derive their name from the topology of the isofrequency surface. In an isotropic medium, the linear dispersion and isotropic behavior of propagating waves implies a spherical isofrequency surface given by the equation $k_x^2 + k_y^2 + k_z^2 = \epsilon \omega^2 / c^2$ (in vacuum $\epsilon = 1$). The ability of such an isotropic medium and its ability to support photonics modes is discussed in detail in appendix B.1 and in figure B.1. However, if we were to now consider an extraordinary wave (TM polarized) in a uniaxial medium, this isofrequency relation changes to:

$$\frac{k_x^2 k_y^2}{\epsilon_z} + \frac{k_z^2}{\epsilon_x} = \frac{\omega^2}{c^2} \tag{E.1}$$
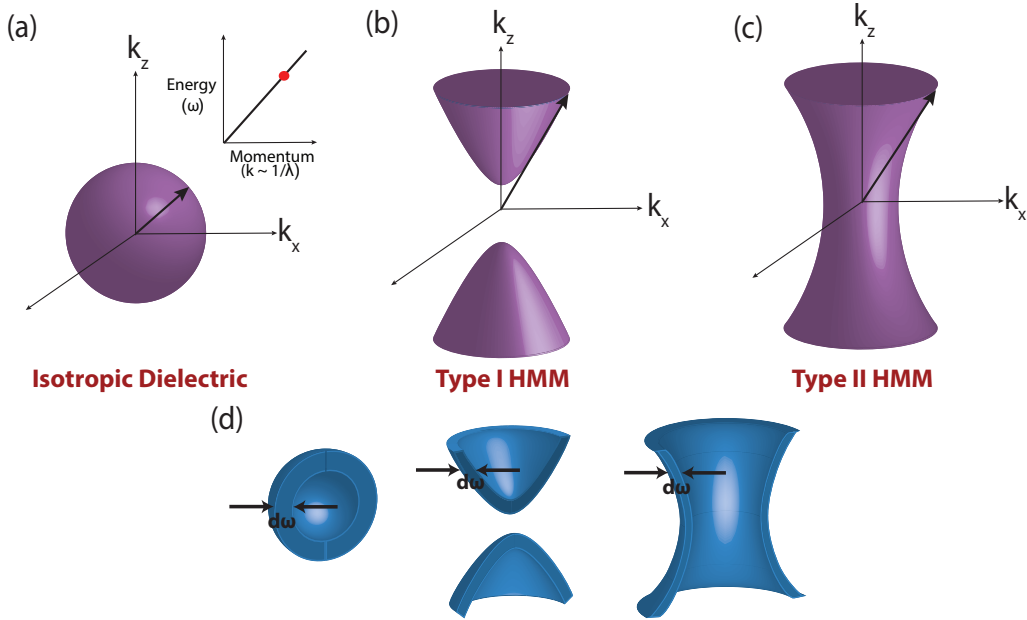
Figure E.1: (a) Spherical isofrequency surface for an isotropic dielectric. Inset shows an energy versus momentum relationship with the red dot indicating the operating frequency for the derived isofrequency surface. (b) Hyperboloid isofrequency surface for a uniaxial medium with an extremely anistropic dielectric response (Type I HMM: $\epsilon_z < 0; \epsilon_x; \epsilon_y > 0$) (c) Hyperboloid isofrequency surface for an extremely anistropic uniaxial medium with two negative components of the dielectric tensor (Type II HMM: $\epsilon_x; \epsilon_y < 0; \epsilon_z > 0$). The (b) Type I and (c) Type II hyperbolic metamaterials can support waves with infinitely large wavevectors in the effective medium limit. Such waves are evanescent and decay away exponentially in vacuum. (d) Isofrequency surfaces of an isotropic dielectric and the Type I and Type II HMMs at slightly different energies separated by $d\omega$. The enclosed volume between the two isofrequency surfaces is a measure of the photonic density of states of the system. It is clear that the hyperboloids have a diverging enclosed volume and thus, in the ideal limit, HMMs can support an infinite photonic density of states.

Note the uniaxial medium has an anisotropic dielectric response where the in-plane components are $\epsilon_x = \epsilon_y = \epsilon_\parallel$ and out of plane component is $\epsilon_z = \epsilon_\perp$. The spherical isofrequency surface of a purely isotropic material distorts to an ellipsoid for the anisotropic case when all components of $\bar{\epsilon}$ are greater than 0. However, when we have extreme anisotropy such that $\epsilon_\parallel \cdot \epsilon_\perp < 0$, the isofrequency surface opens into an open hyperboloid (figure E.1(b),(c)). Such a phenomenon requires the material to behave like a metal in one direction and a dielectric (insulator) in the other. This does not readily occur in nature at optical frequencies except for two known materials Bi_2Te_3 and Bi_2Se_3 as is discussed in chapter 4. Hyperbolic behaviour has been more readily achieved in the optical regime using artificial nanostructured electromagnetic media: metamaterials.

The most important property of such media is related to the behavior of waves with large magnitude wavevectors. In vacuum, such large wavevector waves are evanescent and decay exponentially. However, in hyperbolic media the open form of the isofrequency surface allows for propagating waves with infinitely large wavevectors in the idealistic limit [2, 134]. Thus there are no evanescent waves in such a medium. This unique property of propagating high-k waves gives rise to a multitude of device applications using hyperbolic media [57, 129].

It should be noted that there is a classification for hyperbolic media that helps to identify their properties. Type I HMMs have one component of the dielectric tensor negative ($\epsilon_z < 0; \epsilon_x; \epsilon_y > 0$) while Type II HMMs have two components negative ($\epsilon_x; \epsilon_y < 0; \epsilon_z > 0$) and are shown in figure E.1(b),(c), respectively. Note of course, that if all components are negative, we obtain a metal and if all components are positive we will have a dielectric medium. One striking difference between the Type I and Type II hyperbolic metamaterial is that the hyperboloidal surfaces are two sheeted and single sheeted respectively. The Type II metamaterial is highly reflective since it is more metallic than the Type I counterpart [143].

E.3 Design and Materials of HMM Structures

There are two practical approaches to achieve the hyperbolic dispersion which we discuss below. The fact that hyperbolicity requires metallic behavior in one direction and insulating behavior in the other leads to the requirement that both metals and dielectrics must be used as building blocks. Microscopically, the origin of the high-k propagating waves relies on a metallic building block to create the hyperbolic dispersion of the material. The polaritonic properties of the metallic building blocks allow for the necessary light-matter coupling to create the high-k waves. Specifically, it is necessary to have a phonon-polaritonic (optically active phonons) or plasmon-polaritonic (free electron) metal to construct hyperbolic meta-materials. The high-k modes are a result of the near-field coupling of the surface plasmon polaritons (SPPs) at each of the metal-dielectric interfaces in the structure. The high-k modes are the Bloch modes of the metal-dielectric superlattice.

E.3.1 1D HMMs

A thin film multilayer (super-lattice) consisting of alternating layers of metal and dielectric gives rise to the desired extreme anisotropy [144] (figure E.2 (b)). The layer thicknesses should be far below the size of the operating wavelength for the homogenization to be valid.
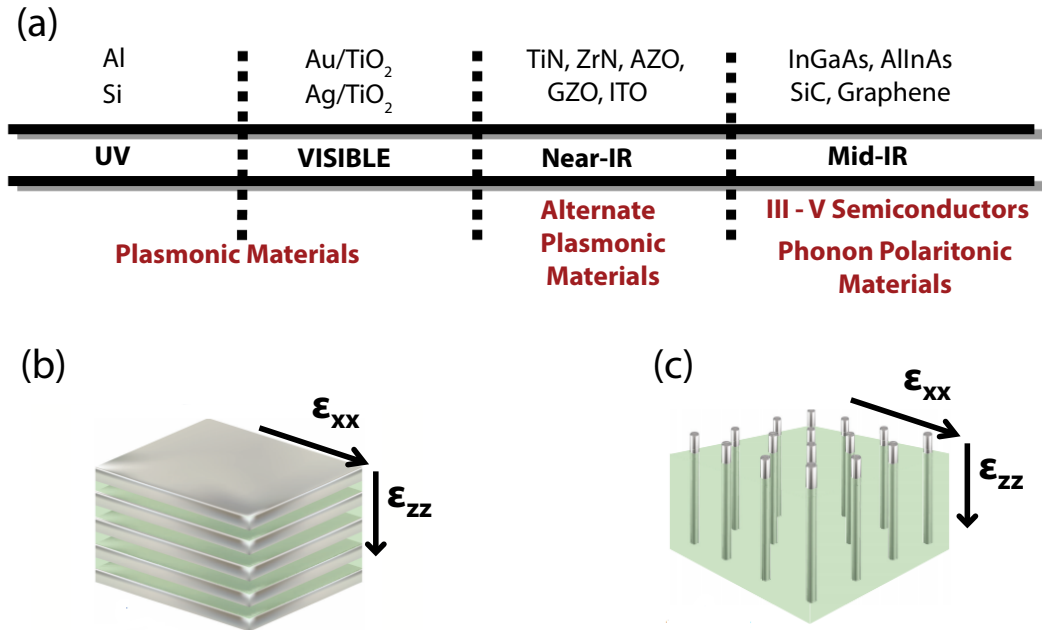
Figure E.2: (a) Materials used to create hyperbolic metamaterials depending on region of operation in the electromagnetic spectrum (UV to mid-IR and THZ frequencies) (b) Multilayer structure consisting of alternating metallic and dielectric layers forming a metal-dielectric superlattice. (c) Nanowire structure consisting of metallic nanorods embedded in a dielectric host. In both (b) and (c) the constituent components are subwavelength allowing characterization with effective medium theory.

A wide choice of plasmonic metals and high index dielectrics can give rise to hyperbolic behavior in different wavelength regimes (figure E.2 (a)). At ultraviolet (UV) frequencies, aluminum could be a suitable choice for the metallic component of the HMM, however, as seen in chapter 3 a Si/SiO_2 multilayer structure could push hyperbolic behaviour into the extreme UV. Au and Ag are by far the most popular materials for plasmonics in the visible due to their low loss and this holds true for HMMs as well. Certain designs that use gold a silver use high index dielectrics such as TiO_2 or SiN to push the HMM further into the visible regime [145] [40].

At near-infrared (IR) wavelengths, compensating for the reflective metallic behavior of naturally plasmonic metals like silver and gold is unfeasible and alternate plasmonic materials with tailored lower plasma frequencies are needed. These alternate plasmonic materials are based on transition metal nitrides or transparent conducting oxides and are ideally suited for hyperbolic media [146, 147]. Recently, their unique property of high melting point was also used to pave the way for high temperature thermal hyperbolic metamaterials [148, 139].

At mid-infrared wavelengths, one option for the metallic component in hyperbolic media consists of III-V degenerately doped semiconductors [78, 149]. The upper limit of doping concentration often limits their abilities to work as a metal at near-IR wavelengths, however

they are ideally suited to the mid-IR. Another option which is fundamentally different from above mentioned plasmonic metals is silicon carbide, a low loss phonon polaritonic metal [143, 150, 151]. SiC has a narrow reststrahlen band at mid-IR wavelengths which allows it to function as a metallic building block for hyperbolic media.

E.3.2   2d HMMs

Another approach to achieving hyperbolic behavior consists of metallic nanowires in a dielectric host [132, 152, 153, 154, 155](figure E.2 (c)). The choice of metals are usually silver and gold grown in a nanoporous alumina template. The major advantage of this design is the low losses, broad bandwidth and high transmission. Also, the problem of large reflectivity like the multilayer design does not exist and we can achieve Type I hyperbolic behavior. Note the fill fraction of metal needed in the 2D design to achieve Type I hyperbolic behavior is far below that in the multilayer design leading to a large figure of merit.

E.4   Density of States Engineering with HMMs

An orthogonal direction of application for hyperbolic media is in the area of engineering the photonic density of states (PDOS) [130, 131, 134, 156, 157]. A critical effect was unraveled with regards to the density of electromagnetic states inside hyperbolic media. As was outlined in detail in appendix B.1, the photonic density of states for a particular system can be calculated by determining the volume between two isofrequency surfaces of interest at ω_1 and ω_2. For a close isofrequency surface, such as a sphere or an ellipsoid in purely dielectric structures, this calculation leads to a finite value. In the case of the PDOS of the hyperbolic medium, it is clearly seen that this volume diverges leading to an infinite density of electromagnetic states within the medium (figure E.1 (d)).

Fermi's golden rule states that the spontaneous emission lifetime of emitters is strongly influenced by the density of available electromagnetic modes [158]. When fluorescent dye molecules or quantum dots are brought near the hyperbolic metamaterial the interaction is dominated by the modes with the highest density of states. As compared to the modes in vacuum, the hyperbolic high-k states dominate and the emitters preferentially couple to these modes [159]. This leads to a decrease in lifetime. Multiple experiments have explored this effect by studying dye molecules and quantum dots on top of the multilayer and nanowire hyperbolic metamaterial. Essentially, the large enhancement to the photonic density of states in hyperbolic media can directly lead to enhancements in absorption, photoluminescence, and radiative efficiency in photonic systems.

Appendix F

Threshold Reduction of Cherenkov Radiation in Hyperbolic Media and Trade-off with Loss

The foundation of the thresholdless Cherenkov radiation (TCR) phenomena is due to the unique hyperbolic topology of the HMM isofrequency surface that can support infinitely large wavevectors in the ideal limit. We can map the different values of the CR wavevector (k_c) on the hyperbolic surfaces for different velocities of the electron source (note: $tan(\theta_c) = k_x/k_z$). We see that in the limit that $v_z \to 0$ in equation 3.1 in chapter 3, θ_c (and thus k^c) approaches the asymptotes of the hyperbola for both the type I and type II case (figure F.1 (a)). In the ideal limit, infinitely large wavevectors can be supported at the asymptotes of the hyperbola and as such the phase velocity in the medium approaches 0 ($v_{phase} = \omega/k \to 0$). The minimum electron velocity where the CR condition is satisfied is at the point $v_z = v_{phase}$ and consequently the minimum CR velocity threshold is also $v_{th} \to 0$ in hyperbolic media.

One caveat to the unbounded velocity limit for CR in hyperbolic media is that we have an upper limit to the CR radiation condition in a type I HMM. This is due to the two sheeted nature of the type I hyperbola creating a bandgap in which photonic modes with wavevectors smaller than $k = k_0 * \sqrt{\epsilon_x}$ are not supported. As a result, any modes with $v_{phase} \geq c/\sqrt{\epsilon_x}$ cannot exist in type I HMMs leading to the upper CR cutoff in such structures. This upper TCR cutoff in type I HMMs ($v_z \leq c/\sqrt{\epsilon_x}$) is observed in figure 3.5 in chapter 3 where the TCR is suppressed at large v_z. Note that similar suppression does not occur in the type II region as it is truly thresholdless and no bandgap exists for the type II single-sheeted hyperboloidal isofrequency surface.

Figure F.1 (b) shows the full field simulations of TCR in the type I and type II regimes of the Si/SiO$_2$ effective medium described in figure 3.4 (a) in chapter 3 for electron velocities as low as $v_z = 0.001c$. In the ideal limit, the velocity has no lower limit, as indicated by figure F.1 (a). However, two key factors limit the threshold reduction of TCR in hyperbolic media: (1) the material loss and (2) the size of the unit cell of the multilayer structure.
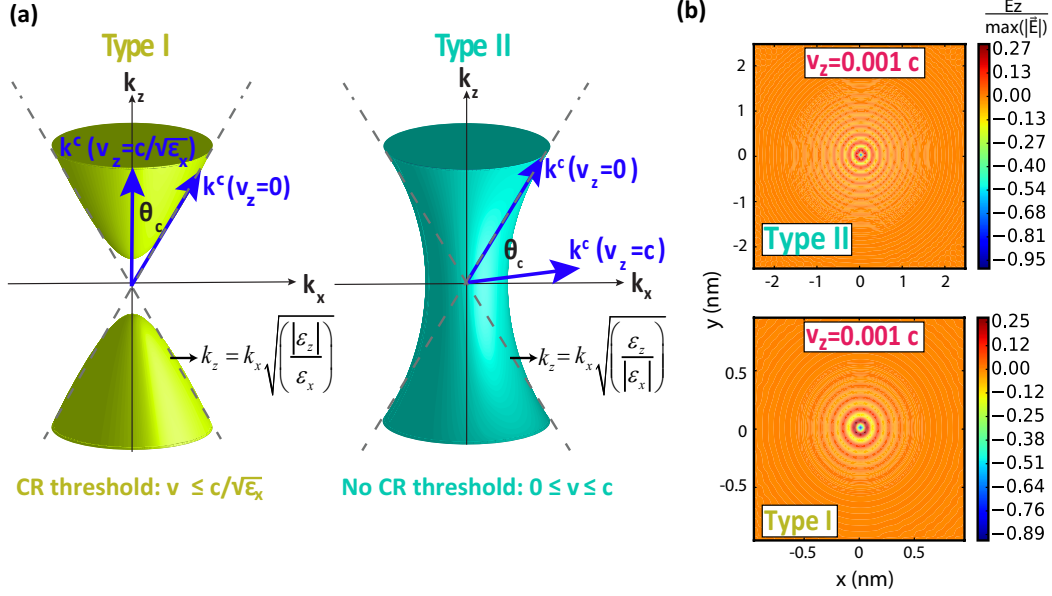
Figure F.1: (a) The type I ($\epsilon_x > 0$, $\epsilon_z < 0$) and type II ($\epsilon_x < 0$, $\epsilon_z > 0$) isofrequency surfaces for HMMs that can support thresholdless cherenkov radiation (TCR) with a wavevector k_c. The dashed lines show the asymptotes of the hyperbola and correspond to the k_c for which the Cherenkov velocity threshold is $v_z = 0$. This is where infinitely large wavevectors are supported in a hyperbolic medium and thus $v_{phase} = \omega/k \to 0$ and the Chernekov velocity threshold is eliminated. (b) Full field simulations of the type I and type II thresholdless Cherenkov radiation of the Si/SiO$_2$ effective medium described in figure 3.4 (a) in chapter 3 at velocities as low as $v_z = 0.001c$. In the ideal limit the TCR has no lower velocity threshold as seen in (a). However, material loss in the structure as well as the finite size of the unit cell of a real multilayer structure fundamentally limit the reduction of the phase velocity in the medium and thus limit the Cherenkov velocity threshold reduction.

The material loss and nonlocal effects greatly damp the high-k modes of hyperbolic media at large k and thus the phase velocity in the medium can never truly reach 0. As a result, we know that the threshold reduction is fundamentally limited by the ability to reduce the phase velocity, and the minimum threshold velocity is $v_{th} = v_{phase}$.

Additionally, the fundamental lower velocity limit will be governed by the wavelength limit at which the medium ceases to act as an effective medium. Figure F.1 (b) display the electric fields for a true effective medium and not a realistic multilayer structure which would have a finite unit cell size. The finite unit cell size limits the extent of the high-k modes supported by the structure to the edges of the brilliouin zone and as a result, limits the reduction of the phase velocity in the medium. For this reason, naturally occurring HMs, as described in chapter 4, may be more ideal candidates to observe TCR has they can be treated as a true effective hyperbolic medium.

87

Appendix G

The Transfer Matrix Method

G.1   Introduction

We begin by motivating that a simple way to produce a hyperbolic metamaterial involves creating a multilayer stack of alternating metal and dielectric layers. Zeroth order *Maxwell-Garnett* effective medium theory accurately predicts that if the layer thickness is subwavelength then the bulk response of the multilayer system may exhibit extreme anisotropy (i.e. metallic in one direction and dielectric in another direction) corresponding to a hyperbolic isofrequency curve. Furthermore, alternating layers of high-index / low-index dielectrics with layer thicknesses $\approx \lambda/4n$ can give rise to a one-dimensional photonic bandgap. Here n = refractive index of each layer.

In order to test this prediction, we can extend the ideas found from the Fresnel coefficients at a single interface to that of a multilayer system. Unfortunately, the conventional method for solving even simple case of a single layer requires the summation of an infinite amount reflections inside of the slab itself. This method is called Airy Summation. Therefore, one can imagine that extending this concept to a multilayer system would result in quite an arduous and cumbersome process that would be nearly impossible to solve using the Airy summation technique. Instead, we exploit the simple electromagnetic boundary conditions at each interface of the multilayer. Here we show that by exploiting the fact that the tangential components of the magnetic and electric field must be continuous across any planar boundary, we can relate the fields at any interface to any other interface contained in the multilayer. The operation is performed through a *transfer matrix* technique and it can be used to calculate the reflection and transmission of an arbitrarily complex multilayer system. The technique shown here is general enough to handle so called high-k evanescent waves so that this method can predict the location of dielectric waveguide modes and metallic plasmonic modes.

G.2   Transfer Matrix Formulation

From Figure 1, we may visualize the general multilayer system consisting of layers with dielectric constant ϵ_i and thickness d_i. It is assumed that the films have infinite extent in both the x- and y-directions.

The goal of the Transfer Matrix Method is to relate the the incident and reflected fields to the transmitted fields using a single *Transfer Matrix*. This Transfer Matrix will contain all the information contained within the constituent layers.

We will develop the formulation for p-polarized light, however, the result can be easily translated to the s-polarized case as well, which we will explicitly give at the end.

Due to the cylindrical symmetry, without a loss of generality we assume the wave has no transverse momentum in the y-direction. That is the propagation wavevector is $\boldsymbol{k} = k_x\hat{x} + k_z\hat{z}$ where k_x^i and k_z^i are the projections of the propagation wavevector along the x- and z-directions respectively. They are related using the iso-frequency relation

$$k_x^2 + k_z^2 = \epsilon(\omega/c)^2. \tag{G.1}$$

If $k_x^2 > \epsilon(\omega/c)^2$, we must ensure that the imaginary part of k_z is positive: $\text{Im}[k_z] > 0$ so that amplitudes of the electric and magnetic fields decay as they propagate.

P-polarized light only has a magnetic field in the y-direction such that in the ith layer the magnetic field can be written as $\boldsymbol{H^i} = H_y^i\hat{y}$ with

$$H_y^i = a_+^i e^{j(k_x^i x + k_z^i z)} + a_-^i e^{j(k_x^i x - k_z^i z)}. \tag{G.2}$$

That is, the ith layer supports both a forward and backward propagating wave. $a_\pm^i$ are the amplitudes of the forward and reverse propagating waves; note that these amplitudes are complex quantities.

Using Maxwell's equations we can relate the x-component of the electric field to the magnetic field as

$$E_x^i = \frac{k_z^i}{\epsilon_i k_o} a_+^i e^{j(k_x^i x + k_z^i z)} + \frac{-k_z^i}{\epsilon_i k_o} a_-^i e^{j(k_x^i x - k_z^i z)}, \tag{G.3}$$

where $k_o = \omega/c = 2\pi/\lambda$.

The electromagnetic boundary conditions at an interface require the components of the magnetic and electric field parallel to the interface, $\boldsymbol{H}_\parallel$ and $\boldsymbol{E}_\parallel$, be continuous across the boundary. For these conditions to be satisfied for all x, y we require that $k_x = k_x^i \ \forall i$. That is the transverse wavevector k_x is conserved for the whole system.

Therefore, for the ith interface $z = z_i$ and the boundary conditions require

$$E_x^i \big|_{z=z_i} = E_x^{i+1} \big|_{z=z_i} \tag{G.4}$$

$$H_y^i \big|_{z=z_i} = H_y^{i+1} \big|_{z=z_i}. \tag{G.5}$$

Cancelling out the common terms, the boundary conditions for the ith interface can be simplified to:

$$a_+^i e^{jk_z^i z_i} + a_-^i e^{-jk_z^i z_i} = a_+^{i+1} e^{jk_z^{i+1} z_i} + a_-^{i+1} e^{-jk_z^{i+1} z_i} \tag{G.6}$$

$$\frac{k_z^i}{\epsilon_i} a_+^i e^{jk_z^i z_i} - \frac{k_z^i}{\epsilon_i} a_-^i e^{-jk_z^i z_i} = \frac{k_z^{i+1}}{\epsilon_{i+1}} a_+^{i+1} e^{jk_z^{i+1} z_i} - \frac{k_z^{i+1}}{\epsilon_{i+1}} a_-^{i+1} e^{-jk_z^{i+1} z_i}. \tag{G.7}$$

It is convenient to rewrite this result above in simple matrix form.

$$\begin{pmatrix} 1 & 1 \\ \frac{k_z^i}{\epsilon_i} & -\frac{k_z^i}{\epsilon_i} \end{pmatrix} \begin{pmatrix} e^{jk_z^i z_i} & 0 \\ 0 & e^{-jk_z^i z_i} \end{pmatrix} \begin{pmatrix} a_+^i \\ a_-^i \end{pmatrix} = \begin{pmatrix} 1 & 1 \\ \frac{k_z^{i+1}}{\epsilon_{i+1}} & -\frac{k_z^{i+1}}{\epsilon_{i+1}} \end{pmatrix} \begin{pmatrix} e^{jk_z^{i+1} z_i} & 0 \\ 0 & e^{-jk_z^{i+1} z_i} \end{pmatrix} \begin{pmatrix} a_+^{i+1} \\ a_-^{i+1} \end{pmatrix}$$

(G.8)

Eqn. (3) can be rewritten in a more compact notation as

$$D_i p_i \begin{pmatrix} a_+^i \\ a_-^i \end{pmatrix} = D_{i+1} p_{i+1} \begin{pmatrix} a_+^{i+1} \\ a_-^{i+1} \end{pmatrix}$$

(G.9)

Additionally, this formulation can be extended to the $z = z_{i+1}$ interface such that

$$D_{i+1} p_{i+1} \begin{pmatrix} a_+^{i+1} \\ a_-^{i+1} \end{pmatrix} = D_{i+2} p_{i+2} \begin{pmatrix} a_+^{i+2} \\ a_-^{i+2} \end{pmatrix}.$$

(G.10)

Using the previous two equations we can relate the complex amplitudes of the ith layer to those of the $i + 2$th layer.

$$\begin{pmatrix} a_+^i \\ a_-^i \end{pmatrix} = \begin{pmatrix} e^{jk_z^i z_i} & 0 \\ 0 & e^{-jk_z^i z_i} \end{pmatrix}^{-1} \begin{pmatrix} 1 & 1 \\ \frac{k_z^i}{\epsilon_i} & -\frac{k_z^i}{\epsilon_i} \end{pmatrix}^{-1} \begin{pmatrix} 1 & 1 \\ \frac{k_z^{i+1}}{\epsilon_{i+1}} & -\frac{k_z^{i+1}}{\epsilon_{i+1}} \end{pmatrix} \begin{pmatrix} e^{jk_z^{i+1} z_i} & 0 \\ 0 & e^{-jk_z^{i+1} z_i} \end{pmatrix}$$

$$\begin{pmatrix} e^{jk_z^{i+1} z_{i+1}} & 0 \\ 0 & e^{-jk_z^{i+1} z_{i+1}} \end{pmatrix}^{-1} \begin{pmatrix} 1 & 1 \\ \frac{k_z^{i+1}}{\epsilon_{i+1}} & -\frac{k_z^{i+1}}{\epsilon_{i+1}} \end{pmatrix}^{-1} \begin{pmatrix} 1 & 1 \\ \frac{k_z^{i+2}}{\epsilon_{i+2}} & -\frac{k_z^{i+2}}{\epsilon_{i+2}} \end{pmatrix} \begin{pmatrix} a_+^{i+2} \\ a_-^{i+2} \end{pmatrix}$$

or equivalently,

$$\begin{pmatrix} a_+^i \\ a_-^i \end{pmatrix} = p_i^{-1} D_i^{-1} D_{i+1} P_{i+1} D_{i+1}^{-1} D_{i+2} p_{i+2} \begin{pmatrix} a_+^{i+2} \\ a_-^{i+2} \end{pmatrix}$$

(G.11)

Here, P_{i+1} is the combination of the fourth and fifth matrices on the right hand side of the equation – it will be written explicitly at the end of this section. Now, we may continue the same procedure as above by extending the formulation from the $i = 0$ layer all the way to the $i = N$ layer as in Figure 1. In this way we **transfer** the boundary conditions from the $i = 0$ to the $i = N$ interface.[1]

$$\begin{pmatrix} a_+^0 \\ a_-^0 \end{pmatrix} = p_0^{-1} D_0^{-1} \left(\prod_{i=1}^{N} D_i P_i D_i^{-1} \right) D_{N+1} p_{N+1} \begin{pmatrix} a_+^{N+1} \\ a_-^{N+1} \end{pmatrix}$$

(G.12)

Finally, if we define the first interface as the origin ($z_0 = 0$) and use the physical fields for the outer regions (incident and reflected wave for incident medium, and only a transmitted outgoing wave in the final medium) then the general result for p-polarized (and s-polarized) light is given by[2]

$$\boxed{\begin{pmatrix} 1 \\ r^{s,p} \end{pmatrix} = (D_0^{s,p})^{-1} T^{s,p} D_{N+1}^{s,p} \begin{pmatrix} t^{s,p} \\ 0 \end{pmatrix}}$$

(G.13)

---

[1] One may simply perform the substitutions $i \to 0, i + 1 \to i, i + 2 \to N + 1$ to obtain the result in Eqn. (8) as a shortcut.

[2] Eqn. (9) lacks the p_{N+1} term because it has been multiplied into the definition of $t^{s,p}$ as a simplification step.

where

$$T^{s,p} = \left(\prod_{i=1}^{N} D_i^{s,p} P_i (D_i^{s,p})^{-1} \right) \tag{G.14}$$

and

$$D_i^p = \begin{pmatrix} 1 & 1 \\ \frac{k_z^i}{\epsilon_i} & -\frac{k_z^i}{\epsilon_i} \end{pmatrix}, D_i^s = \begin{pmatrix} 1 & 1 \\ k_z^i & -k_z^i \end{pmatrix}, P_i = \begin{pmatrix} e^{-jk_z^i d_i} & 0 \\ 0 & e^{jk_z^i d_i} \end{pmatrix}. \tag{G.15}$$

The reflection and transmission coefficients are given by the following simple result:

$$r^{s,p} = \frac{M_{21}^{s,p}}{M_{11}^{s,p}} \tag{G.16}$$

$$t^{s,p} = \frac{1}{M_{11}^{s,p}} \tag{G.17}$$

where M is total transfer matrix equal to $(D_0^{s,p})^{-1} T^{s,p} D_{N+1}^{s,p}$.

Appendix H

The Electron Source and Energy Spectrometer in the TEM

In this appendix, we provide further details about the nature of the electron source used in the TEM experiments as well as details of the electron energy loss spectrometer.

H.1   The Electron Gun

In general, the source of electrons in a TEM is an electron gun that produces a beam of electrons with a high kinetic energy (with electron velocities at relativistic magnitudes). A negative potential acts as the electron source (or cathode) that is placed in an electron accelerating chamber. There are a few varieties of electron sources, we highlight the two major forms below:

- *Thermionic Emission*: A v-shaped wire, most commonly made of tungsten, is heated with a direct dc current to 2700 K, at which temperature electrons are emitted from the tip of the wire (as the thermal energy exceeds the work function of tungsten). Such sources, have a spread in the electron energy (Δ E) of approximately 1.5 eV and can be operated at chamber pressures as high as 10^{-2} Pa [160].

- *Field Emission*: A v-shaped tungsten tip is placed in an electrostatic field that reduces the width of the surface potential barrier for electrons at the fermi level. Once the width of the barrier is suitably reduced (the barrier width is comparable to the de Broglie wavelength), electrons can tunnel through the barrier and escape the tip. Field emission sources are much more stable, last for longer periods of time and can operate at much cooler temperatures (300 K) than thermionic sources. They have an average energy spread of approximately ΔE=0.3 eV, however chamber pressures can not be higher than 10^{-8} Pa [160].

Once electrons are emitted by either a thermionic or field emission processes, they are accelerated in the chamber via an applied electric field parallel to the optic axis by applying a potentail difference between an anode placed vertically below the electron source (the cathode).

The k-EELS experiments performed in chapters 2, 3, and 4 were conducted with a Hitachi HF-3300 TEM/STEM with a cold field emission (CFEG) gun source operated at a 300 keV accelerating potential, a temperature of 300 K, at a chamber pressure of approximately 10^{-8} Pa.

H.2 The Electron Energy Loss Spectrometer
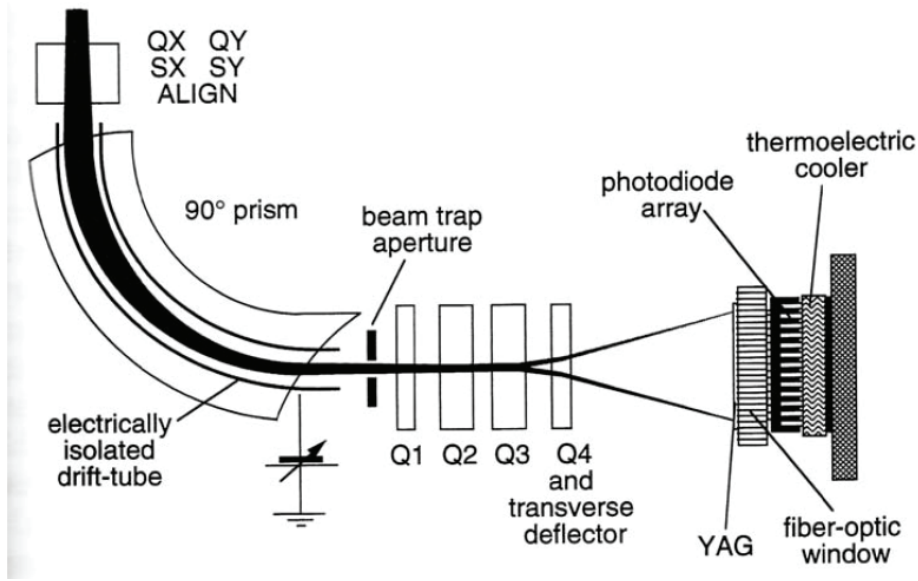
Figure H.1: A magnetic prism applies a force F perpendicular to the trajectory of the incoming electrons, bending through the prism at a radius R. Electrons with different degrees of energy loss will be bent at different bending radii, according to equation H.1. Electrons with the same energy loss are thus focused to the same location as they exit the spectrometer. The electron dispersion is then magnified by a series of quadrupole lenses. In order to record the dispersion and the intensity distribution of the electrons, they are projected onto a scintillator to produce a subsquent photo-intensity distribution that is imaged via a photodiode array or charge coupled device. *Image taken from Egerton [160]

The electron spectrometer detects small changes of the electron energy of the incident electrons on the order of single to 100s of electron volts. Note that the incident electrons have energies on the order of 100 keV, and as a result these truly minute changes can only be captured by what is known as a magnetic prism.

In a magnetic a prism, a highly uniform magnetic field ($B \approx 0.01$ Wb), generated via parallel plates of an electromagnetic, exerts a force $F = evB$ on each electron, where v is the velocity of the electron. This force acts perpendicular to the electron trajectory bending it through a radius R (figure H.1) such that:

$$R = mv/eB \qquad (H.1)$$

where m is the electron mass. As a result, electrons that lose energy (and subsequently have a smaller v), have a smaller bend radius R, and are bent through the magnetic prism at a larger angle than electrons that experienced no energy loss (elastically scattered electrons). As a result, electrons with the same energy (and thus energy loss), exit the spectrometer at the same location and a dispersive map of the energy loss of the electrons can be generated.

The actual dispersion of the electrons can be magnified by a series of quadrupole lenses after the electron exists the spectrometer. These quadrupoles (Q1, Q2, Q3, and Q4 in figure H.1) can be fine tuned to adjust the dispersive energy range of the electrons to be captured and recorded. The actual recording of the electrons is completed through a photo-intensity distribution obtained via a scintillator (generally YAG) coupled to a photodiode array or charge coupled device (CCD) (figure H.1).

The k-EELS experiments performed in chapters 2, 3, and 4 were conducted with a Gatan Image Filter (GIF) Tridiem^{TM} and the MAESTRO central computer control system [65].

Appendix I

Focused Ion Beam Milling Methodology for k-EELS Sample Preparation

In this appendix we detail the process of preparing free-standing structures for TEM analysis via focused ion beam milling (FIB). Here we specifically look at the preparation for the silicon samples used in 3. Aside from a few minor adjustments, this methodology also holds for sample preparation of the Bi_2Te_3 sample in chapter 4. The FIB sample preparation was performed with the aid of Douglas Vick of NRC-NANO. The sample was prepared using a Hitachi Nanoduet NB5000 Dual Beam FIB/SEM. The following steps outline the sample preparation process:

1. A protection layer of W was deposited using the Gas Injection System (GIS) and a 40-1-80 probe[1]. The dimension of the deposition area was 15 μm x 6 μm. Note: this protection layer did not need to be too thick its purpose was to protect the Si surface from ion damage during subsequent imaging/trenching.

2. 8-step staircase recipes were used to trench around the volume of interest. A large current probe (40-1-300, current 12.1 nA) was used for this step.

---
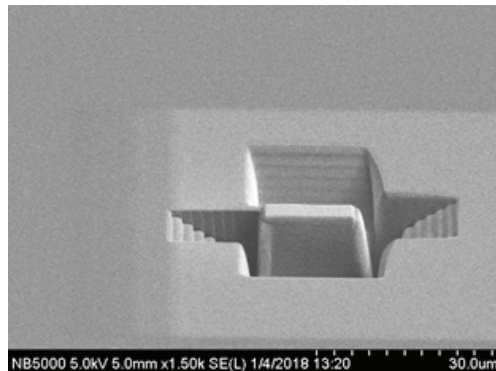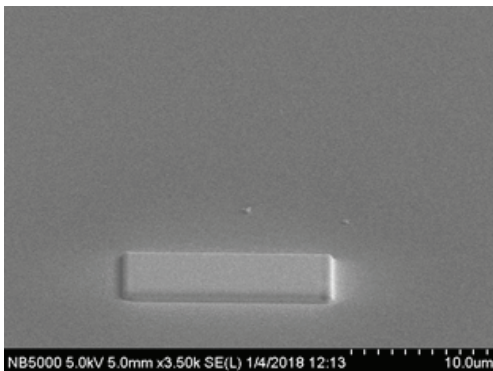
[1]Hitachi notation: 40-1-80 == 40 kV Ga ions, condenser lens on, 80 μm diameter aperture

3. The eucentric stage was tilted to 45° and a medium current probe (40-1-150, 2.5 nA) was used to free the bottom and sides of the lamella, leaving only a thin bridge connecting the sample to the bulk.

4. The microsampler (MS) probe was brought in, lowered to the sample, and affixed with W using the GIS. The bridge was than cut and the lamella plucked.
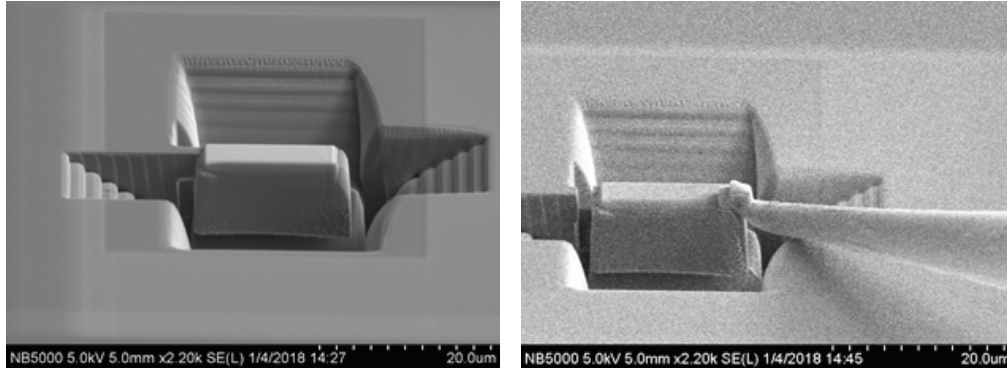
5. The work site was now switched from eucentric stage (holding the bulk Si chip), to the side entry revolver mesh holder, into which a TEM grid was mounted. The MS probe was brought over to the grid and the sample affixed with the GIS system to one finger of the grid.
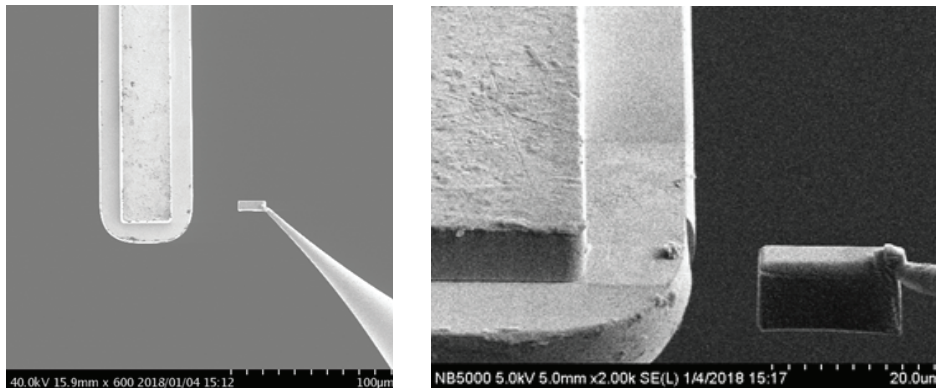
6. The MS probe was cut from the sample and retracted.

7. The revolver holder was rotated 90° so that the FIB beam was oriented parallel to the finger of the grid. Another protection layer of W was added prior to the thinning steps.
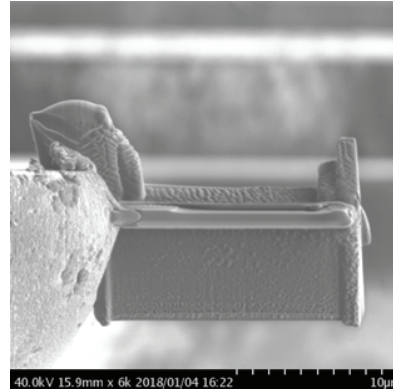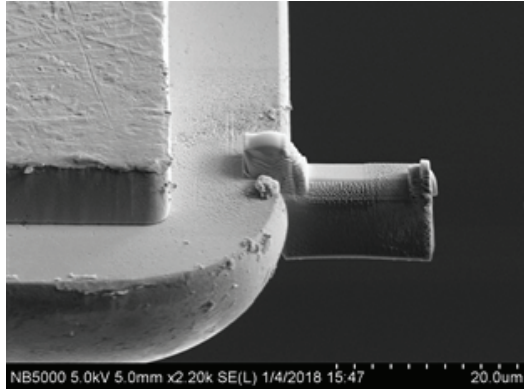
8. The sample was thinned to about 1 μm thickness using the 40-1-150 probe (2.5 nA). In order to compensate for the radial profile of the ion beam and create a lamella with parallel faces, the stage tilt was adjusted $\pm0.8°$ during front/rear side milling.

9. Probes of progressively smaller current (800 pA, 80 pA) were used to thin the lamella further down to electron transparency conditions for the TEM.

10. Reduction of amorphous damage layers were performed in 2 steps:

   - Rastering with a 5 kV probe (5-1-150, 120 pA) for 30 seconds each side, tilt adjustment $\pm3°$
   - Rastering with a 2 kV probe (2-1-150, 170 pA) for 30 seconds each side, tilt adjustment $\pm5°$